DISSERTATION

Phenomenological Modeling of Reactive Single-Particle Transport in Semiconductor Processing

ausgeführt zum Zwecke der Erlangung des akademischen Grades
eines Doktors der technischen Wissenschaften

unter der Betreuung von

Associate Prof. Dipl.-Ing. Dr.techn. Josef Weinbub
O.Univ.Prof. Dipl.-Ing. Dr.techn. Dr.h.c. Siegfried Selberherr

eingereicht an der Technischen Universität Wien
Fakultät für Elektrotechnik und Informationstechnik
von

Luiz Felipe Aguinsky, MSc.
Matrikelnummer: 11834250

Wien, im November 2022

Abstract

The continuing evolution of micro- and nanotechnology puts ever-increasing pressure on the involved manufacturing processes. In the context of this expanding complexity, the experimental and empirical knowledge of process developers must be complemented with physically-sound modeling and simulation. Historically, the focus of simulations of fabrication processes has been on manufacturing steps which directly impact the electrical characteristics of the final devices. In more recent decades, however, increased attention has been placed on directly investigating the manufactured device structure. The computational modeling of evolving surfaces during their fabrication processes is the purview of topography simulation.

Topography simulation is composed of two main elements: A method for describing the advecting surfaces, and reactive transport models which determine the surface advection velocity fields. The focus of this thesis is on the latter, building upon previous work which has already established the level-set (LS) method to treat the former. Reactive transport can be directly modeled through a combination of reactor-scale simulations, which determine the physical and chemical properties of the reactant species, and first-principle simulations describing the interaction of such species with the surface. However, these simulations are computationally very costly and complex. Also, there is still substantial debate about the intricacies of the chemical phenomena in many manufacturing processes, thus, this type of modeling might not be possible.

Instead, this thesis presents phenomenological models for reactive transport based on first-order reversible Langmuir kinetics using a single effective particle. A particle can either represent a specific chemical species or it can be an aggregate proxy of multiple and often unknown reactants. Although several processes require the consideration of multiple particles, the spirit of parsimony required for phenomenological modeling motivates this thesis to explore the profound complexity already present in reactive single-particle transport.

By reducing the physical and chemical complexity to a restricted number of parameters, not only can experimental surfaces be reproduced, but also insights into the surface chemistry can be gained. To achieve this, this thesis presents an overview of the existing approaches for reactant flux distribution calculations. A particular focus is given on viewing the venerable but often misunderstood Knudsen diffusive transport through a novel lens, which is the major methodological contribution of this work. Then, these reactive transport models are applied to specific problems.

The first novel contribution of this thesis with respect to applications is the novel integration of a Knudsen diffusion-based model with the LS method for thermal atomic layer processing (ALP) in high aspect ratio (AR) structures. This integration permits a thorough analysis of the model parameters and the qualitative investigation of a platform for three-dimensional (3D) integration of novel memories. In another contribution, existing flux calculation approaches are evaluated for the process of low-bias sulfur hexafluoride (SF_6) plasma etching of silicon (Si). This enables new interpretations and analyses, most notably the extraction of an empirical relationship between experimentally-accessible measurements and surface-chemical properties. In a final novel application, the capabilities of topography simulation are showcased in the optimization of Si microcavity resonators through a custom robust automatic calibration procedure.

In conclusion, it is shown that the final topography of a processed device carries the fingerprint of the surface chemistry occurring during the manufacturing process. This fundamental result is the enabler of direct modeling of experimentally processed surfaces as well as inverse modeling: The extraction of chemical information from experimental surfaces. In summary, topography simulation using phenomenological single-particle reactive transport modeling is a powerful tool which is able to complement reactor-scale and first-principle calculations.

Kurzfassung

Die fortschreitende Entwicklung der Mikro- und Nanotechnologie erfordert einen immer höheren Druck auf die betroffenen Herstellungsprozesse. Im Kontext dieser wachsenden Komplexität muss das experimentelle und empirische Wissen der Prozessentwickler_innen durch physikalisch fundierte Modellierung und Simulation ergänzt werden. Historisch lag der Fokus der Simulationen von Herstellungsprozessen auf jenen Schritten, die sich direkt auf die elektrischen Eigenschaften der Halbleiter-Bauelemente auswirken. In den letzten Jahrzehnten wurde jedoch verstärktes Interesse auf die direkte Untersuchung der Struktur der hergestellten Bauelemente gelegt. Die computergestützte Modellierung der sich verändernden Oberflächen während des Herstellungsprozesses ist der Aufgabenbereich der Topographiesimulation.

Die Topographiesimulation besteht aus zwei Hauptelementen: Eine Methode zur Beschreibung der sich bewegenden Oberflächen und reaktive Transportmodelle, welche die Geschwindigkeitsfelder der Oberflächenadvektion bestimmen. Der Schwerpunkt dieser Arbeit liegt auf letzterem, aufbauend auf früheren Arbeiten, die bereits die "Level-Set"-Methode zur Behandlung des ersteren etabliert haben. Der reaktive Transport kann durch eine Kombination aus Simulationen im Reaktormaßstab, welche die physikalischen und chemischen Eigenschaften der reaktiven Spezies bestimmen, und "First-Principles"-Simulationen, welche die Interaktion dieser Spezies mit der Oberfläche beschreiben, direkt modelliert werden. Allerdings sind diese Simulationen sehr rechenintensiv und komplex. Außerdem gibt es immer noch umfangreiche Diskussionen über die Besonderheiten der chemischen Phänomene in vielen Herstellungsprozessen, sodass diese Art der Modellierung unter Umständen nicht möglich ist.

Stattdessen werden in dieser Dissertation phänomenologische Modelle für den reaktiven Transport auf Basis der reversiblen Langmuir-Kinetik erster Ordnung unter Verwendung eines einzigen effektiven Partikels vorgestellt. Ein Partikel kann entweder eine spezifische, chemische Spezies repräsentieren oder es kann ein aggregierter Ersatz für mehrere und oft unbekannte Reaktanten sein. Obwohl mehrere Prozesse die Berücksichtigung mehrerer Partikel erfordern, motiviert der für die phänomenologische Modellierung erforderliche Sinn für Parsimonie diese Dissertation dazu, die tiefe Komplexität zu erforschen, die bereits im reaktiven Einzelpartikeltransport vorhanden ist.

Indem die physikalische und chemische Komplexität auf eine begrenzte Anzahl von Parametern reduziert wird, können nicht nur experimentelle Oberflächen reproduziert werden, sondern auch Einblicke in die Oberflächenchemie gewährt werden.

Um dies zu erreichen, wird in dieser Dissertation ein Überblick über die bestehenden Methoden zur Berechnung der Verteilung von Reaktantenflüssen gegeben. Ein besonderer Schwerpunkt liegt auf der Betrachtung des altbekannten, aber oft missverstandenen Knudsen-Diffusionstransports durch eine neue Linse, was der wichtigste methodische Beitrag dieser Arbeit ist. Dann werden diese reaktiven Transportmodelle auf spezifische Probleme angewandt.

Der erste neuartige Beitrag dieser Dissertation in Bezug auf Anwendungen ist die neuartige Integration eines auf Knudsen-Diffusion basierenden Modells mit der "Level-Set"-Methode für die thermische Atomlagenbearbeitung in Strukturen mit hohem Aspektverhältnis. Diese Integration erlaubt eine gründliche Analyse der Modellparameter und die qualitative Untersuchung einer Plattform für die dreidimensionale Integration von neuartigen Speichern. In einem weiteren Beitrag werden bestehende Methoden zur Flusskalkulation für den Prozess des Schwefelhexafluorid-Plasmaätzens von Silizium mit geringer Bias bewertet. Dies ermöglicht neue Interpretationen und Analysen, insbesondere die Extraktion einer empirischen Beziehung zwischen experimentell zugänglichen Messungen und oberflächenchemischen Eigenschaften. In einer finalen, neuartigen Anwendung werden die Möglichkeiten der Topographiesimulation bei der Optimierung von Si-Mikrokavitätenresonatoren durch ein eigenes robustes automatisches Kalibrierungsverfahren demonstriert.

Abschließend wird gezeigt, dass die Endtopographie eines gefertigten Bauelements den Fingerabdruck der Oberflächenchemie trägt, die während des Herstellungsprozesses auftritt. Dieses fundamentale Ergebnis ermöglicht die direkte Modellierung von experimentell prozessierten Oberflächen ebenso wie die inverse Modellierung: die Extraktion von chemischen Informationen aus experimentellen Oberflächen. Zusammenfassend lässt sich sagen, dass die Topographiesimulation mit Hilfe der phänomenologischen Modellierung des reaktiven Einzelteilchentransports ein leistungsstarkes Instrument ist, das die Berechnungen im Reaktormaßstab und die "First-Principles"-Berechnungen ergänzen.

Resumo

A evolução contínua da micro e nanotecnologia coloca uma pressão cada vez maior sobre os processos de fabricação envolvidos. No contexto dessa complexidade em expansão, o conhecimento experimental e empírico dos desenvolvedores de processos deve ser complementado com modelagem e simulação fisicamente fundamentada. Historicamente, o foco das simulações de processos de fabricação incidiu sobre as etapas de fabricação que impactam diretamente nas características elétricas dos dispositivos finais. Em décadas mais recentes, no entanto, a maior atenção tem sido dada à investigação direta da estrutura dos dispositivos fabricados. A modelagem computacional de superfícies em evolução durante os processos de fabricação é o âmbito da simulação de topografia.

A simulação de topografia é composta de dois elementos principais: um método para descrever as superfícies advectantes e modelos de transporte reativos que determinam os campos de velocidade de advecção da superfície. O foco dessa tese é no último, baseado em trabalhos anteriores que já estabeleceram o método de conjunto de nível para tratar o primeiro. O transporte reativo pode ser modelado diretamente através de uma combinação de simulações em escala de reator, que determinam as propriedades físicas e químicas das espécies químicas reativas, e simulações de primeiros princípios descrevendo a interação de tais espécies com a superfície. No entanto, essas simulações são muito caras e complexas computacionalmente. Além disso, ainda há um debate considerável sobre os meandros dos fenômenos químicos envolvidos em muitos processos de fabricação, portanto, esse tipo de modelagem nem sempre é possível.

Ao invés disso, essa tese apresenta modelos fenomenológicos para o transporte reativo baseados em cinética de Langmuir reversível de primeira ordem, usando uma única partícula efetiva. Uma partícula pode representar uma espécie química particular ou pode ser um substituto agregado de múltiplos reagentes, os quais por vezes são desconhecidos. Embora diversos processos exijam a consideração de múltiplas partículas, o espírito de parcimônia necessário para a modelagem fenomenológica leva essa tese a explorar a profunda complexidade já presente no transporte reativo de uma única partícula.

Reduzindo a complexidade física e química a um número restrito de parâmetros, não apenas as superfícies experimentais podem ser reproduzidas, mas também é possível obter uma compreensão maior da química de superfície. Para conseguir isso, esta tese apresenta uma visão geral das abordagens já existentes para cálculos de distribuição de fluxo de reagentes. Um enfoque particular é dado na análise do venerável, mas freqüentemente incompreendido, transporte difusivo de Knudsen através de uma nova perspectiva, o que constitui a principal contribuição metodológica deste trabalho. Em seguida, esses modelos de transporte reativos são aplicados a problemas específicos.

A primeira contribuição original dessa tese com relação a aplicações é a integração inovadora de um modelo de difusão de Knudsen com o método de conjunto de nível para processamento térmico de camadas atômicas em estruturas de alta relação de aspecto. Essa integração permite uma análise completa dos parâmetros do modelo e a investigação qualitativa de uma plataforma de integração tridimensional de novas memórias. Em outra contribuição, as abordagens existentes para o cálculo do fluxo são avaliadas para o processo de corrosão de silício com hexafluoreto de enxofre em baixo viés de voltagem. Isso permite interpretações e análises originais, mais notavelmente a extração de uma relação empírica entre as medidas experimentalmente acessíveis e propriedades químicas de superfície. Em uma última contribuição original, as capacidades de simulação topográfica são demonstradas na otimização de microcavidades ressonadoras de silício através de um procedimento de calibração automática robusto e individualizado.

Em conclusão, mostra-se que a topografia final de um dispositivo processado carrega a impressão digital da química de superfície que ocorre durante o processo de fabricação. Esse resultado fundamental é o que permite a modelagem direta de superfícies processadas experimentalmente, bem como a modelagem inversa: a extração de informações químicas de superfícies experimentais. Em resumo, a simulação topográfica usando a modelagem fenomenológica de transporte reativo por uma única partícula é uma ferramenta poderosa que é capaz de complementar os cálculos em escala de reator e de primeiros princípios.

Acknowledgement

The intense journey that is the pursuit of a doctoral degree is, ultimately, a product of the collaboration between the student and the supervisors. I would like to firstly thank my primary supervisor, Prof. Josef Weinbub, for his outstanding level of support for all of my ideas, plans, and ambitions. I always knew that I could count on him to provide sharp, precise, and timely feedback which in turn has enormously expanded my own scientific skills.

Jointly, I owe a debt of gratitude to my secondary supervisor, Prof. Siegfried Selberherr. I greatly admire and appreciate his immense legacy in establishing the Institute for Microelectronics as a leading center for globally-recognized research. The Institute was an excellent place of work, where I could follow my own ideas while still relying on the incredible expertise of the local researchers. The lively discussions fostered by Prof. Selberherr have made me a more well-rounded scientist, his feedback has ingrained in me the necessity of a sharp eye for detail, and his extensive knowledge has guided me from my beginnings as a complete novice in the field of TCAD.

Additional thanks go to Dr. Andreas Hössinger from the industrial partner Silvaco Europe Ltd., who has worked intensely in conjunction with Prof. Weinbub to create and maintain the Christian Doppler Laboratory for High Performance Technology Computer-Aided Design (HPTCAD). His input has prompted research questions which are simultaneously scientifically engaging as well as industrially relevant. I am grateful for the interesting discussions we had in our regular meetings and for his valuable and efficient feedback.

This thesis would not have been possible without the help of my colleagues and friends from the Christian Doppler Laboratory for HPTCAD and also from the Institute for Microelectronics in general. Special thanks go to Frâncio Rodrigues, co-founder of the Brazilian specialty coffee corner, who has been my editor and proof-reader of first resort, and who has indulged with me in lengthy musings about the past, present, and future of the global semiconductor industry. Additional thanks go to Christoph Lenz, Paul Manstetten, Xaver Klemenschits, Roberto Orio, Felipe Ribeiro, Alex Toifl, Michael Quell, Tobias Reiter, and Alex Scharinger for the scientific and also not-so-scientific lunch discussions. This work would also not have happened without the practical help from the entire staff of the Institute, and to that I thank Diana Pop and Petra Kampter-Jonas, who help hold everything together, and Prof. Tibor Grasser for his stewardship.

My support network originally started in that far away land of Porto Alegre, Brazil, but over the years it now extends globally. My everlasting thanks for the friendship and support from my fellow expatriates, exiles, and outcasts: Pedro Perfeito, Arthur Loureiro, Augusto Medeiros, Rodrigo Sieben, Natália Amaral-Skreinig, Gustavo Amaral-Skreinig, Genário Oliveira, Matheus Pinheiro, and Wilton Loch. Your support, companionship, and role-playing game sessions were absolutely necessary for surviving these trying times. My friends from other parts of the planet are also always present at heart and are dearly thanked. Alex Zimmermann, Ahish Vishwanatha, and Bill Heymann have all been fundamental for me to overcome so many difficulties, and I treasure your camaraderie.

Last but absolutely not least I give my heartfelt thanks to my amazing family. To my beloved wife Aline, the best part of my life, I am so grateful for you being my partner, supporter, and number one fan in this amazing journey through this narrow bridge that is life. I also thank my brother João Pedro, who has always strived to be with me everywhere I am, even when geographically impossible, to always give me the best advice. My aunt Susana, who always takes the time to check in on me, is deeply thanked. My incredible parents have supported me throughout my life, and I am so grateful for everything they have done through the years. I thank my father Sergio for the love, support, and encouragement for me to always follow my dreams and passions. Finally, my mother Beatriz has always been my great inspiration for all academic pursuits, showing me that the world can be understood and repaired through both science and loving kindness. My love and thanks to you.

Contents

List of Figures

List of Tables

List of Abbreviations

ROC	radius of curvature
1D	one-dimensional
2D	two-dimensional
3C-SiC	cubic silicon carbide
3D	three-dimensional
$\mathbf{Al_2O_3}$	aluminum oxide
ALD	atomic layer deposition
ALE	atomic layer etching
$\mathbf{AlF_3}$	aluminum fluoride
ALP	atomic layer processing
AR	aspect ratio
$\mathbf{Ar^+}$	argon
ARDE	aspect ratio dependent etching
ASD	area-selective deposition
BC	boundary condition
BEOL	back end of line
$\mathbf{C_2H_4}$	ethylene
CC	concave-concave
CD	critical dimension
CFL	Courant-Friedrichs-Lewy
$\mathbf{Cl_2}$	chlorine gas
CMOS	complementary metal-oxide-semiconductor
CMP	chemical-mechanical planarization
CVD	chemical vapor deposition
DMAC	dimethylaluminum chloride
DRAM	dynamic random-access memory
DRIE	deep reactive ion etching
EAR	equivalent aspect ratio
EDA	electronic design automation
EPC	etch per cycle
$\mathbf{F_2}$	fluorine gas
FinFET	fin field-effect transistor

FLOOXS	Florida object-oriented multipurpose simulator
GAA	gate-all-around
GPC	growth per cycle
GSA	generalized simulated annealing
H_2O	water
HF	hydrogen fluoride
HfO_2	hafnium oxide
HPTCAD	High Performance Technology Computer-Aided Design
ICP	inductively couple plasma
LS	level-set
MEMS	microelectromechanical systems
N_2	nitrogen gas
NEMS	nanoelectromechanical systems
ODE	ordinary differential equation
ON	oxide-nitride
PC	plano-concave
PVD	physical vapor deposition
ReRAM	resistive random-access memory
RIE	reactive ion etching
SDF	signed-distance function
SEM	scanning electron micrography
SF_6	sulfur hexafluoride
Si	silicon
SiO_2	silica
$Sn(acac)_2$	tin(ii) acetylacetonate
SPER	solid phase epitaxial regrowth
TCAD	technology computer-aided design
TCS	trichlorosilane
TEM	transmission electron micrography
TEMAH	tetrakis(ethylmethylamino)hafnium
TMA	trimethylaluminum
VCQ	Vienna Center for Quantum Science and Technology
VSC	Vienna Scientific Cluster
XeF_2	xenon difluoride

Chapter 1

Introduction

The modern world is brimming with micro- and nanoscale devices. Whether semiconducting logic [1] or memory devices [2] at the core of modern computing systems, optical or optoelectronic devices in communications [3] and quantum science [4], or microelectromechanical systems (MEMS) sensors in aviation [5], there is no facet of society which has not been transformed by these advanced technologies. However, the continuing advancement of micro- and nanotechnology requires ever more complex manufacturing, with modern semiconductor fabrication facilities nowadays sometimes requiring investments in the order of tens of billions of dollars [6].

With such enormous resources involved, the development of new technologies cannot depend only on experimental pathfinding, since the experiments can be very complex and costly, and the design space is too vast [7]. Therefore, simulation tools are fundamental as a cost-saving and insight-producing measure. Over the decades, the field of technology computer-aided design (TCAD) has emerged to address the issue of development and application of computational models to simulate the fabrication and operation of semiconductor devices and circuits [8].

TCAD contains several sub-fields which can be broadly gathered into three distinct categories, as illustrated in Fig. 1.1. At the center is *device TCAD* which concerns itself with simulating device operation [9]. Device TCAD concerns itself not only with the simulation of current *vs.* voltage characteristics, but also includes, e.g., the subfields of modeling of optoelectronic devices [10], quantum effects [11, 12], magnetic devices [13], and the effects of radiation [14].

Multiple devices can be interconnected to form an electrical circuit, and its characteristics can be simulated with *circuit TCAD*. The categories of device and circuit TCAD are intrinsically linked, since, e.g., the electrical characteristics obtained from device TCAD can be used to construct compact models which more efficiently enable the simulation of connected devices [15]. Additionally, circuit TCAD encompasses the modeling of the interconnects linking multiple devices [16] and the extraction of parasitic parameters [17].

The third category is dedicated to modeling and simulation of the fabrication processes of semiconductor devices. This category is called *process TCAD*, and this thesis situates itself broadly within its scope. Both historically [18] and more recently [19], these simulations have attracted major research and industrial attention.

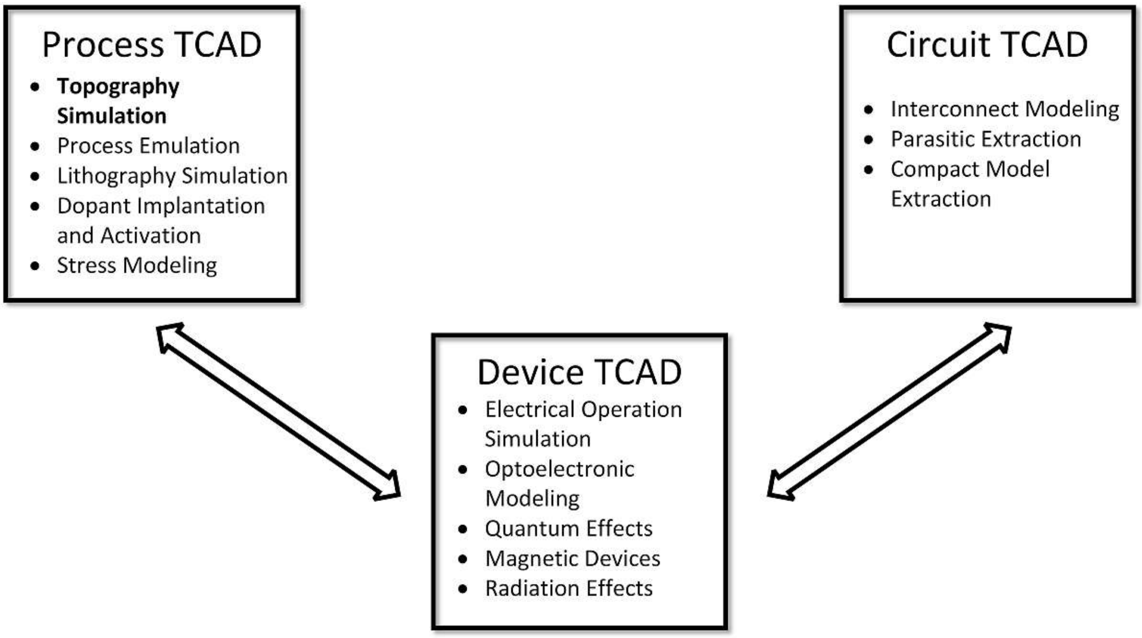

Figure 1.1: Illustration of the three main categories of TCAD including related subfields.

This is because they stand at the beginning of the chain of TCAD investigations. Process TCAD is a fundamental enabler of modern micro- and nanodevices, since it not only provides physically realistic structures for device simulation, but also directly deals with the most costly aspect of the semiconductor value chain [20, 21]: The manufacturing process.

There are several processes required for the manufacturing of a modern semiconductor device, all of them requiring attention from process TCAD. Historically, substantial development attention has been placed on processes which directly impact the electrical characteristics of the devices, such as dopant implantation [22] and diffusion [23], as well as oxidation [24] and stress accumulation [25]. Since the desired outcome is the study of electrical phenomena, comparatively little attention had been paid to the precise shape of the devices.

More recently, however, precise control of the final shape of the processed device has become a more salient issue [26]. The increased miniaturization of devices has led to the development of non-planar structures such as fin field-effect transistors (FinFETs) and gate-all-around (GAA) transistors which have decreased tolerances and require more control of the fabrication processes [27]. Also, the MEMS and nanoelectromechanical systems (NEMS) revolution involves systems where the shape is at the forefront [28], and the emergence of superconductor electronics requires high authority over the involved Josephson junctions [29]. Thus, the sub-field of *topography simulation* has garnered increase importance, since it concerns itself with the simulation of processes which dictate the final shape, i.e., the topography, of the device.

There are several processes which impact the final device structure. Centrally, there are the complementary processes of *deposition* [30] and *etching* [31], i.e., the addition and removal of material, respectively. These processes can be further described according to the specificities of the involved reactor. For example, the deposition of material in a vacuum reactor through physical processes is called physical vapor deposition (PVD) [32], while the deposition exploiting chemical reactions is named chemical vapor deposition (CVD) [33]. In etching, there is a broad distinction between liquid-phase reactors, named wet etching, and vapor- or plasma-phase processes, called dry etching [7].

Etching and deposition are not the only processes which affect the structure. For example, chemical-mechanical planarization (CMP) [34] and oxidation [35] have a severe impact on the final shape. Additionally, there is the process of lithography, i.e., the printing of patterns on photoresist material through light [36]. However, due to its specialized nature, lithography modeling is often considered a separate sub-field [37]. The simulation of the involved reactors is also a separate domain of expertise [38].

Since the simulation of the reactors is not directly involved in conventional topography simulation, two different geometrical scales can be naturally defined. The *reactor-scale* involves the entire reactor, focusing on, e.g., the generation of active reactants, as well as their characteristics and distributions across the entire wafer [38]. Topography simulation operates, instead, at the *feature-scale*, where only a small region of interest is investigated. Small regions are, for example, a single transistor [39], an individual MEMS structure [40], or even somewhat larger structures such as three-dimensional (3D) NAND channel holes [26]. These two regions are linked by an abstract region of the feature-scale named the *source plane*, where the outputs of a reactor-scale analysis, such as reactant species incoming angular distribution functions, become fixed inputs for the topography simulation.

Topography simulation is composed of two major elements. First, it must be able to robustly describe evolving surfaces. This is particularly challenging for the aforementioned processing techniques since changes in the topology can occur. For example, during etching, a layer might be completely pierced; or a hole might be covered leaving an air-gap during deposition. These changes are exceedingly challenging to model using conventional explicit surface representations such as polyhedral meshes [41]. Therefore, implicit surfaces and, crucially, the level-set (LS) method have emerged as the standard surface representation and advection method, respectively, for topography simulation [42].

In addition to the surface representation, the second major element is the determination of the surface advection velocity distribution. In other words, the physical and chemical phenomena involved with the distribution of reactants, i.e., the *reactive transport*, must be modeled. Reactive transport modeling entails the calculation of the trajectories of *particles* through the simulation domain as well as their interaction with the evolving surface. Such particles can directly represent the reactant species and the respective chemical interactions. However, a particle can also be an aggregate of several reactants into a single representation. This is often the case for processes involving plasmas [43], since the involved chemistry is not only complex but also often unknown.

For example, several polymerizing species can be aggregated into an effective particle which represents the formation of the polymer protective film in reactive ion etching (RIE).

Nonetheless, if a precise reactor model is available and the possible physical and chemical reactions are known, the reactive transport can in principle be directly modeled [44]. In practice, however, this is exceedingly difficult. Even for very established processes, there is still a very active scientific debate over the involved surface phenomena [45]. Additionally, the reactors, in particular those involving plasmas, are exceptionally complex, therefore, predictive modeling is not always possible.

This motivates the development of *phenomenological models*. That is, models which attempt to capture the most essential phenomena known from physical-chemical intuition [46]. Since these models are intrinsically simplified, they necessarily involve parameters which must be calibrated to experimental data. Nevertheless, if these models are properly justified, the extracted parameters can be meaningful and, thus, shine light into the processing conditions. Therefore, in the spirit of Occam's Razor [47], a phenomenological model must be constructed as parsimoniously as possible to adequately capture reality. Phenomenological modeling is fundamentally different to *process emulation* [48], where the geometric properties gathered from experiments are directly described without involving physical insight. This direct description of properties is also named *geometrical modeling*.

In this attitude of simplicity, a further subdivision are the so-called *single-particle models*. In them, the entire physical and chemical complexity of the reactants is abstracted into a single representative phenomenological species, whether representing a chemical species or a phenomenological aggregate. Although for some processes a larger number of phenomenological particle species are necessary even for the simplest possible model [43], for several others a single-particle representation is sufficient. In fact, from the point of view of phenomenological modeling, a simpler model with fewer species is more desirable, since more information can be gained from the parameters.

The choice of a minimal number of species requires deep knowledge of the involved processing step. In general, single-particle models are adequate for processes where one chemical species is the limiting factor, even if different species might be involved in the reaction. For example, low-bias plasma etching [49], atomic layer processing (ALP) in the single-reactant limited regime [30], CVD [50], and PVD [51] are ideal applications to phenomenological single-particle modeling.

1.1 Research Goals

The research goals of this thesis are, in summary, the development of sufficiently accurate phenomenological single-particle reactive transport models for topography simulation and their application to relevant etching and deposition processes. These models must be robust enough to be accurate without resorting to reactor or first-principle calculations. Simultaneously, the number of parameters should be kept as low as possible to maximize their chemical interpretability.

With robust and accurate models, direct modeling, i.e., the reproduction of experimental topographies, is possible. This enables the generation of physically-sound device structures which are of great importance to device engineers. In addition, a phenomenological model should enable inverse modeling: The extraction of useful chemical information from experimental topographies. Finally, the application of these models must be able to provide experimentally-actionable input to process developers, that is, phenomenological modeling must be demonstrated as a constituent of a larger optimization effort.

Research Setting

The research presented in this thesis has been conducted within the scope of the Christian Doppler Laboratory for High Performance TCAD at the Institute for Microelectronics, TU Wien. This Laboratory is a long-term collaboration pursuing application-oriented basic research between the Institute for Microelectronics and Silvaco Europe Ltd., a leading commercial provider of electronic design automation (EDA) and TCAD tools, jointly funded by the Christian Doppler Association and the involved company. The Laboratory is led by Prof. Josef Weinbub.

The research collaboration regarding low-bias sulfur hexafluoride (SF_6) plasma etching of silicon (Si) for microcavity resonators has been established in collaboration with the experimental teams led by Prof. Ulrich Schmid of the Institute of Sensors and Actuator Systems, TU Wien, and by Dr. Michael Trupke of the Vienna Center for Quantum Science and Technology (VCQ) at the Faculty of Physics, University of Vienna. The computational results in Chapter 6 were obtained using resources from both the Vienna Scientific Cluster (VSC) and from the computing infrastructure of the Institute for Microelectronics.

1.2 Outline

This thesis follows the didactic structure of first introducing concepts and then expanding them into applications. Thus, the ordering of the chapters does not necessarily follow their chronological order of development and original publication. Instead, their arrangement is chosen to provide a more natural narrative for the reader.

Initially, Chapter 2 briefly reviews topography simulation and the basic categories of approaches to calculate the reactive transport. After this broad overview, one specific approach to generate one-dimensional (1D) models, Knudsen diffusion, is presented in Chapter 3 in its historic context with a focus on clarifying lingering misconceptions. Knudsen diffusive transport is re-derived using a more modern formulation including an analogy to radiative heat transfer to incorporate more physical phenomena as well as two brief applications.

Then, attention is shifted to applying the presented models to specific etching and deposition processes and to the adequate interpretation of the model parameters. First, Chapter 4 presents an application of Knudsen diffusive transport models to the thermal ALP, including its novel integration with LS based topography simulation.

Chapter 5 investigates the process of low-bias SF_6 plasma etching of Si, evaluating the applicable approaches proposed in Chapter 2 and proposing a new empirical relationship between experimental topographical measurements and the phenomenological model parameters.

Finally, Chapter 6 culminates the thesis by performing an even deeper investigation of the low-bias SF_6 plasma etching process in order to optimize an actual device: Silicon microcavity resonators. The issue of requiring manual calibration is addressed with a developed custom feature detection and automatic calibration procedure. Finally, the power of topography simulation is showcased in practice by exploring the impact of different etch time regimes on parameters linked to device performance. The concluding remarks and outlook for possible future research directions are discussed in Chapter 7.

Chapter 2

Review of Reactive Transport Models for Topography Simulation

The ultimate goal of topography simulation is to guide the development of semiconductor devices through a physically realistic description of structures after etching and deposition. To achieve this goal, an accurate topography simulation must possess two fundamental characteristics: A method for robustly representing the advecting surfaces and realistic models describing the local surface speeds stemming from the complex reactive transport of the involved reactants. This chapter presents a review of these reactive transport models including their context within topography simulation.

Firstly, a short overview of the chosen method for surface advection, the level-set (LS) method, is presented. Particular attention is placed on the term linking the topography simulation with reactive transport modeling: The velocity field $v(\vec{r}, t)$. Afterward, a review of Langmuir adsorption kinetics is given which is necessary for connecting the particle fluxes with the local surface state. Finally, an overview of the explored approaches to calculate the local particle fluxes is provided. Importantly, the flux calculation and the chemical state of the surface might mutually interact which is the source of complex reactive transport behavior. The interplay of these elements in one iteration cycle of the topography simulation is visually represented in Fig. 2.1. The evaluation and application of reactive transport models to specific etching and deposition problems is discussed in subsequent chapters of this dissertation.

2.1 The Level-Set Method

The fundamental challenge of surface advection algorithms in semiconductor manufacturing is that the involved surfaces undergo very complex processes [41]. In particular, the surfaces can undergo changes in topology, such as the complete perforation of a material layer after an etch step, which make explicit surface representations exceedingly difficult [42]. Although cell-based representations can also handle such topological changes [52], they lack sufficient information about the surface position and are thus inaccurate in their calculations, e.g., curvatures and normals [42, 53].

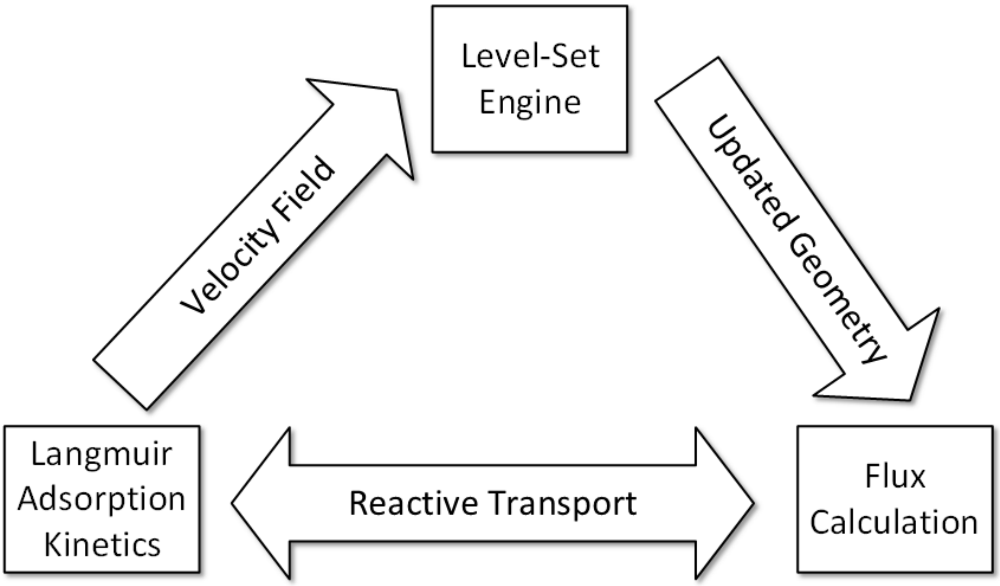

Figure 2.1: Flowchart depicting one iteration cycle of an LS based topography simulation. The two-headed arrow linking the flux calculation to Langmuir adsorption kinetics indicates their mutual dependence in the calculation of the reactive transport.

Thus, the accurate LS method has emerged as a standard in topography simulation for process technology computer-aided design (TCAD). It is widely implemented in commercial simulators, such as Synopsys' Sentaurus Topography [54], Silvaco's Victory Process [55], and the Florida object-oriented multipurpose simulator (FLOOXS) [29, 56], as well as open-source tools like ViennaTS [57].

The LS method is based on an implicit surface representation. Unlike explicit representations, where surface points and connecting elements are directly stored, in this implicit representation a function $\phi(\vec{r},t)$ is defined for all points in the domain. In the LS method [58, 59], the surface S bounding a volume V is recovered from the property $\phi(\vec{r},t)=0$ for all points on S. That is, S is described by the zero level-set of $\phi(\vec{r},t)$, as long as $\phi(\vec{r},t)>0$ on the outside of V and $\phi(\vec{r},t)<0$ on its inside. A common choice of $\phi(\vec{r},t)$ for describing surfaces resulting from semiconductor processing [60, 61] is that of the signed-distance function (SDF), that is, the distance d between $\vec{r}$ and S with the necessary sign:

$$\phi(\vec{r},t)=\begin{cases}-d, & \vec{r}\in V\\ 0, & \vec{r}\in S\\ d, & \vec{r}\notin V\end{cases} \tag{2.1}$$

The evolution of the surface described in Eq. (2.1) is driven by a velocity field $\vec{v}(\vec{r},t)$. The following Hamilton-Jacobi equation can then be derived for the evolution of the surface [58, 62]:

$$\frac{\partial\phi(\vec{r},t)}{\partial t}+v(\vec{r},t)\,|\nabla\phi(\vec{r},t)|=0 \tag{2.2}$$

To obtain a numerical solution, Eq. (2.2) is conventionally discretized on a regular rectangular grid with spacing Δx. The involved partial derivatives are then approximated using finite difference schemes [63]. Additionally, it should be remarked that there is a difference between *fast marching* and *narrow band* LS methods [42]. In the former, the values of $\phi(\vec{r}, t)$ are stored in the entire domain, thus requiring the fast marching method to propagate the values from the interface [64], whereas in the latter only values near the surface are stored [65]. Both methods have found application (e.g., fast marching and narrow band respectively in Silvaco's Victory Process [55] and ViennaTS [57]) and are used in this dissertation. Although developments in fast marching methods are an area of activity for researchers of the Christian Doppler Laboratory for High Performance TCAD [66, 67], a more detailed description is outside the scope of the presented research.

Instead, the principal focus of this dissertation is the study of phenomenological methods for the construction of the term $v(\vec{r}, t)$. For a reactive transport model to be useful for topography simulations, it should ultimately generate a velocity field, i.e., etch or growth rates must be determined for the whole surface. It is noteworthy that, for the method described by Eq. (2.2), only the normal component $v(\vec{r}, t)$ of the proper velocity field $\vec{v}(\vec{r}, t)$ is necessary. Therefore, it would be more accurate to describe $v(\vec{r}, t)$ as a *speed* field. However, for consistency with the established literature, this dissertation will hitherto refer to $v(\vec{r}, t)$ as *the velocity field*. When the involved process results in material deposition, the convention is that $v(\vec{r}, t)$ carries a positive sign. Then, $v(\vec{r}, t)$ can also be denoted as the growth rate $GR(\vec{r}, t) = v(\vec{r}, t)$. Etching processes result in an etch rate with a negative sign, i.e., the etch rate $ER(\vec{r}, t) = -v(\vec{r}, t)$.

2.2 Langmuir Adsorption Kinetics

The process of etching or deposition involves physical and chemical transformations of the evolving surface. Thus, a crucial element in the overall simulation approach is the choice of an adequate model for the interaction of the particles with the surface. Additionally, such a reactive transport model must be connected with a velocity field, as discussed in Section 2.1. In the context of phenomenological modeling, said model should be as simple as possible to capture the relevant physical and chemical processes, therefore, coarse approximations are permitted as long as the simulation outcomes can be related to experiments.

The established approach for phenomenological modeling of surfaces builds upon the seminal work by Irving Langmuir in 1918 [68]. The key idea behind Langmuir adsorption kinetics is that impinging vapor species adsorb upon interacting with the force fields stemming from the surface atoms. Importantly, such force fields are not explicitly investigated, instead their properties are only *phenomenologically* described regarding general and approximate properties of the reactant-surface system. These forces are assumed to be very short in range, thus the impinging reactants adsorb forming a film with at most one monolayer. If such forces are relatively weak, the reactant can thermally evaporate spontaneously, leading to a reversible kinetic behavior.

This comparatively weak and reversible interaction is named *physisorption* (or physical adsorption), in contrast to *chemisorption* where the chemical bonds change more permanently [69]. Due to large unknowns present in phenomenological modeling, the limit between physisorption and chemisorption is often tenuous, however, insights from Langmuir modeling are usually associated with the physisorption regime.

Langmuir adsorption kinetics starts by assuming that the surface has a homogeneous distribution of surface sites with area s_0 which are available to interact with the impinging reactants. These surface sites are allowed to be partially saturated by the condensed vapor, leading to the fundamental concept of the *surface coverage* Θ: The local ratio of occupied to available surface sites, so that Θ=0 for an unoccupied, or clean, surface and Θ=1 for a fully-saturated site. From that, Langmuir postulates [68] a simple relationship for competitive adsorption and desorption

$$\frac{1}{s_0}\frac{d\Theta}{dt} = \overbrace{\Gamma_{\text{imp}}\beta_0(1-\Theta)}^{\text{adsorption rate}} - \overbrace{\Gamma_{\text{ev}}\Theta}^{\text{desorption rate}}\,, \tag{2.3}$$

where Γ_{imp} is the local flux of impinging particles, whose calculation is discussed in Section 2.3; Γ_{ev} is the evaporation flux for a fully covered surface; and β_0 is the *clean surface sticking coefficient*, i.e., the probability of an impinging species to adsorb on an unoccupied surface (Θ=0). From the steady-state limit of Eq. (2.3) the standard Langmuir adsorption isotherm is recovered [69]. Although such limit is very often assumed in applications for semiconductor processing [43], it fails in many applications where the transient times are relevant, such as in atomic layer deposition (ALD). More recent studies have suggested alternative forms for Langmuir adsorption, including a second-order term in Θ [70, 71]. Thus, Eq. (2.3) can accurately be named *first-order reversible Langmuir kinetics*.

There are two intrinsically empirical parameters in Eq. (2.3): Γ_{ev} and β_0. From those, β_0 carries the most physical and chemical significance. Firstly, it implicitly considers the stoichiometry of the surface reaction. Although stoichiometric factors can be explicitly written in a Langmuir-type equation, they are not always observed in reality due to steric hindrance [68]. That is, the impinging species might effectively be larger than the underlying surface sites, preventing further molecules to attach even though stoichiometric considerations would otherwise permit. Additionally, β_0 connects the surface state with the transport of reactants given by Γ_{imp}, since a reactant which does not adsorb is free to propagate and perhaps impinge on a different surface element. For these first-order kinetics, the adsorption probability, i.e., the full sticking coefficient, is [30]

$$\beta = \beta_0(1-\Theta)\,, \tag{2.4}$$

and the reflection probability is then simply $1-\beta$.

Finally, this surface kinetics relationship brings additional insight into the reactive transport calculation. Already from early experiments from Knudsen [72, 73] and Langmuir [74], it has been observed that the molecules which do not adsorb are reflected, however, they do not scatter away specularly. Instead, they follow a cosine distribution, that is, their reflection direction is independent of the incoming path.

This observation is interpreted as evidence of a very fast mechanism such that during the reflection process the molecule thermalizes with the surface and loses information about its previous state. In semiconductor processing, this cosine dependence usually holds for uncharged reactants, while accelerated ions show specular reflections [75].

The Langmuir adsorption kinetics shown in Eq. (2.3) is valid for a single particle. Due to its phenomenological nature, such model can be employed regardless if the particle represents a well-defined chemical species or a phenomenological aggregate of multiple reactants. This dissertation focuses on semiconductor processing steps which can be effectively modeled using a single-particle. Nonetheless, it is notable that the semiconductor process modeling community has developed and applied multiple-particle variants of such models [43, 76, 77, 78]. La Magna *et al.* [43] propose, e.g., a steady-state, first-order reversible Langmuir kinetics for the competing adsorption of neutrals and polymers under ion bombardment for reactive ion etching (RIE).

Regardless of the number of involved chemical species, as discussed in Section 2.1 and Eq. (2.2), the final goal of describing the surface state is the determination of a velocity field $v(\vec{r}, t)$. However, Langmuir adsorption kinetics only evaluate small changes in the surface structure of up to a monolayer. Thus, the construction of a coverage-dependent velocity field $v(\Theta(\vec{r}), t)$ requires careful consideration as it involves substantial approximations. In the LS method, the velocity field is assumed to be constant as the surface advects while the Courant-Friedrichs-Lewy (CFL) condition is satisfied. The CFL condition is necessary in order to guarantee numerical stability [79], so after each CFL-limited advection step, the velocity field is recalculated. In summary, for fast marching LS methods, the surface advection step is limited to a single grid spacing Δx, while for narrow band methods it is limited to $0.5 \cdot \Delta x$ [53]. Therefore, a constructed $v(\Theta(\vec{r}), t)$ is only valid during an advection step if the following conditions are met: i) Transport equilibrates much more quickly than the surface advection speed, such that there are no changes in local impinging fluxes $\Gamma_{\mathrm{imp}}(\vec{r})$ during the advection step; and ii) Δx is small enough that changes in the distribution $\Theta(\vec{r})$ due to the evolving geometry are negligible. For example, Yanguas-Gil [30] proposes the following form for the growth rate of chemical vapor deposition (CVD) from a single impinging reactant

$$v(\Theta(\vec{r}), t) = GR(\Theta(\vec{r}), t) = \frac{M_m}{\rho} \Gamma_{\mathrm{imp}}(\vec{r}, t) \beta(\Theta) \,, \tag{2.5}$$

where M_m is the incorporated mass per impinging molecule and ρ is the film density.

2.3 Approaches to Calculate Local Fluxes

In Section 2.2, all terms of Langmuir adsorption kinetics in Eq. (2.3) are discussed except for the local impinging particle flux $\Gamma_{\mathrm{imp}}(\vec{r})$. Its calculation is the focus of this section, where four classes of methods are presented: Constant flux, bottom-up visibility calculation, top-down pseudo-particle tracking, and one-dimensional (1D) models. In particular, the relationship mediated by the coverage-dependent reflection given by Eq. (2.4) between the local fluxes and the surface state is explored, including required approximations.

At the heart of these flux calculation approaches are considerations of the flow regime. This analysis requires defining two characteristic lengths of the transport processes: The mean free path λ, given by the probability of particle-particle collisions; and a representative length of the geometry d, e.g., the diameter if the geometry is a cylinder. From those, the Knudsen number can be constructed as [30]:

$$\mathrm{Kn} = \frac{\lambda}{d}\,. \tag{2.6}$$

Kn is a measure of the relative probability of a particle-particle collision to a particle-geometry collision. Therefore, the *molecular flow* regime is achieved for high Knudsen numbers, typically assumed to be $\mathrm{Kn} > 10$ [80], i.e., a collision with the geometry is at least ten times more likely than that with another particle. Many semiconductor processing techniques, particularly those involving gas- or plasma-phase, occur in a high vacuum chamber and thus in the molecular flow regime. Therefore, this regime is conventionally assumed for the flux calculation, although allowances for the *transitional flow* regime ($10^{-1} < \mathrm{Kn} < 10$) are discussed for the top-down and 1D approaches.

All calculation methods of $\Gamma_{\mathrm{imp}}(\vec{r})$ require a reference flux value Γ_{source} which is the reactant flux at an imaginary boundary between the feature-scale and the reactor-scale called the source plane. Although Γ_{source} can be experimentally inferred [43] or calculated with detailed reactor models [38, 81], another approach is to normalize the impinging flux to the source flux, i.e.,

$$\hat{\Gamma}_{\mathrm{imp}}(\vec{r}) = \frac{\Gamma_{\mathrm{imp}}(\vec{r})}{\Gamma_{\mathrm{source}}}\,. \tag{2.7}$$

This is viable since Γ_{source} is also, by definition, the local flux received by a fully visible surface site (c.f. point $\vec{r}_2$ in Fig. 2.5). Therefore, instead of performing a complex calculation of Γ_{source}, $\hat{\Gamma}_{\mathrm{imp}}(\vec{r})$ is calculated in its normalized form directly. Then, rather than relying on a complex formula such as Eq. (2.5), the velocity field can be calculated from the (etch or deposition) plane wafer rate PWR. An example of such field is

$$v(\vec{r},t) = \hat{\Gamma}_{\mathrm{imp}}(\vec{r},t) \cdot PWR \tag{2.8}$$

which can be advantageous since the PWR can be straightforwardly related to experimental measurements. For instance, lithography masks often include a large exposed test structure which is expected to receive the maximum amount of reactants $\hat{\Gamma}_{\mathrm{imp}} = 1$ and be etched with the PWR.

Lastly, it is noteworthy that the incoming flux might be characterized not only by its magnitude but also by an angular and energy distribution, particularly when ion acceleration due to plasma interactions are involved. The bottom-up and top-down methods, as discussed below, can take these distributions into account for the local flux calculations. However, the focus of this dissertation is the study of thermal processes, that is, those where there is no preferential incoming or reflection direction. Nonetheless, Eq. (2.7) is always valid if Γ_{source} is interpreted as the absolute value of the flux, since a fully visible element will always receive Γ_{source} regardless of the source angular and energy distribution.

2.3.1 Constant Flux

The most straightforward approach for the reactive transport calculation is the constant flux approximation, illustrated in Fig. 2.2. In this approach, all exposed surface elements receive the same Γ_{source}, thus the velocity field is strictly a function of local material properties. Although simple, this method still requires some computational effort since only the exposed surfaces must be detected, disregarding, e.g., eventual voids [82, 83].

This apparent simplicity can obfuscate the deeper physical assumptions necessary for the application of this reactive transport approach. One situation which enables this approach is the *surface-controlled regime* [84], which is commonly observed in anisotropic wet etching [85, 86]. In it, there must be a large enough availability of reactants such that all exposed surface sites become fully saturated. Thus, according to Eq. (2.4), the sticking coefficient approaches zero ($\beta \to 0^+$). Additionally, any local depletion due to the ongoing surface-chemical reactions is immediately replenished by transported reactants. Thus, any anisotropy is strictly due to local surface-controlled phenomena and the constant flux approach holds.

Accordingly, the velocity field is constructed with strictly local parameters. For anisotropic wet etching, the most common surface-controlled phenomenon is the crystallographic orientation dependence of the etch rate [85]. Thus, the velocities are a function of the surface normal $\vec{n}$, and the anisotropy is only due to *local* surface properties, notably $\vec{n}$, and not due to differences in flux, as long as the surface-controlled regime is experimentally maintained. One approach for determining this locally-varying velocity field for crystallographic orientation-dependent phenomena, proposed by Toifl *et al.* [87], involves interpolating between the crystal directions $\vec{m}_i$

$$v(\vec{n}) = v_0 + \sum_i \alpha_i \langle \vec{n}, \vec{m}_i \rangle^{\omega_i} H(\langle \vec{n}, \vec{m}_i \rangle)\,. \tag{2.9}$$

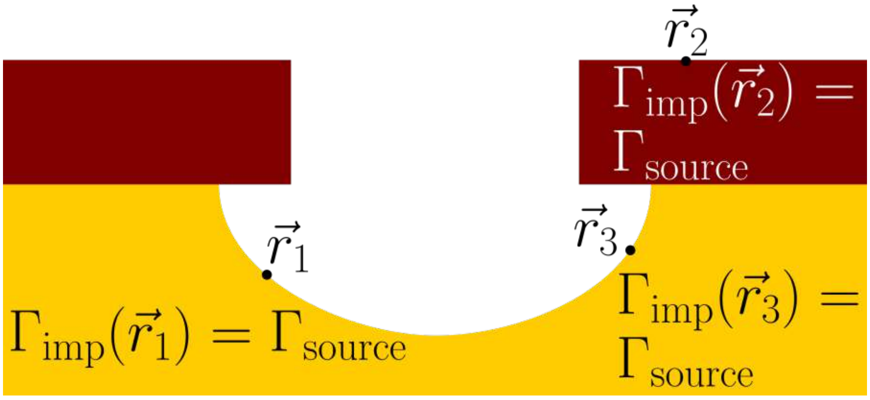

Figure 2.2: Illustration of constant flux approach to reactive transport calculation. All exposed surface elements, regardless of involved material, receive the same impinging flux Γ_{imp} equal to the source flux Γ_{source}. Adapted from Aguinsky *et al.*, *Solid State Electron.* 191, (2022) p. 108262. [88], © The Authors, licensed under the CC BY 4.0 License, `https://creativecommons.org/licenses/by/4.0/`.

In Eq. (2.9), H is the Heaviside function, $\langle \cdot, \cdot \rangle$ is the inner product, v_0 is the isotropic component of the velocity field, and α_i and ω_i are parameters which can be constructed from considering the etch rates in the $\vec{m}_i$ directions. An example of Eq. (2.9), parameterized to the etching of sapphire from a mixture of sulfuric acid to phosphoric acid on a 3:1 ratio (M3-1) at 503 K, is shown in Fig. 2.3. The effect of applying this velocity field to an array of cones is shown in Fig. 2.4, highlighting the strong profile variation strictly due to local properties.

However, surface saturation is not the only condition in which the constant flux approximation is valid. In isotropic wet etching, it is commonly necessary to establish the *transport-controlled regime*, where the etching is limited by rate of reactant transport. Otherwise, an oversupply of reactants can lead to more complex surface phenomena and, thus, undesired anisotropy [84]. Therefore, there is a trade-off which must be carefully balanced to achieve true isotropy: Excessive reactant supply can lead to anisotropy from surface reactions, while insufficient supply can lead to anisotropy due to a gradient in the flux distribution.

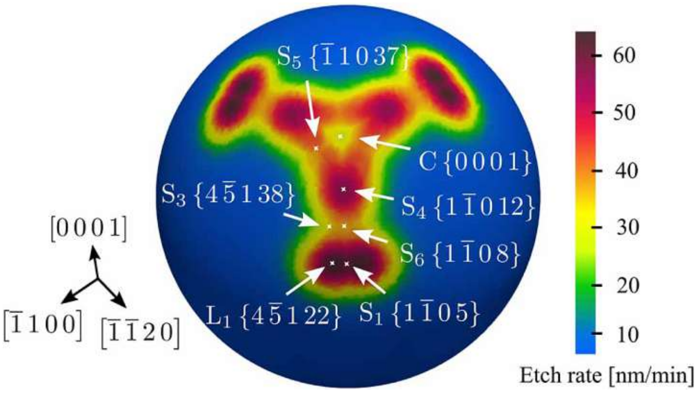

Figure 2.3: Parameterization of Eq. (2.9) to anisotropic wet etching of sapphire using the M3-1 mixture [87]. Reprinted from Toifl *et al.*, *Semicond. Sci. Technol.* 36, (2021) p. 045013. [87], © The Authors, licensed under the CC BY 4.0 License, `https://creativecommons.org/licenses/by/4.0/`.

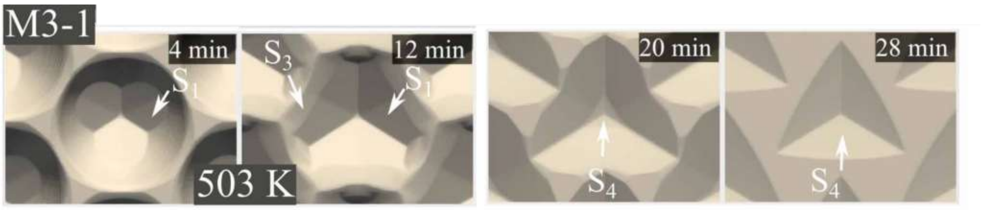

Figure 2.4: Time evolution of an array of cones of sapphire under anisotropic wet etching on the surface-restricted regime using the parameterization of the velocity field from Fig. 2.3 [87]. Adapted from Toifl *et al.*, *Semicond. Sci. Technol.* 36, (2021) p. 045013. [87], © The Authors, licensed under the CC BY 4.0 License, `https://creativecommons.org/licenses/by/4.0/`.

Therefore, achieving a truly isotropic wet etching process, wherein the constant flux approximation must necessarily hold, is fairly complex. Either a surface-controlled reaction with no spurious anisotropic component or a finely-balanced transport-controlled regime must be constructed. However, if this is achieved, the topography simulation becomes somewhat trivial, and the velocity field can be expressed as

$$v(\vec{r},t) = ER_{\text{material}}\,, \tag{2.10}$$

where ER_{material} represents the measurable isotropic etch rate of an exposed material.

2.3.2 Bottom-Up Visibility Calculation

Moving beyond the straightforward constant flux approach, the bottom-up calculation adds nuance to the reactive transport by incorporating *visibility effects*. This is represented in Fig. 2.5, where a fully visible surface element ($\vec{r}_2$) still receives Γ_{source}, while a partially obstructed element ($\vec{r}_1$) receives a smaller flux due to reduced visibility Γ_{vis}. Importantly, visibility is here defined as a continuous variable between 0 and Γ_{source}, while exposure, as defined in Section 2.3.1, is strictly binary. Thus, the visibility-dependent flux can be stated as an integral over the entire source plane [61]

$$\Gamma_{\text{vis}}(\vec{r}) = \int_{\text{source}} \Gamma_{\text{source}}(\vec{r}-\vec{r}\,')\langle\vec{n},\vec{n}\,'\rangle d\vec{r}\,'\,, \tag{2.11}$$

where $\vec{r}$ and $\vec{n}$ are the position and unit normal vector of the point where the flux is evaluated, respectively; and $\vec{r}\,'$ and $\vec{n}\,'$ are the positions and normals at the source plane over which the integral iterates. Since the flux calculation is performed at each surface element independently, this method is denoted as *bottom-up*.

In Eq. (2.11), the source flux has an angular dependence on the outgoing direction $\vec{r}-\vec{r}\,'$, thus $\Gamma_{\text{source}}(\vec{r}-\vec{r}\,')$ must be constructed attentively so that the total integral is correctly normalized. An isotropic source flux distribution has to follow a cosine distribution, i.e. [89]

$$\Gamma_{\text{source,isotropic}}(\vec{r}-\vec{r}\,') = \Gamma_{\text{source}}\frac{1}{\pi}\frac{\langle(\vec{r}-\vec{r}\,'),\vec{n}\,'\rangle}{||\vec{r}-\vec{r}\,'||}\,, \tag{2.12}$$

so that a fully visible surface element receives a flux with magnitude Γ_{source}. Additionally, Eq. (2.11) enables more complex source flux distributions such as those more vertically focused due to plasma-accelerated ions which can be modeled with a κ-power cosine distribution

$$\Gamma_{\text{source,focused}}(\vec{r}-\vec{r}\,') = \Gamma_{\text{source}}\frac{\kappa+1}{2\pi}\frac{\langle(\vec{r}-\vec{r}\,'),\vec{n}\,'\rangle^{\kappa}}{||\vec{r}-\vec{r}\,'||}\,. \tag{2.13}$$

The largest challenge imposed by Eq. (2.11) is the solution of the involved integral. Nonetheless, the lack of reflections greatly simplifies this challenge, since each surface position $\vec{r}$ only requires computing the contributions by the $\vec{r}\,'$ positions on the source plane which has a constant and comparatively small number of elements.

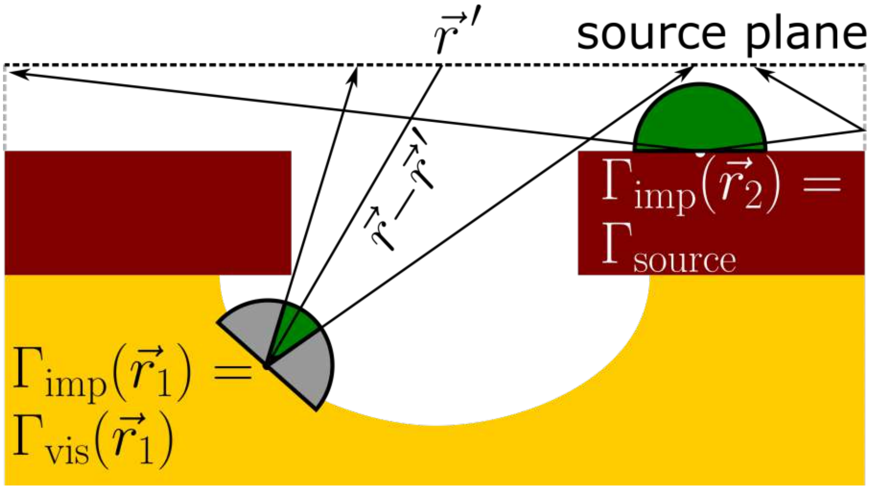

Figure 2.5: Illustration of the bottom-up visibility calculation showing the source plane, the imaginary region where reactor phenomena is linked to the feature-scale, and reflective boundary conditions. The surface element with coordinates $\vec{r}_2$ is fully visible, therefore it receives Γ_{source}, while the one at $\vec{r}_1$ receives a reduced flux due to visibility Γ_{vis}. The arrows indicate rays which are cast from the surface to sample the hemispherical visibility. Adapted from Aguinsky *et al.*, *Solid State Electron.* 191, (2022) p. 108262. [88], © The Authors, licensed under the CC BY 4.0 License, `https://creativecommons.org/licenses/by/4.0/`.

Thus, this integral can be directly solved on the LS grid if a function which determines if $\vec{r}$ and $\vec{r}\,'$ are mutually exposed is available [82, 90]. More recently, ray-tracing schemes have been developed by discretizing the hemisphere above each $\vec{r}$ and querying for intersections with the source plane. For example, efficient ray-tracing kernels can be used by extracting explicit meshes from the LS grid [91]. Additional performance improvements have been achieved by adaptive sampling of the hemisphere [92] and by restricting the number of surface elements wherein the flux is calculated [93].

This bottom-up approach has critical implications for the reactive transport modeling. As previously stated, Eq. (2.11) does not include reflections, therefore, it can only model processes with $\beta = 1$. This puts the bottom-up visibility calculation in stark contrast to the constant flux approach which captures processes with near-zero sticking coefficient. Thus, these two approaches can be understood as the two extremes of reactive transport with constant sticking coefficient. There are several physical processes which are commonly modeled with a sticking coefficient of unity, most notably physical vapor deposition (PVD). In this category of processing techniques, the material to be deposited is vaporized and transported to the feature, where it physically interacts (i.e., without changes in its chemical composition) and forms a film [32]. If these interactions are energetically favored and occur with high efficiency without re-sputtering, then they can be adequately modeled with $\beta = 1$ [30, 94]. However, more complex phenomena in PVD such as grain boundary formation, might require different values of β [51].

To overcome this limitation on β, it is possible to reformulate Eq. (2.11) to include not only the direct visibility contributions, but also the effect of the indirect flux Γ_{ind} reflected by the entire geometry onto $\vec{r}$ as [90]

$$\Gamma_{\text{imp}}(\vec{r}) = \Gamma_{\text{vis}}(\vec{r}) + \Gamma_{\text{ind}}(\vec{r}) =$$
$$\beta(\vec{r}) \int_{\text{source}} \Gamma_{\text{source}}(\vec{r}-\vec{r}\,')\langle\vec{n},\vec{n}\,'\rangle d\vec{r}\,' + \int_{\text{geometry}} (1-\beta(\vec{r}\,'))\Gamma_{\text{refl}}(\vec{r},\vec{r}\,')\langle\vec{n},\vec{n}\,'\rangle d\vec{r}\,', \quad (2.14)$$

where Γ_{refl} is the reflected flux which is naturally itself a function of the impinging flux at $\vec{r}\,'$. That is, for each $\vec{r}$, the integration variable $\vec{r}\,'$ iterates not only over the source plane but also over the surface. Thus, Eq. (2.14) is a true integral equation, since the local impinging flux depends on the distribution Γ_{imp} over the entire geometry. This equation is exceedingly challenging to solve, since it scales with the square of the number of surface sites, as each site must compute the contributions of the whole geometry. It can be solved for arbitrary source and reflection distribution functions iteratively over multiple bounces [41]. More commonly, Eq. (2.14) is solved under the stricter approximations of constant β and isotropic source and reflection distributions, in what is often named a *radiosity* approach [90, 95, 96, 97], discussed in more detail in Section 2.3.4. Nonetheless, the quadratic dependence on the number of surface elements imposes stringent performance limitations to this approach even on state-of-the-art computing systems, since the entire radiosity matrix must be calculated, stored and inverted.

2.3.3 Top-Down Pseudo-Particle Tracking

As discussed in the previous sections, the constant flux approach is valid in the $\beta \rightarrow 0^+$ regime. Furthermore, the bottom-up visibility calculation straightforwardly captures $\beta = 1$. It is thus patently necessary to introduce a method which is able to capture reactive transport for intermediate values of β, as well as more complex physical phenomena beyond the constant sticking coefficient approximation. Although Eq. (2.14) condenses the involved physical and chemical phenomena, its direct solution is untenable for the general case due to the computational complexity of the integral equation.

Therefore, a more computationally efficient approach is the Monte Carlo tracking of pseudo-particles sampling of this integral equation, as illustrated in Fig. 2.6. These pseudo-particles are named as such because they should only be interpreted as discrete samples of the continuum integral equation. They are not representations of individual particles, e.g., chemical reactants or ions, and are, therefore, unable to capture molecular-scale phenomena. This Monte Carlo method equally splits the product of Γ_{source} and the source plane area A_{source} (i.e., the *total power*, in analogy to radiative heat transfer [98]) among N_{part} pseudo-particles to achieve an initial per-pseudo-particle flux payload [89]

$$\Gamma_{\text{part,initial}} = \frac{A_{\text{source}}}{N_{\text{part}}}\Gamma_{\text{source}}\,. \quad (2.15)$$

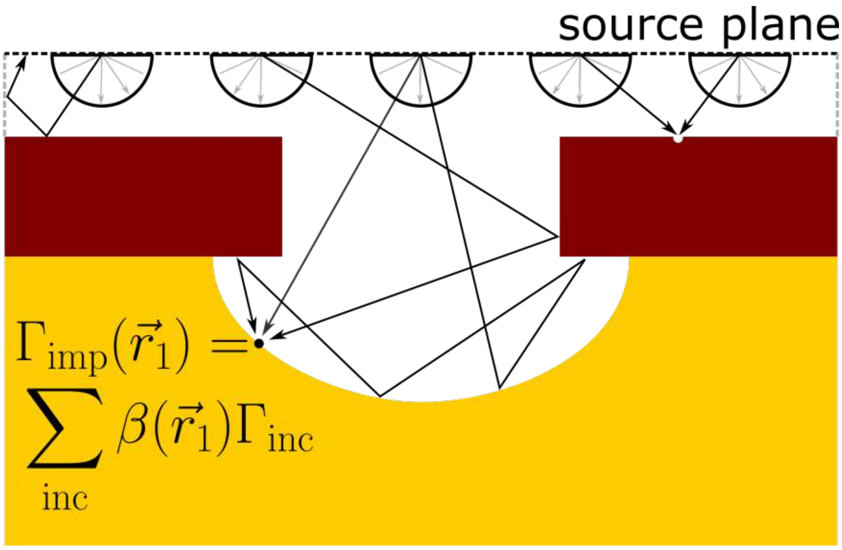

Figure 2.6: Illustration of Monte Carlo tracking of pseudo-particles. They are generated in a top-down fashion from the source plane and carry a flux payload Γ_{inc} which is accumulated at each surface element. Adapted from Aguinsky *et al., Solid State Electron.* 191, (2022) p. 108262. [88], © The Authors, licensed under the CC BY 4.0 License, `https://creativecommons.org/licenses/by/4.0/`.

The pseudo-particles are then initialized with a uniform initial position in the source plane and an initial direction $\vec{t}$ sampled from the $\Gamma_{\text{source}}(\vec{t})$ distribution, e.g., Eq. (2.12) or Eq. (2.13) with $\vec{t} = \vec{r} - \vec{r}\,'$. Each pseudo-particle is traced *top-down* through the simulation domain until it interacts with the geometry and terminates. Then, the pseudo-particle deposits its flux payload mediated by the local value of β [41, 89, 99]. Therefore, each surface element accumulates its impinging flux as the sum over all incident pseudo-particles, each carrying its own payload Γ_{inc}

$$\Gamma_{\text{imp}}(\vec{r}) = \sum_{\text{inc}} \beta(\vec{r})\Gamma_{\text{inc}}\,. \tag{2.16}$$

This formulation enables directly representing the effects of reactant reflections by generating new pseudo-particles according to a reflection distribution. These reflected pseudo-particle have their flux payload Γ_{refl} reduced with respect to the incident pseudo-particle according to

$$\Gamma_{\text{refl}} = (1 - \beta(\vec{r}))\Gamma_{\text{inc}}\,. \tag{2.17}$$

The new pseudo-particles have their initial direction sampled from the hemisphere aligned with the local normal direction. This sampling can take several forms depending on the involved physical and chemical reactions. It is usually assumed that pseudo-particles representing neutral species immediately thermalize and reflect isotropically, sampling the hemisphere with a cosine distribution similar to Eq. (2.12). However, accelerated ions can reflect specularly under certain conditions, thus requiring a distribution function depending on the incoming ray direction $\vec{t}$ [44, 75]. This process of termination and generation repeats until the pseudo-particle leaves the simulation domain or its payload drops below a threshold.

An initial approximation to be made to the top-down approach is assuming constant sticking coefficient, similarly to the discussion in Section 2.3.1 and Section 2.3.2. However, in contrast to the constant flux and bottom-up approaches, β can now take any fixed value between the respective extremes of 0 and 1, including having different values for each involved material. In general, β as described in Eqs. (2.16) and (2.17) is an arbitrary function of the position $\vec{r}$, usually depending on the local surface coverage $\Theta(\vec{r})$ according to Eqs. (2.3) and (2.4) for single-reactant first-order Langmuir kinetics. By assuming a constant and effective value for β, denoted as β_{eff}, it is implicitly assumed that there is also a constant and effective value for Θ (Θ_{eff}) across the geometry, i.e.,

$$\beta_{\text{eff}} = \beta_0 (1 - \Theta_{\text{eff}}) \, . \tag{2.18}$$

Equation (2.18) has two important consequences. Firstly, it provides an upper bound $\beta_{\text{eff}} \leq \beta_0$. Also, it highlights that the constant sticking approximation is better-suited for the low-coverage regime (i.e., the transport-controlled regime), since, in this case, small relative variations $\Delta\Theta_{\text{eff}}/\Theta_{\text{eff}}$ have a lesser impact on the $(1 - \Theta_{\text{eff}})$ term.

The top-down methodology is also suited for more complex reactive transport calculations beyond constant β for a single species. Multiple reactant species, each represented by a different type of pseudo-particle, can be applied to model RIE, including additional pseudo-particle information such as ion energy [44, 43, 78, 99, 100]. The Θ-dependence of β can be calculated, whether by performing a self-consistent calculation of the steady-state Langmuir kinetics [96], or by explicitly solving the time-dependence of Θ [101, 102]. The calculation of the particle trajectory, which is necessary for the ray-tracing algorithms, enables modeling beyond the molecular flow regime. By providing the mean free path λ of the involved reactor conditions, a probability of a scattering event can be calculated from a given trajectory. Therefore, particle-particle collisions and the transitional flow regime can also be modeled with this methodology [103].

One significant challenge of this Monte Carlo approach is the control of convergence. Although it does not require the quadratic computational effort of the direct solution of Eq. (2.14), the number of pseudo-particles necessary might still be substantial. There is no guaranteed convergence by analyzing only the N_{part}, since, e.g., a geometry involving a deep trench might require substantial oversampling to achieve adequate results. Additionally, the inherently random nature of the Monte Carlo process might lead to the introduction of numerical noise to the geometry which might cause problems in further analysis steps. It is important to note that such noise is only numerical and not related to the physically discrete nature of the involved reactants. That is, the pseudo-particles are to be interpreted strictly as a means of sampling an integral equation such as Eq. (2.14) and not as a representation of individual molecules or ions.

2.3.4 One-Dimensional Models

The flux calculation approaches hitherto discussed can be computationally challenging for arbitrary three-dimensional (3D) geometries, even with relatively simple surface kinetics such as the constant β approximation. However, in many situations encountered in semiconductor fabrication, symmetry considerations and approximations can be made to reduce the dimensionality of the problem from 3D to 1D, particularly for structures involving high aspect ratios (ARs) and a preferential transport direction. The AR is defined as the ratio between two critical dimensions (CDs): Depth L to width d (c.f. Fig. 2.7)

$$\mathrm{AR} = \frac{L}{d}\,. \tag{2.19}$$

For example, trenches and vias necessary for innovative back end of line (BEOL) processing [104] as well as modern 3D NAND memories [105] require increasingly higher ARs. Although such structures can have intricate shapes, it is often more useful to focus on phenomena due to the high AR itself. Thus, the complex structure under investigation is replaced by a simpler equivalent geometry with well-defined CDs, as illustrated in Fig. 2.7. Therefore, 1D models with faster performance and additional physical insight can be constructed.

The key approximation behind all 1D models is the assumption that all reactants have an isotropic source distribution and also reflect isotropically (e.g., Eq. (2.12)). This greatly simplifies Eq. (2.14) which takes the form of an integral equation over the whole structure area A' [106]

$$\Gamma_{\text{imp}}(\vec{r}) = \Gamma_{\text{vis}}(\vec{r}) + \int_{A'} (1-\beta(\vec{r}\,'))\Gamma_{\text{imp}}(\vec{r}\,') \frac{\langle(\vec{r}-\vec{r}\,'),\vec{n}\,'\rangle\langle(\vec{r}\,'-\vec{r}),\vec{n}\rangle}{\pi||\vec{r}-\vec{r}\,'||^4} dA' \tag{2.20}$$

and is named the *radiosity equation*, highlighting that the problem is entirely analogous to diffuse radiative heat transfer [98]. This equation can be directly solved using finite elements for arbitrary geometries at great computational cost [97]. However, the problem can be simplified by identifying the *view factor* in Eq. (2.20), which is the fraction of energy $dF_{dA'-dA}$ leaving one differential surface dA' and arriving in dA separated by a distance t, as follows [98]

$$dF_{dA'-dA} = \frac{\langle(\vec{r}-\vec{r}\,'),\vec{n}\,'\rangle\langle(\vec{r}\,'-\vec{r}),\vec{n}\rangle}{\pi||\vec{r}-\vec{r}\,'||^4} dA' = \frac{\cos\theta\cos\theta'}{\pi t^2} dA'\,. \tag{2.21}$$

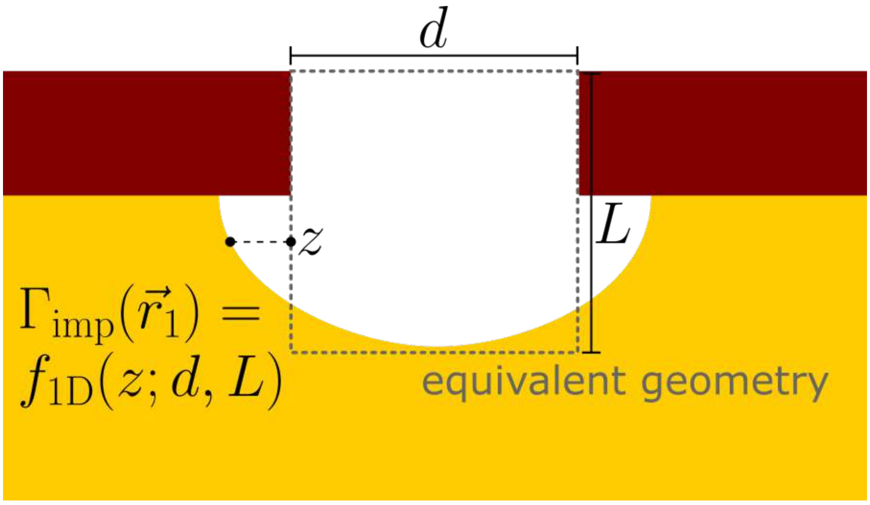

Figure 2.7: Illustration of flux calculation approach using 1D models. The complex 3D structure is mapped to an equivalent geometry with well-defined CDs d and L so that a 1D flux function can be constructed. Adapted from Aguinsky *et al.*, *Solid State Electron.* 191, (2022) p. 108262. [88], © The Authors, licensed under the CC BY 4.0 License, `https://creativecommons.org/licenses/by/4.0/`.

In Eq. (2.21), θ are the angles between each surface normal and the line connecting the surface elements. Thus, pre-calculated tables of view factors [107] can be used to map common high AR structures to 1D line equations over the preferential transport direction z. This enabled Manstetten *et al.* to construct an 1D framework which calculates the flux for several convex high AR structures under the constant β approximation [108]. Kokkoris *et al.* created similar equations for long cylindrical holes and trenches, while also enabling locally-varying $\beta(\vec{r})$ though a self-consistent calculation [106].

These 1D radiosity approaches are valuable due to their computational efficiency. However, they still require a costly matrix inversion step for the calculation of the local fluxes which might be performed several times in the self-consistent calculation for varying $\beta(\vec{r})$. Additionally, these approaches do not enable an intuitive understanding of the effects of the reactive transport parameters without performing the simulations. This motivates another type of 1D model where, instead of directly calculating the integral equation, the reactive transport process is approximated with an 1D diffusion equation [30]. This diffusive transport approach is, however, not only based on conventional molecule-molecule (Fickian) diffusion. Instead, the main drivers of the diffusive process are the molecule-geometry interactions in a process called Knudsen diffusion, which is explored in detail in Chapter 3, including an approach to model the transitional flow regime.

Chapter 3

Knudsen Diffusive Transport

Recently, increased research attention has been placed on the development of one-dimensional (1D) diffusion-based reactive transport models due to their applicability in atomic layer deposition (ALD) [109, 110, 111], following their introduction to aid the design of chemical vapor deposition (CVD) reactors in 1999 [50]. These models have as advantages their relatively straightforward implementation and the ability to provide physically meaningful insight. These diffusive transport approaches are based on *Knudsen diffusion*, that is, the diffusivity stems from molecule-geometry collisions instead of the conventional molecule-molecule interactions. Since its inception in the early 20th century by Martin Knudsen [72], the development of the theory of Knudsen diffusion has been littered with misconceptions [112], requiring corrections calculated by Smoluchowski [113] and Clausing [114, 115]. Nonetheless, many of these misconceptions persist to this day, possibly due to the well-established status of the theory which is often applied without critical examination.

This chapter presents a more rigorous discussion of Knudsen diffusive processes based on the excellent but often-overlooked work by Pollard and Present [116, 117]. First, some properties of ideal gases, stemming from the kinetic theory of gases, are reviewed. Then, the equations of Knudsen diffusion are reformulated in a more modern manner, including their analogy to radiative heat transfer and the role of the *view factor*. The classical result of the diffusivity coefficient in long cylinders is recovered, while problems originating from attempting to derive the commonly-used hydraulic diameter approximation for rectangular trenches [109, 110] are discussed. An approach to capture the transitional flow for intermediate Knudsen numbers, the Bosanquet approximation, is also reviewed. Finally, the original research contributions of this dissertation are presented.

Own contributions: A novel extension to Knudsen diffusion, including the role of the direct flux, is derived, following the work presented at the IWCN 2019 [118] and ALE 2019 [119] conferences. Additionally, two unpublished applications of Knudsen diffusion to problems in semiconductor processing are discussed: Aspect ratio (AR) dependent reactive ion etching (RIE) in the neutral-limited regime and heteroepitaxial growth of 3C-SiC on Si micro-pillars.

3.1 Properties of Ideal Gases

In this section, the properties of ideal gases, that is, the fundamental results of the kinetic theory of gases, are shortly reviewed. They are the foundation of diffusive transport processes and must be carefully considered for a thorough discussion of reactive transport. All definitions follow Present [117], including the necessary adaptations in the labeling of variables for consistency.

Ideal gases, also named perfect gases, are a useful abstraction of real gas behavior under reasonable hypotheses. It is assumed that the gas is composed of molecules, defined as the smallest discrete quantity of a certain substance with defined chemical properties. This definition of molecule encompasses monoatomic gases (e.g., noble gases) and is used instead of "particle" throughout this chapter for consistency with the literature. The number of molecules must be large enough such that meaningful statistical information can be extracted from their average properties. These molecules are assumed to be separated from each other by a distance much greater than its molecular diameter, and they propagate on a straight line throughout a container with fixed volume. Upon colliding with each other or with the walls of the container, the molecules scatter perfectly elastically.

In essence, the assumptions of the kinetic theory of gases hold for systems with low density and without particle acceleration due to, e.g., plasma sheath acceleration. Therefore, in the context of semiconductor processing the ideal gas approximation is well-suited for systems involving gas-phase neutral particles in a vacuum chamber, such as low pressure CVD or ALD. In such situations, the ideal gas law can be derived:

$$p = nk_BT \,, \tag{3.1}$$

where p represents the pressure, n the number density or concentration of molecules, T the temperature, and k_B Boltzmann constant.

Due to the large number of involved molecules, the properties of an ideal gas system can be more precisely studied by analyzing their statistical behavior. The most crucial statistical property of a gas is the distribution function of molecular velocities $f^*(\vec{v})$. If the container carrying the ideal gas is stationary, then trivially all components of the velocity are zero on average, i.e., $\bar{v}_x = \bar{v}_y = \bar{v}_z = 0$. Thus, it is often more useful to focus on the distribution function of the molecular *speed* v which can be obtained by integrating $f^*(\vec{v})$ over the solid angle Ω:

$$f(v) = \int_0^{4\pi} f^*(\vec{v}) d\Omega \tag{3.2}$$

It can be shown that, assuming that the velocities are isotropic and the velocity component in any direction is independent of any other direction, the speed distribution function of an ideal gas composed of molecules of mass m takes the form of

$$f(v) = \left(\frac{m}{2\pi k_BT}\right)^{\frac{3}{2}} e^{-\frac{mv^2}{2k_BT}} \,. \tag{3.3}$$

Equation (3.3) is the *Maxwell-Boltzmann distribution*. The fundamental statistical property extracted from Eq. (3.2) is the average speed $\bar{v}$, also called *thermal speed*:

$$\bar{v} = \int_0^\infty v f(v) dv = \left(\frac{8k_B T}{\pi m}\right)^{\frac{1}{2}} \tag{3.4}$$

Two additional speeds can be computed from the distribution, notably the root-mean squared velocity v_{rms} and the most probable speed v_m. Their values differ from $\bar{v}$ only by fixed constants.

As discussed in Chapter 2, the reactive transport models are intrinsically tied to the local impinging flux Γ_{imp} at the container wall. The Γ_{imp} can be directly calculated for ideal gases by considering its definition: The number of striking molecules per unit area per time. This is shown in Fig. 3.1 for an area dA of the container wall, aligned with the xy-plane without loss of generality. The number of molecules dN which strike dA during a time interval dt with velocities in the neighborhood of $\vec{v}$ are contained in the oblique cylinder with base dA and height $v_z dt$. Therefore, dN can be calculated as the product of the number of molecules per unit volume $nf^*(\vec{v})dvd\Omega$ with the cylinder volume $v_z dt dA$. The differential flux then reads

$$d\Gamma_{\mathrm{imp}} = \frac{dN}{dAdt} = nv_z f^*(\vec{v})dvd\Omega = nvf(v)\cos\theta\, dv \sin\theta\, \frac{d\theta d\phi}{4\pi}\,. \tag{3.5}$$

The impinging flux is then obtained after integrating over all possible values and directions of $\vec{v}$, i.e., over the hemisphere above xy $(0 < \theta < \pi/2)$, obtaining

$$\Gamma_{\mathrm{imp}} = \frac{1}{4\pi}\int_0^\infty vf(v)dv \int_0^{2\pi}\int_0^{\frac{\pi}{2}} \cos\theta \sin\theta\, d\theta\, d\phi = \frac{1}{4}n\bar{v}\,. \tag{3.6}$$

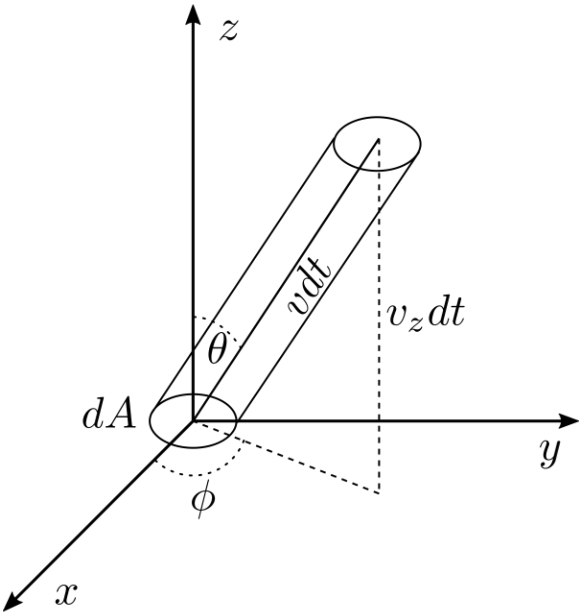

Figure 3.1: Illustration of the oblique cylinder containing the molecules striking area dA of the container wall during time dt. After integration over all velocities in the hemisphere aligned with $+z$, the Hertz-Knudsen equation is obtained.

By using Eqs. (3.1) and (3.4), the impinging flux can be summarized as

$$\Gamma_{\text{imp}} = \frac{1}{4} n\bar{v} = \frac{p}{\sqrt{2\pi m k_B T}} \,. \tag{3.7}$$

The relationship in Eq. (3.7) between the gas properties and the local flux is a fundamental result of surface science and is named the *Hertz-Knudsen equation*.

Additionally, the kinetic theory of gases enables a direct calculation of the mean free path λ of an ideal gas. Assuming that a gas is composed of spherical molecules with a fixed diameter d, the average distance between collisions for a single gas molecules can be calculated as

$$\lambda = \frac{1}{\sqrt{2} n \pi d^2} = \frac{k_B T}{\sqrt{2} \pi d^2} \,. \tag{3.8}$$

The assumption of fixed d is called the "billiard ball" or hard-sphere approximation. Although in reality the physical diameter of molecules is not clearly defined due to their inherent quantum chemical nature, the hard-sphere diameter is defined empirically from measurements of viscosity [120]. Notably, the calculation of Γ_{imp} can be performed assuming a finite λ, that is, that the molecules might collide with each other before impacting the wall. This calculation yields the same result as in Eq. (3.6), further strengthening the Hertz-Knudsen equation.

Finally, the first indications of diffusive transport behavior can be directly encountered by assuming that the concentration n is not constant, but instead it follows a gradient in the z direction. In this situation, n can be approximated via a first-order Taylor expansion at an arbitrary $z = 0$ plane:

$$n(z) = n(0) + z \left.\frac{dn}{dz}\right|_{z=0} \tag{3.9}$$

A similar calculation to that shown in Fig. 3.1 can be performed at the $z = 0$ plane which is not part of the container wall. However, unlike Eq. (3.6), the calculation cannot be restricted to the hemisphere aligned with $+z$. Instead, the net flux crossing the plane $\Gamma_{\text{cross}}(z{=}0)$ is the difference between the flux coming from the hemisphere below Γ_{z^-} and the hemisphere above Γ_{z^+}. The sign convention is that a positive Γ_{cross} is interpreted as a net flow in the $+z$ direction. After performing the involved integral, it can be shown that:

$$\Gamma_{\text{cross}}(z = 0) = \Gamma_{z^-} - \Gamma_{z^+} = -\frac{1}{3} \bar{v} \lambda \frac{dn}{dz} \tag{3.10}$$

Equation (3.10) has the shape of a diffusion equation with diffusivity

$$D_{\text{self}} = \frac{1}{3} \bar{v} \lambda \,. \tag{3.11}$$

These equations represent the phenomenon of *self-diffusion*, that is, the diffusion of one gas through another with the same properties. For example, this is the expected behavior of the diffusion of isotopic tracer molecules through an inert gas composed of molecules with similar weights and diameters.

3.2 Knudsen Diffusion

The transport properties of ideal gases discussed in Section 3.1 are mostly due to the presence of molecule-molecule interactions which are described by the mean free path λ. In the context of semiconductor processing, it is often more important to focus on the interactions of a molecule with the geometry, particularly when the high Knudsen number (Kn) regime is involved. Notwithstanding, the kinetic theory of gases still provides useful insights into this regime, since it can be applied to construct a diffusion-type equation where the transport is driven by molecule-geometry interactions. This phenomenon is called *Knudsen diffusion* [112] in honor of its original proponent [72]. Although Knudsen did indeed obtain the correct expression for the diffusivity for long cylinders, it was later shown by Smoluchowski [113] that his results were incorrect for arbitrary cross-sections. Later, Clausing [114, 115] extended the approach to model tubes of arbitrary length, and Pollard and Present [116] rigorously re-introduced the effects of self-diffusion within Knudsen diffusion.

This section focuses on re-evaluating some of these classical results using a modern formulation, inspired by the derivation by Present [117] and including an analogy with the radiosity method through the view factor. Ultimately, the goal is to apply insights from the kinetic theory of gases and develop approximate one-dimensional models for reactant transport in semiconductor processing, as discussed in Section 2.3.4. It is thus necessary to be careful with all involved approximations so that the resulting models are physically meaningful.

Firstly, the fundamental approximation of Knudsen diffusivity processes is the presence of a preferential transport direction denoted as z. Thus, the impinging flux on all surfaces on any plane of constant $z = z_0$ is the same. Additionally, as is the case with radiosity models, a cosine re-emission distribution is assumed which is a well-established result for uncharged molecules [73]. The molecular flow regime is assumed ($\mathrm{Kn} >> 1$), although Section 3.4 discusses approaches to recover the transitional flow regime. The features are assumed to have high ARs in z, so that the visibility effects due to the direct flux Γ_{vis} are negligible. Finally, the molecule-surface interaction is assumed to follow Langmuir kinetics, as discussed in Section 2.2, however, the involved sticking coefficients are assumed to be low ($\beta << 1$). Therefore, Knudsen diffusive approaches are well-suited for semiconductor processing of high AR features in the high vacuum regime for reactant chemistries involving low β, such as low pressure CVD [50] and ALD [109, 110, 111].

Similarly to the calculation of self-diffusion in Eq. (3.10), the main idea behind Knudsen diffusion is the calculation of the net flux $\Gamma_{\mathrm{cross}}(z)$ through a cross-section of a long (in z) feature with area $A_{\mathrm{cross}}(z)$, as illustrated in Fig. 3.2. The same sign convention of positive sign for a net flux in the $+z$ direction is applied, thus the $\Gamma_{\mathrm{cross}}(z)$ is the difference between the number of molecules per time unit N^- crossing $A_{\mathrm{cross}}(z)$ from $z' < z$ to the number of molecules N^+ crossing from $z' > z$:

$$\Gamma_{\mathrm{cross}}(z) = \frac{N^- - N^+}{A_{\mathrm{cross}}(z)} \tag{3.12}$$

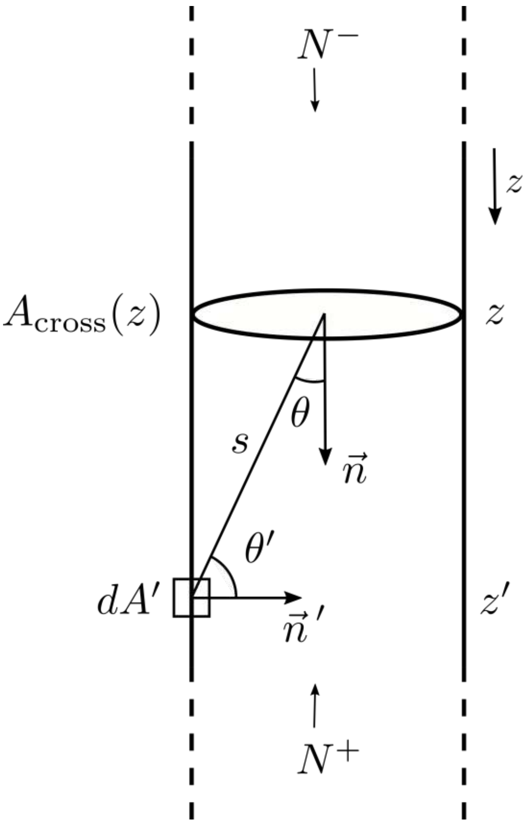

Figure 3.2: Calculation of Knudsen diffusion through a long feature. The net flux through the cross-section $\Gamma_{\text{cross}}(z)$ is the difference between the number of molecules per time unit N^- coming from surface elements dA' with coordinates $z' < z$ to those N^+ coming from $z' > z$ divided by the cross-sectional area $A_{\text{cross}}(z)$.

There are two key insights behind Knudsen diffusion. First, from the molecular flow hypothesis, it is assumed that the molecules crossing $A_{\text{cross}}(z)$ have as origin points *reflections through the geometry*. Therefore, the number of molecules dN^+ coming from a surface element dA' and arriving at the cross-section at a distance s can be written as

$$dN^+ = (1 - \beta(z'))\Gamma_{\text{imp}}(z') \int_{A_{\text{cross}}} \frac{\cos\theta' \cos\theta}{\pi s^2} \, dA \, dA' \,, \tag{3.13}$$

where θ represents the angles between t and the surface normals. Equation (3.13) is analogous to the radiosity formulation of Eq. (2.20) without direct visibility contributions. However, instead of accumulating the flux at each surface element, it is *calculated at the cross-section*, which is not a part of the surface. By using the approximation $\beta << 1$, the Hertz-Knudsen equation from Eq. (3.7), and the definition of the differential-finite view factor [98] as

$$F_{dA'-A} = \int_{A_{\text{cross}}} \frac{\cos\theta' \cos\theta}{\pi s^2} \, dA \,, \tag{3.14}$$

then the number of incoming molecules can be written as

$$N^+ = \frac{1}{4}\bar{v}\int_z^\infty n(z')F_{dA'-A}(z'-z)dA' \,. \tag{3.15}$$

It is important to note that the Hertz-Knudsen equation only states a linear relationship between the concentration and the impinging flux on the surface. It is not valid for Γ_{cross}, since by definition it is a *net flux* and not an impinging flux on the container wall. The formulation in Eq. (3.15) is useful since it enables the use of standard, pre-calculated tables where the view factors are written as a function of $z' - z$ for several geometries [107]. Attention must be placed on the correct use of the chain rule to transform the integration variable from dA' to dz' when considering any particular geometry.

To this point, the derivation has not veered far from the radiosity approach. This leads to the second key insight: To avoid the occurrence of an integral equation in n alike that in Γ_{imp} in Eq. (2.20), the concentration is approximated via a Taylor expansion around z, similarly to Eq. (3.9):

$$n(z') = n(z) + (z'-z)\frac{dn}{dz} + (z'-z)^2\frac{d^2n}{dz^2} + ... \tag{3.16}$$

Thus, after performing the change of variables $z' - z \to z'$, Eq. (3.15) reads:

$$N^+ = \frac{1}{4}\bar{v}n(z)\int_0^\infty F_{dA'-A}(z')dA' + \frac{1}{4}\bar{v}\frac{dn}{dz}\int_0^\infty z'F_{dA'-A}(z')dA' + ... \tag{3.17}$$

By analogy, the equation for N^- reads:

$$N^- = \frac{1}{4}\bar{v}n(z)\int_{-\infty}^0 F_{dA'-A}(z')dA' + \frac{1}{4}\bar{v}\frac{dn}{dz}\int_{-\infty}^0 z'F_{dA'-A}(z')dA' + ... \tag{3.18}$$

Most view factor tables implicitly assume a strictly positive axial distance z'. However, from the interpretation of the view factor as the mutual visibility between two surfaces, it is clear that it must be symmetric in z', so the property

$$F_{dA'-A}(z') = F_{dA'-A}(-z') \tag{3.19}$$

must hold. This can be imposed without loss of generality by imposing the absolute value function over the odd exponents of z' on the expressions from the view factor tables [107]. Therefore, Eq. (3.18) can be simplified by reversing the integration bounds and by changing the sign of the integration variable $z' \to -z'$:

$$\begin{aligned} N^- = \frac{1}{4}\bar{v}n(z)\int_0^\infty F_{dA'-A}(-z')dA' + \frac{1}{4}\bar{v}\frac{dn}{dz}\int_0^\infty (-z')F_{dA'-A}(-z')dA' + ... = \\ + \frac{1}{4}\bar{v}n(z)\int_0^\infty F_{dA'-A}(z')dA' - \frac{1}{4}\bar{v}\frac{dn}{dz}\int_0^\infty z'F_{dA'-A}(z')dA' + ... \end{aligned} \tag{3.20}$$

When combining the results of Eqs. (3.17) and (3.20) into Eq. (3.12), all terms containing the even-order terms of the Taylor expansion (n, d^2n/dz^2, ...) cancel out.

Thus, after truncating the expansion on the first-order term, the following diffusion equation is obtained

$$\Gamma_{\text{cross}}(z) = -D_{\text{Kn}}(z)\frac{dn}{dz}\,, \tag{3.21}$$

where the Knudsen diffusivity $D_{\text{Kn}}(z)$ for a long feature is

$$D_{\text{Kn}}(z) = \frac{\bar{v}}{2A_{\text{cross}}(z)}\int_0^\infty z' F_{dA'-A}(z')dA'\,. \tag{3.22}$$

Although Eq. (3.22) still requires the calculation of an integral, it does not depend on n. Therefore, it is not an integral equation. Save for the dependence on $\bar{v}$ which can be straightforwardly calculated using Eq. (3.4), D_{Kn} is a strictly geometric property similar to the W transmission quantity proposed by Clausing [114, 115]. As an example, the classical result of Knudsen diffusion in a long cylinder can be recovered by considering the geometry represented in Fig. 3.3.

Figure 3.3 shows the coordinate system for the calculation of the view factor inside a long cylinder between a lateral area element and a circular disk at the base, separated by the axial distance z'. From the cylinder geometry, it is evident that $A_{\text{cross}} = \pi d^2/4$ and $dA' = \pi d\,dz'$. The view factor in this configuration has been calculated [107, 121, 122] and takes the form

$$F_{dA'-A}(z') = \frac{\left(\frac{z'}{d}\right)^2 + \frac{1}{2}}{\sqrt{\left(\frac{z'}{d}\right)^2 + 1}} - \left|\frac{z'}{d}\right|\,. \tag{3.23}$$

After replacing these terms in Eq. (3.22) and performing the integration, the standard result for the diffusivity is recovered:

$$D_{\text{Kn}} = \frac{1}{3}\bar{v}d \tag{3.24}$$

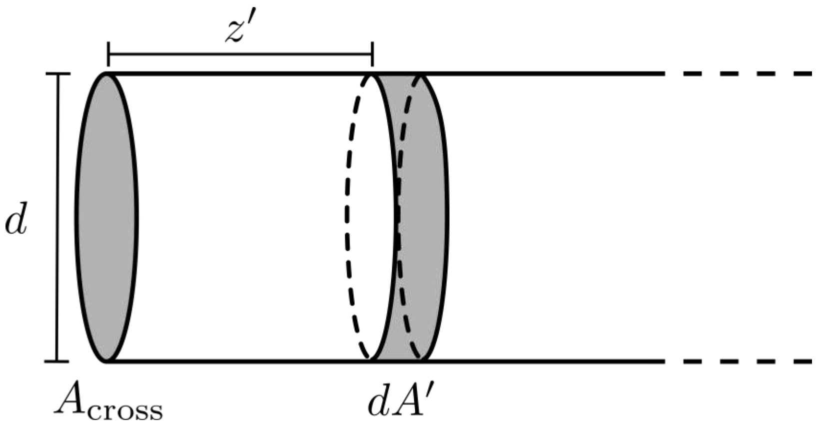

Figure 3.3: View factor calculation inside a long cylinder with diameter d. The cylindrical element dA' is separated by z' from a circular disk of area A_{cross} at the end of a long cylinder.

Equation (3.24) is remarkable for its clear analogy with the self-diffusion coefficient from Eq. (3.11). From an intuitive perspective, it appears as if Knudsen diffusion simply corresponds to self-diffusion after replacing the mean free path λ by a characteristic geometric length d. However, Section 3.3 discusses issues which arise if this analogy is fully assumed at face value without a more careful consideration of the geometry.

To correctly model the reactive transport inside the feature, Eq. (3.21) is not sufficient. The intent behind the original development of the theory was to capture the flow between two reservoirs of constant pressure connected by a tube [112]. No attention is placed on the state of the surface inside this tube, particularly since the approximation of very low β is imposed. However, for semiconductor processing applications, the goal is to achieve an accurate description of the surface through which Knudsen transport takes place. Accordingly, a surface advection velocity function can be constructed from surface-chemical information. A fuller description of the chemical phenomena is achieved by imposing conservation of mass in the presence adsorption losses at the sidewalls [50, 123]:

$$\frac{\partial n(z,t)}{\partial t} + \frac{\partial \Gamma_{\text{cross}}(z,t)}{\partial z} = -\bar{s}\beta(z)\Gamma_{\text{imp}}(z) \tag{3.25}$$

From the discussion in Section 2.2, it is usually assumed that transport equilibrates much more quickly than the surface kinetics. This is also named the frozen surface approximation [124], and it means that the first term in Eq. (3.25) is zero (i.e., a steady-state condition in n), even if the surface kinetics have not equilibrated ($d\Theta/dt \neq 0$). This steady-state conservation of mass is illustrated in Fig. 3.4. The right-hand side of Eq. (3.25) represents the volumetric losses due to adsorption, where $\bar{s}$ is the specific surface area, i.e., the surface area per unit volume. For a cylinder, $\bar{s} = 4/d$.

After replacing the previously calculated results for a cylinder and the Hertz-Knudsen Eq. (3.7) into Eq. (3.25), the following ordinary differential equation (ODE) is obtained:

$$-D_{\text{kn}}\frac{d^2n}{dz^2} = -\bar{s}\beta(z)\Gamma_{\text{imp}}(z) \implies \frac{1}{3}\bar{v}d\frac{d^2n}{dz^2} = \frac{4}{d}\beta(z)\frac{1}{4}\bar{v}n(z) \tag{3.26}$$

This equation can be further simplified by assuming constant β and by performing the change of variables $z \to \varepsilon L$, with L being the length of the cylinder. Then,

$$\frac{d^2n}{d\varepsilon^2} = 3\beta\frac{L^2}{d^2}n(\varepsilon) = h_T^2\, n(\varepsilon)\,, \tag{3.27}$$

where h_T^2 is the Thiele modulus, also called the second Damköhler number [50, 124], which is the ratio of the reaction rate to the transport rate. By identifying the AR from Eq. (2.19), h_T^2 takes the form

$$h_T^2 = 3\beta(\text{AR})^2\,. \tag{3.28}$$

For many semiconductor processing techniques, the goal is to achieve conformality, that is, a uniform distribution of growth or etch rates throughout the geometry.

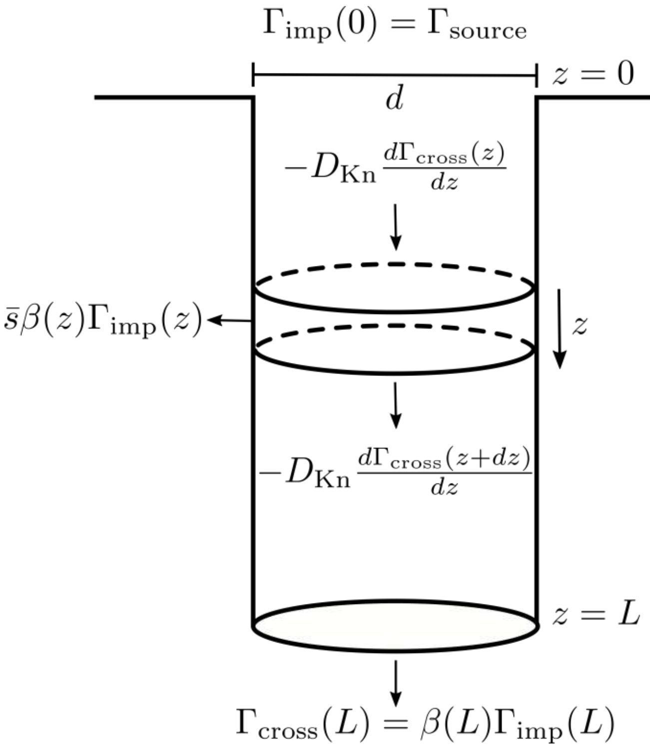

Figure 3.4: Illustration of steady-state conservation of mass in a cylinder leading to a 1D diffusion equation including the two required boundary conditions.

From Eq. (3.27), this means having a value $h_T^2 << 1$. A dimensionality analysis in Eq. (3.28) exposes the challenge of achieving good conformality in high AR structures. There is a quadratic dependence on the AR which can only be combatted with linear improvements in β. The issue of non-ideal conformality in atomic layer processing (ALP) is the subject of Chapter 4.

Equation (3.26) is an ODE of the second degree. Therefore, it requires two boundary conditions (BCs). First, as discussed in Section 2.3, it is always assumed that there is a constant distribution of reactants in the region of the reactor neighboring the feature, i.e., the source plane, which for a long feature is defined as the plane z=0 at the top. This means that the reactor is efficient enough to maintain a constant impinging flux $\Gamma_{\text{imp}}(z{=}0){=}\Gamma_{\text{source}}$. In the context of the Hertz-Knudsen equation, this is equivalent to maintaining a constant concentration (n_0) at the top:

$$n(0) = n_0 \tag{3.29}$$

The second BC is defined at the bottom (z=L). This BC must also have a different treatment than in the classical case of a tube connecting two reservoirs with fixed pressures. This situation would yield a BC similar to Eq. (3.29). Instead, the BC at z=L is that the flux must match the losses due to adsorption, thus preserving the mass balance. This is achieved through a Robin BC which takes the form [30]:

$$\Gamma_{\text{cross}}(L) = \beta(L)\Gamma_{\text{imp}}(L) \implies -D_{\text{Kn}} \left.\frac{dn}{dz}\right|_{z=L} = \beta(L)\frac{1}{4}\bar{v}n(L) \tag{3.30}$$

Under the approximation of constant β and the aforementioned BCs, the ODE from Eq. (3.26) has an exact solution [50] which can be written in terms of the normalized flux normalization $\hat{\Gamma}_{\mathrm{imp}}(z)$ following the convention from Eq. (2.7):

$$\hat{\Gamma}_{\mathrm{imp}}(z) = \frac{\Gamma_{\mathrm{imp}}(z)}{\Gamma_{\mathrm{source}}} = \frac{n(z)}{n_0} = \frac{3\sqrt{\beta}\sinh\left(\frac{\sqrt{3\beta}(L-z)}{d}\right) + 4\sqrt{3}\cosh\left(\frac{\sqrt{3\beta}(L-z)}{d}\right)}{3\sqrt{\beta}\sinh\left(\frac{\sqrt{3\beta}L}{d}\right) + 4\sqrt{3}\cosh\left(\frac{\sqrt{3\beta}L}{d}\right)} \tag{3.31}$$

3.3 Approximations for Long Rectangular Trenches

From the beginning of the development of the theory of Knudsen diffusion, there has been controversy about its proper application to tubes with non-cylindrical cross-sections [112]. Smoluchowski [113] provided a correction to the calculation method originally proposed by Knudsen [72] which eventually led to the development of tables of transmission probabilities W for rectangular tubes of different widths w to heights h [112]. These tubes are defined by the structural ratio

$$X = \frac{w}{h} \tag{3.32}$$

which is, in essence, the AR in the plane perpendicular to the preferential transport direction. However, the nomenclature X is preferred since AR is conventionally reserved for relating to the *depth* of the feature (c.f. Fig. 2.7).

As the semiconductor processing community started applying Knudsen diffusion models to deposition processes in rectangular trenches, simplified expressions were sought [50]. In general, these models attempt to use the results obtained for a long cylinder, discussed in Section 3.2, but assuming an equivalent diameter d_{equiv}. This is conventionally performed in analogy to continuum fluid dynamics through the use of the hydraulic diameter approximation [109]:

$$d_{\mathrm{equiv}} = \frac{2}{\frac{1}{w} + \frac{1}{h}} = h\, g_{\mathrm{hd}}(X) \tag{3.33}$$

That is, the equivalent diameter is found by identifying a characteristic length (h) and multiplying it by a *geometric factor* determined solely by the structural ratio X:

$$g_{\mathrm{hd}}(X) = \frac{2}{1 + \frac{1}{X}} \tag{3.34}$$

Equation (3.34) claims that a square hole ($X{=}1$) is equivalent to the inscribed cylinder ($d{=}h$), and that an infinitely wide trench has an equivalent diameter twice as large as its opening, i.e., $\lim_{X\to\infty} g_{\mathrm{hd}}(X) = 2$.

The approximation in Eq. (3.33) is further justified by Monte Carlo simulations for square holes [125]. This eventually led to Cremers *et al.* proposing a mapping between several three-dimensional (3D) structures to equivalent cylinders through a purportedly structure-independent parameter: The equivalent aspect ratio (EAR) [110].

That is, all studies of conformality in different structures, such as square holes or wide trenches, can be related to an equivalent cylinder with AR as conventionally defined in Eq. (2.19). They propose, among others

$$\mathrm{EAR}(\text{square hole}) = \frac{L}{h} = \frac{L}{h\, g_{\mathrm{hd}}(1)}\,, \tag{3.35}$$

$$\mathrm{EAR}(\text{infinitely wide trench}) = \frac{L}{2h} = \frac{L}{h\, g_{\mathrm{hd}}(\infty)}\,. \tag{3.36}$$

These definitions, however, are still questionable. Already from the work of Smoluchowski [113], it is known that the transport properties in a square hole differ from a cylinder by a fixed factor [112].

A more rigorous definition of the geometric factor $g_{\mathrm{vf}}(X)$ for long square holes can be obtained by using the expression for D_{Kn} involving the view factors. After introducing $A_{\mathrm{cross}}{=}wh$ in Eq. (3.22) and identifying the characteristic length as h:

$$D_{\mathrm{Kn}} = \frac{1}{3}\bar{v}h \cdot \underbrace{\frac{3}{2}\frac{1}{wh^2}\int_0^{\infty} z' F_{dA'-A}(z', X)\, dA'}_{g_{\mathrm{vf}}(X)} \tag{3.37}$$

For clarity, it is useful to calculate the contributions of each individual trench wall separately. This is shown in Fig. 3.5 for the exchange between a surface element dA' on one of the walls with width w to the rectangle at the end of the trench. The view factor has been calculated in terms of $Z = z'/w$ and X and takes the form [107]:

$$F_{dA'-A}(Z, X) =$$
$$\frac{1}{\pi}\left[\arctan\frac{1}{Z} + \frac{Z}{2}\ln\left(\frac{Z^2\left(Z^2+\frac{1}{X^2}+1\right)}{\left(Z^2+1\right)\left(Z^2+\frac{1}{X^2}\right)}\right) - \frac{Z}{\sqrt{Z^2+\frac{1}{X^2}}}\arctan\frac{1}{\sqrt{Z^2+\frac{1}{X^2}}}\right] \tag{3.38}$$

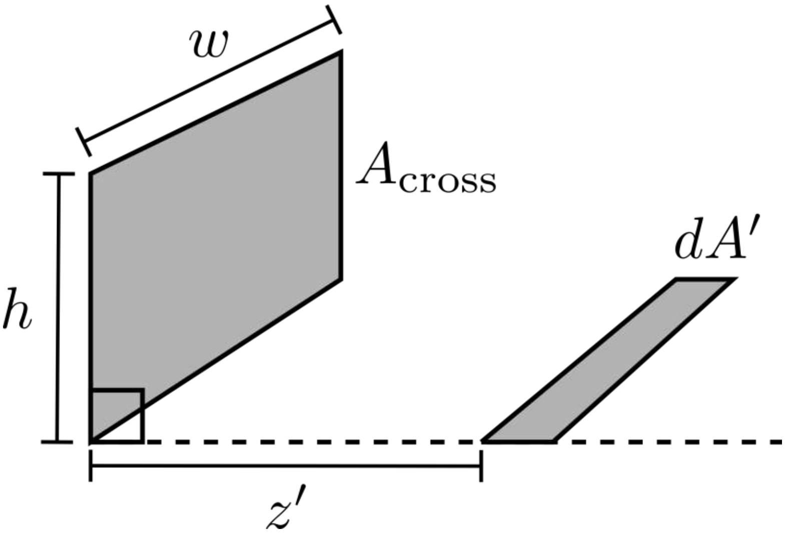

Figure 3.5: View factor calculation for one wall of a long rectangular trench with height h and width w. The rectangular strip dA' on the trench wall is separated by z' from a rectangle of area A_{cross} at the end of the long trench.

The expression for $g_{\text{vf}}(X)$ is then obtained by combining the two contributions from the walls aligned with w with those from the two walls aligned with h. The latter have view factors equivalent to Eq. (3.38) but with the role of w and h reversed, i.e., $X \to 1/X$. After performing the necessary substitutions to obtain integrals over a variable Z:

$$g_{\text{vf}}(X) = 3\left(X^2 \int_0^\infty Z F_{dA'-A}(Z,X)dZ + \frac{1}{X}\int_0^\infty Z F_{dA'-A}(Z,\frac{1}{X})dZ\right) \tag{3.39}$$

The integral resulting from inserting the view factor from Eq. (3.38) into Eq. (3.39) does not have a closed-form solution. Nonetheless, it can be solved numerically with a program such as Mathematica [126]. For the case of a square hole, a value $g_{\text{vf}}(1) \approx 1.11495$ is obtained which is numerically equivalent to the ratio of transmission probabilities $W_{\text{square}}/W_{\text{cylinder}} \approx 1.11495$ calculated using Smoluchowski's expression [112]. Thus, it is clear that the EAR for a square proposed by Eq. (3.35) is incorrect, albeit only by a factor of approximately 10 %.

A larger problem occurs when attempting to recover the wide trench limit. As it can be intuited from the first term on Eq. (3.39), $g_{\text{vf}}(X)$ diverges on the infinite width limit $X \to \infty$. This is represented in Fig. 3.6, where numerical calculations of both forms of the geometric factor, $g_{\text{vf}}(X)$ and $g_{\text{hd}}(X)$, are compared. Figure 3.6 demonstrates that the hydraulic diameter approximation consistently underestimates the more rigorous $g_{\text{vf}}(X)$. Additionally, it indicates that the divergence of $g_{\text{vf}}(X)$ occurs very slowly, as even for rather extreme values of $X > 100$, g_{vf} remains in the same order of magnitude as g_{hd}.

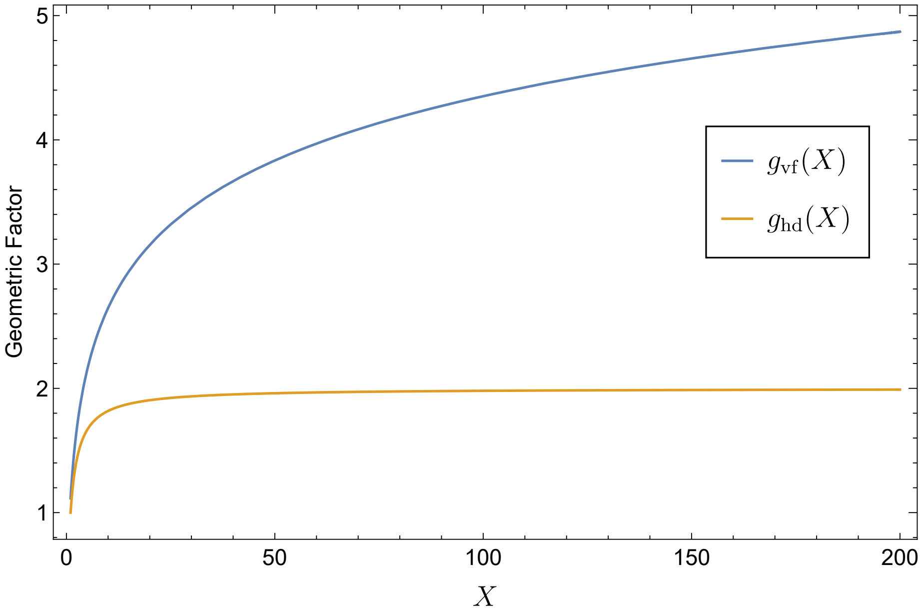

Figure 3.6: Comparison of the geometric factor from the hydraulic diameter approximation $g_{\text{hd}}(X)$ to that from the rigorous view factor $g_{\text{vf}}(X)$ calculation as a function of the rectangular structural ratio X (c.f. Fig. 3.5).

Therefore, it must be concluded that Knudsen diffusion is not strictly defined for very wide trenches. However, in practice it remains a useful model in the limit $w \to \infty$. In this situation, the molecule-molecule collisions, and, therefore, the mean-free path λ, can no longer be neglected. A rough analogy is that, as w increases, X does not increase asymptotically. Instead, it is bounded by λ, that is,

$$\lim_{w \to \infty} X \approx \frac{\lambda}{h} = \mathrm{Kn} \tag{3.40}$$

which can be identified as the definition of the Knudsen number in Eq. (2.6). Thus, assuming a pressure regime resulting in $\mathrm{Kn} \approx 100$, the hydraulic diameter approximation is only wrong by a factor of approximately 2. Since there are large uncertainties in the involved parameters, particularly the sticking coefficient, such a factor can be neglected in many cases. However, unlike the claim in [110], results from different geometries cannot be directly compared without careful consideration.

Finally, it is noteworthy that $g_{\mathrm{vf}}(X)$ only applies to the dependency on d for the calculation on the diffusivity D_{Kn}. The conservation of mass in Eq. (3.25) also involves d in the adsorption loss term in its right-hand side through the specific surface ratio $\bar{s} = 4/d$. For a rectangular trench

$$\bar{s} = \frac{2(h+w)}{hw} = \frac{4}{h\, g_{\mathrm{hd}}(X)} \,. \tag{3.41}$$

Therefore, the hydraulic diameter approximation *must* be applied to the right-hand side of Eq. (3.25). This is likely the source of the lingering confusion, since Eq. (3.41) has been correctly applied since the first applications of Knudsen diffusion in semiconductor processing [50].

3.4 Transitional Flow

The theory of Knudsen diffusion presented so far has focused on the molecular flow regime. However, as it has already been discussed for Eq. (3.40), the presence of molecule-molecule collisions affects the transport properties even for high Kn. These issues become even more salient in the transitional flow regime (approximately $10^{-1} < \mathrm{Kn} < 10$), as the molecule-molecule collisions become roughly as likely as molecule-geometry interactions.

A rigorous examination of the problem of diffusion in long cylindrical tubes was performed by Pollard and Present [116]. They perform an integration procedure similar in concept to that presented in Eq. (3.22), but including an additional integration over the s between the cross-sectional area and the surface element (c.f. Fig. 3.2). This additional integral captures an attenuation of the number of incoming molecules due to molecule-molecule collisions through an $e^{-s/\lambda} ds$ term. They obtain a general expression for the combined diffusion coefficient

$$D_{\mathrm{Kn+self-diffusion}} = \frac{1}{3}\bar{v}\lambda \left[1 - \frac{6}{8}\frac{\lambda}{d} + \frac{12}{\pi}\frac{\lambda}{d} Q(d/\lambda) \right] . \tag{3.42}$$

In Eq. (3.42), $Q(d/L)$ is an integral which must be calculated numerically. $Q(d/L)$ has the key property of recovering both the self-diffusivity from Eq. (3.11) in the limit $\lambda >> d$, as well as the standard Knudsen diffusivity from Eq. (3.24) after calculating the limit $d >> \lambda$.

However, Eq. (3.42) is valid only for the combination of Knudsen with self-diffusion. For the issue of mutual diffusion, that is, the diffusion of two gases of different characteristics, mean free path approximations like Eq. (3.8) fail [117]. To address that issue, the Chapman-Enskog theory of diffusion was developed [120] which has as a fundamental result the following diffusivity D_{AB} between two "billiard ball" molecules A and B

$$D_{AB} = \frac{3}{8}\sqrt{\frac{\pi k_B T}{2m^*}}\frac{1}{n\pi d_{AB}^2}\,, \tag{3.43}$$

with $m^* = m_A m_B/(m_A + m_B)$ being the reduced mass, d_{AB} the average molecular diameter $(d_A + d_B)/2$, and n the total concentration $n_A + n_B$.

In order to capture a combined diffusivity D stemming from an arbitrary gas-phase diffusivity D_{gas} and the Knudsen diffusivity D_{Kn} in a more general manner, Bosanquet proposed an interpolation formula. This work is usually attributed to a British military technical report from 1944 [127], which is not easily available to the public. It was re-introduced to the scientific community at large by Pollard and Present [116]. The Bosanquet formula is not rigorously derived, instead, it is based on the intuition that the combined frequency of the total scattering events (i.e., both molecule-molecule and molecule-geometry collisions) is the sum of the individual frequencies of each type of collision. From that insight, each collision frequency is identified as approximately the inverse of the respective diffusion coefficient. Therefore, Bosanquet interpolation formula for the combined diffusivity D is

$$\frac{1}{D} \approx \frac{1}{D_{\text{gas}}} + \frac{1}{D_{\text{Kn}}}\,. \tag{3.44}$$

Equation (3.44) is an interpolation formula since it naturally recovers the limits $D_{\text{gas}} >> D_{\text{Kn}}$ and vice-versa. Notably, Pollard and Present [116] achieve excellent agreement between their formula in Eq. (3.42) and Eq. (3.44) using the standard self-diffusion and Knudsen diffusivity formulas.

3.5 Extended Knudsen Diffusion

The standard Knudsen diffusion calculation discussed in Section 3.2 requires substantial approximations. Namely, the sticking coefficients are assumed to be low, and the features are assumed to be long, such that the diffusion process can be approximated by the diffusivity of infinite cylinders or trenches. Therefore, local contributions to the flux due to visibility of the source (c.f. Section 2.3.2) are neglected. Although Clausing has calculated corrections in transmission probabilities for short cylinders [114, 115], the issue of direct source flux contributions remains unaddressed.

The hitherto discussed formulation of Knudsen diffusivity including the view factors enables an extended calculation overcoming these limitations for short cylinders and including the direct flux in a straightforward manner. In essence, the mass balance procedure follows the same derivation that Eq. (3.15), however, the preferential transport direction z is no longer assumed to extend from $-\infty$ to ∞. Instead, the same mass balance integrals to calculate Γ_{cross} from Eq. (3.12) are now restricted to the range 0 to L, as illustrated in Fig. 3.7. This restriction now enables considering the contributions due to the direct flux from the source area A_{source}.

In contrast to the bottom-up approach discussed in Section 2.3.2, the direct flux is not computed at each surface element. Instead, it is accumulated at the entire cross-section through the N^- element of the net flux balance in Eq. (3.12). It now reads

$$N^- = \Gamma_{\text{source}} A_{\text{source}} F_{\text{source}-\text{cross}}(0-z) + \int_0^z (1-\beta(z'))\Gamma_{\text{imp}}(z') F_{dA'-A}(z'-z)\,dA' \,. \quad (3.45)$$

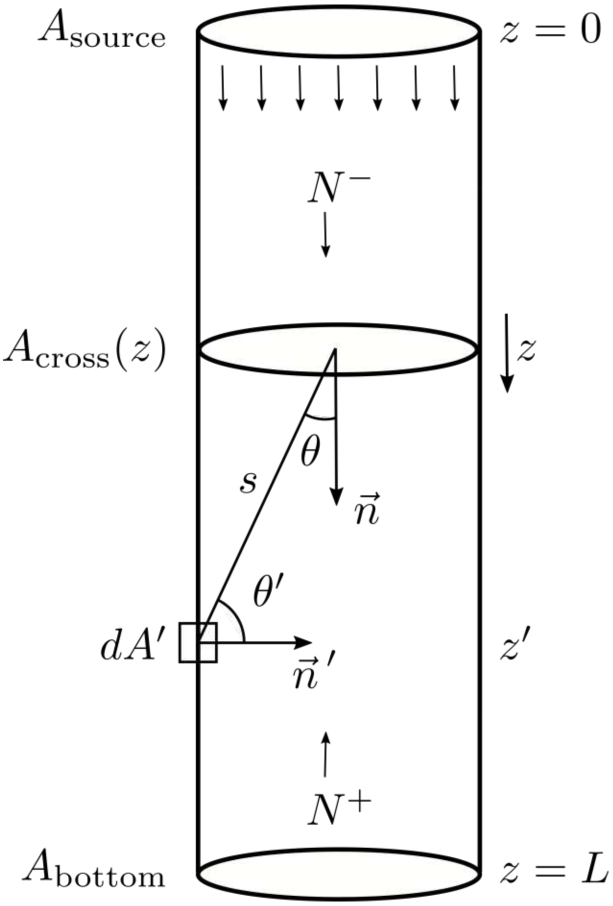

Figure 3.7: Calculation of extended Knudsen diffusion through an arbitrary feature. The geometry is now restricted from z varying between 0 and L and the direct flux contributions from A_{source} are incorporated.

In Eq. (3.45), $F_{\text{source}-\text{cross}}$ is the finite-finite view factor between A_{source} and A_{cross} [98]. This element is not multiplied by a sticking coefficient since it is assumed that the source is fully emitting (i.e., $\beta_{\text{source}} = 0$). Similarly, the N^+ term must consider the flux due to reflections from the bottom area A_{bottom}:

$$N^+ = \\ (1-\beta(L))\Gamma_{\text{imp}}(L)A_{\text{bottom}}F_{\text{bottom}-\text{cross}}(L-z)+\int_z^L(1-\beta(z'))\Gamma_{\text{imp}}(z')F_{dA'-A}(z'-z)dA' \tag{3.46}$$

Just as in Section 3.2, in order to avoid an integral equation, a Taylor expansion of the concentration similar to Eq. (3.16) is required. There are, however, subtle differences. The lack of infinite dimensions means that even-order terms do not cancel from symmetry considerations. Instead, all terms above the first derivative are directly truncated, and the term involving $n(z)$ cannot be disregarded.

For simplicity, similar considerations to those made in Eq. (3.31) are made. First, a constant value of β is assumed. Also, all terms are normalized with respect to Γ_{source}, therefore, the Taylor expansion can be performed over $\hat{\Gamma}_{\text{imp}}(z)$ instead of n, as they are equivalent after normalization (c.f. Eq. (3.7)). Additionally, in a similar vein to Eq. (2.7), a normalized cross-sectional flux is defined as:

$$\hat{\Gamma}_{\text{cross}}(z) = \frac{\Gamma_{\text{cross}}(z)}{\Gamma_{\text{source}}} \tag{3.47}$$

With all these considerations, Eqs. (3.45) and (3.46) are combined with the net flux from Eqs. (3.12) and (3.47) to obtain

$$\begin{aligned}
&\hat{\Gamma}_{\text{cross}}(z) = \\
&\quad \frac{A_{\text{source}}}{A_{\text{cross}}(z)}F_{\text{source}-\text{cross}}(0-z) - (1-\beta)\frac{A_{\text{bottom}}}{A_{\text{cross}}(z)}F_{\text{bottom}-\text{cross}}(L-z)\hat{\Gamma}_{\text{imp}}(z) \\
&\quad + (1-\beta)\frac{1}{A_{\text{cross}}(z)}\left[\int_0^z F_{dA'-A}(z'-z) - \int_z^L F_{dA'-A}(z'-z)dA'\right]\hat{\Gamma}_{\text{imp}}(z) \\
&+(1-\beta)\frac{1}{A_{\text{cross}}(z)}\left[\int_0^z (z'-z)F_{dA'-A}(z'-z) - \int_z^L (z'-z)F_{dA'-A}(z'-z)dA'\right]\frac{d\hat{\Gamma}_{\text{imp}}(z)}{dz} \\
&\quad - (1-\beta)\frac{A_{\text{bottom}}}{A_{\text{cross}}(z)}(L-z)F_{\text{bottom}-\text{cross}}(L-z)\frac{d\hat{\Gamma}_{\text{imp}}(z)}{dz}\,.
\end{aligned} \tag{3.48}$$

Using the same conventions, the steady-state conservation of mass can be written as:

$$\frac{d\hat{\Gamma}_{\text{cross}}}{dz} = -\bar{s}\beta\hat{\Gamma}_{\text{imp}}(z) \tag{3.49}$$

The BCs are then equivalent to those from Eqs. (3.29) and (3.30):

$$\hat{\Gamma}_{\text{imp}}(0) = 1 \tag{3.50}$$

$$\hat{\Gamma}_{\text{cross}}(L) = \beta\hat{\Gamma}_{\text{imp}}(L) \tag{3.51}$$

It is important to note that, instead of a second-order ODE in n, the extended Knudsen diffusion is a system of coupled first-order ODEs for $\hat{\Gamma}_{\text{imp}}$ and $\hat{\Gamma}_{\text{cross}}$. Although it is indeed not an integral equation, it still requires the pre-computation of several integrals which might have fairly complex forms. This, in combination with the complexity of Eq. (3.48), makes the use of numerical methods necessary.

To investigate the consequences of this extended calculation, it is evaluated for a finite cylinder of constant diameter. The same differential-finite view factor from Eq. (3.23) is used, as well as the disk to parallel coaxial disk view factor, necessary for the terms involving both A_{source} and A_{bottom} [107, 128]

$$F_{\text{disk}-\text{disk}} = \frac{1}{2}\left[R - \sqrt{R^2 - 4}\right] , \tag{3.52}$$

where

$$R = \frac{2\frac{d^2}{z'^2} + 4}{\frac{d^2}{z'^2}} , \tag{3.53}$$

such that both disks are separated by z' and have equal diameters d. The resulting ODEs after computing the involved integrals in Eq. (3.48) have a closed-form expression, however, they are omitted for brevity. The numerical solution of the ODE system is computed using Mathematica [126]. It is compared to both the solution of the standard Knudsen diffusion from Eq. (3.31) and that obtained with a radiosity framework [108], shown in Fig. 3.8.

In Fig. 3.8, it can be seen that the extended Knudsen diffusion follows very closely the curve obtained using the radiosity framework. Since the latter evaluates the integral equation and has been validated with a Monte Carlo simulation [108], it can be considered the exact result for a cylinder. For cylinders with low β, all flux calculations yield very similar results which is expected from the characteristics of Knudsen diffusion discussed so far. Interestingly, qualitatively similar results among all calculations are also obtained for the lowest AR cylinder, even though the standard Knudsen diffusion has been constructed for long cylinders. This is evidence that, for relatively short cylinders, the important physical phenomena are captured by the boundary conditions instead of the diffusivity.

In the situation of high AR and high β, standard Knudsen diffusion deviates more notably from both extended Knudsen diffusion and the radiosity framework. This is due to the lack of direct flux in standard Knudsen diffusion, thus the exponential decline of Eq. (3.31) is the only dominating factor. Naturally, in situations of higher β, attention must be placed on the role of the direct flux. A methodology to partially recover the effects of the direct flux while still using the standard Knudsen diffusion is discussed in Section 3.6.2.

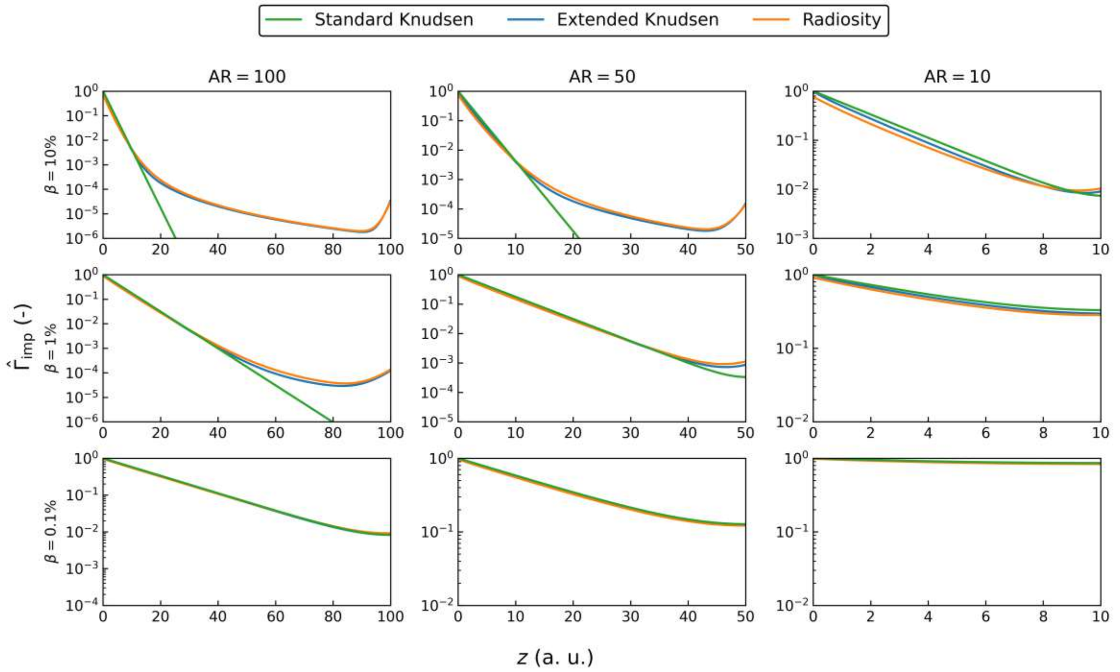

Figure 3.8: Comparison of normalized impinging flux $\hat{\Gamma}_{\text{imp}}$ calculated using extended Knudsen diffusion to that using standard Knudsen and the radiosity framework [108] as a function of the axial distance z in arbitrary units. Calculations were performed for a finite cylinder of diameter $d = 1\,\text{a.u.}$ for multiple values of constant sticking coefficient β and aspect ratio AR.

Nonetheless, the success of the extended Knudsen diffusion should be carefully interpreted. The qualitative agreement shown in Fig. 3.8 is an indication of the small relative error between the extended diffusive calculations and the exact radiosity framework. However, since $\hat{\Gamma}_{\text{imp}}$ is already normalized to Γ_{source}, it is in fact more useful to focus on the *absolute* error in $\hat{\Gamma}_{\text{imp}}$ to obtain the deviation in units of Γ_{source}. This is shown in Fig. 3.9 for the case of a cylinder of $d = 1\,\text{a.u.}$ and $\text{AR} = 100$. There, it can be seen that the error is more pronounced at the top of the cylinder for higher values of β. Such error is likely a consequence of the boundary condition in Eqs. (3.29) and (3.50) imposing maximum flux at the top. For higher values of β, the reduction in flux due to the 90° inclination of the cylinder wall with respect to the source plane is an important factor which is not captured.

Additionally, the difference in absolute error between the standard and extended Knudsen diffusion is minimal. This is more apparent when one of the results from Fig. 3.8 is evaluated without the logarithmic scale. This is shown in Fig. 3.10 for the cylinder with $\text{AR} = 100$ and $\beta = 1\,\%$. In this linear plot, it is clear that all curves are very similar qualitatively. Therefore, the standard Knudsen approach is more than adequate for many applications, as long as the phenomenological parameters are sufficiently adjusted.

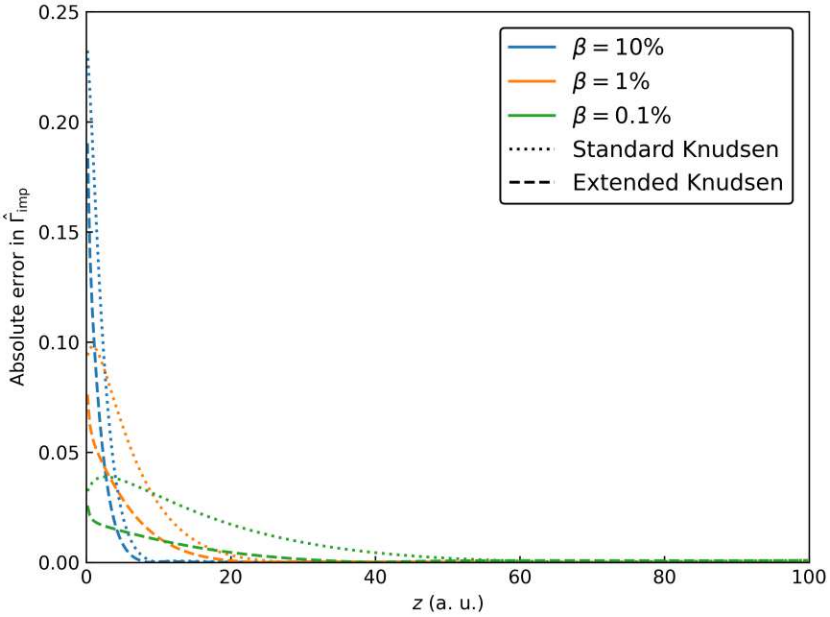

Figure 3.9: Axial length (z) distribution of the absolute error of extended and standard Knudsen diffusion compared to the exact radiosity framework [108] for a finite cylinder with $d = 1$ a.u. and $\mathrm{AR} = 100$ for multiple values of β.

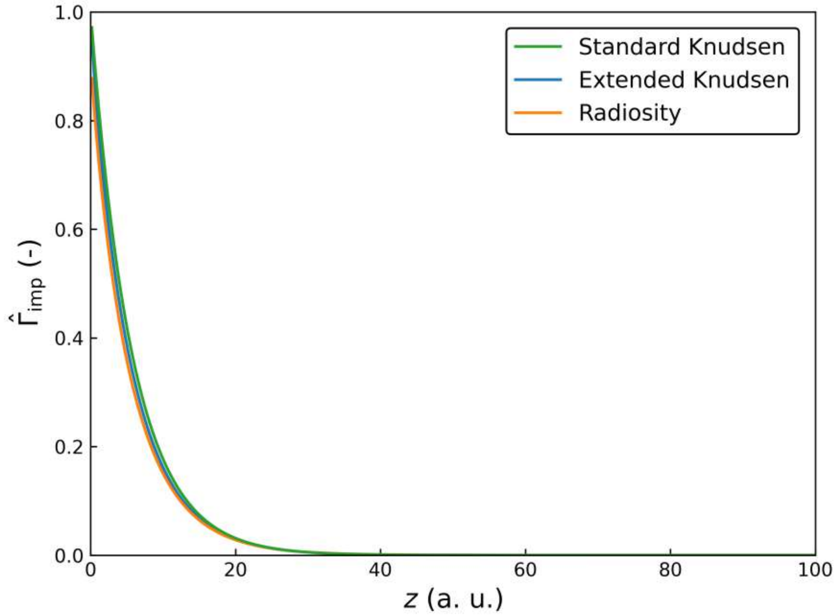

Figure 3.10: Linear scale comparison of extended Knudsen diffusion to standard Knudsen and the radiosity framework [108]. Calculations were performed for a finite cylinder with $d = 1$ a.u., $\mathrm{AR} = 100$, and $\beta = 1\,\%$.

3.6 Applications

In this section, two hitherto unpublished applications of Knudsen diffusive transport are presented. Both of them are direct applications of the standard Knudsen diffusion derived in Section 3.2 under the approximation of constant β. Section 3.6.1 presents an analysis of AR dependent phenomena in RIE through a direct integration of $\hat{\Gamma}_{\text{imp}}$, while Section 3.6.2 presents a variation of standard Knudsen diffusivity including the direct flux more directly than the presentation in Section 3.5. The latter is applied to model heteroepitaxial growth of cubic silicon carbide (3C-SiC) on silicon (Si).

3.6.1 Aspect Ratio Dependent Reactive Ion Etching

RIE is a plasma processing technique which enables etching of high AR structures [129]. This is achieved through the combination of at least two different reactants: Neutrals and ions. It is known since the groundbreaking work by Coburn and Winters [130] that the combined etch rate due to both neutrals, such as chlorine gas (Cl_2), and ions, like argon (Ar^+), is much higher than their individual contributions. Since the ions are vertically accelerated due to the plasma sheath, this enables a considerable vertical etch and, thus, the etching of high AR structures.

However, since there is a nonzero lateral component due to the neutrals which are not vertically accelerated, additional chemical reactions were developed to passivate the sidewalls [131]. For example, fluorocarbon containing plasmas naturally deposit a C_xF_y polymer layer which protects the surface from etching. The reactor is then fine-tuned so that the neutrals are unable to strip the polymer layer by themselves. Instead, only the bottom has the protective polymers removed, since it is affected by both neutrals and ions. This increased selectivity due to sidewall passivation enables even higher ARs. Therefore, ever more complex modeling flux models, with a precise description of the three involved reactant species, are required to accurately reproduce experimental topographies [43, 132].

The further development of RIE requires tremendous engineering effort to overcome its grand challenges [133]. From those many challenges, one crucial issue which must be addressed is that of aspect ratio dependent etching (ARDE): An observed reduction in etch rates as the AR increases. This phenomenon can have multiple overlapping causes [134], such as ion shading, bulk or surface diffusion, or even electric charge effects. However, the cause which has received the most research attention has been the restricted transport of neutral species towards the bottom of the feature [129].

This situation of restricted neutral transport is an ideal candidate for investigation of the so far discussed Knudsen diffusivity, so much so that it is usually named "Knudsen transport" in the literature [134]. In order to reduce the complex RIE problem to a single representative particle, a few assumptions about the process must be made. Firstly, it is assumed that the ion transport is perfectly vertical. That is, it does not affect vertical sidewalls and the ion flux at the bottom is independent of the AR. This vertical ion transport also completely removes any possible passivation layers at the bottom.

Thus, both the sidewall and the bottom may have different chemical compositions which are approximately represented by the respective constant sticking coefficients β_{wall} and β_{bottom}. This assumption means that the sidewalls are uniformly coated with an infinitesimally thin protective film and the bulk material at the bottom is fully exposed. Since there are now two involved sticking coefficients, the ODE and necessary BCs for $\hat{\Gamma}_{\text{imp}}(z)$ in a cylinder with diameter d, first presented in Section 3.2, now take the form:

$$\frac{d^2\hat{\Gamma}_{\text{imp}}}{dz^2} = \frac{3}{d}\beta_{\text{wall}}\hat{\Gamma}_{\text{imp}}(z) \tag{3.54}$$

$$\hat{\Gamma}_{\text{imp}}(0) = 1 \tag{3.55}$$

$$\left.\frac{d\hat{\Gamma}_{\text{imp}}}{dz}\right|_{z=L} = \frac{3}{4d}\beta_{\text{bottom}}\hat{\Gamma}_{\text{imp}}(L) \tag{3.56}$$

Equation (3.54) has the exact solution:

$$\hat{\Gamma}_{\text{imp}} = e^{-\frac{z\sqrt{3\beta_{\text{wall}}}}{d}} \frac{3\beta_{\text{bottom}}\left(e^{\frac{2L\sqrt{3\beta_{\text{wall}}}}{d}} - e^{\frac{2z\sqrt{3\beta_{\text{wall}}}}{d}}\right) + 4\sqrt{3\beta_{\text{wall}}}\left(e^{\frac{2L\sqrt{3\beta_{\text{wall}}}}{d}} + e^{\frac{2z\sqrt{3\beta_{\text{wall}}}}{d}}\right)}{3\beta_{\text{bottom}}\left(e^{\frac{2L\sqrt{3\beta_{\text{wall}}}}{d}} - 1\right) + 4\sqrt{3\beta_{\text{wall}}}\left(e^{\frac{2L\sqrt{3\beta_{\text{wall}}}}{d}} + 1\right)} \tag{3.57}$$

Since Eq. (3.57) is numerically unstable in the limit $\beta_{\text{wall}} \to 0$, due to it approaching $0/0$, an exact solution can be directly obtained from Eq. (3.54) for $\beta_{\text{wall}} = 0$:

$$\hat{\Gamma}_{\text{imp},\beta_{\text{wall}}=0} = \frac{4d + 3\beta_{\text{bottom}}(L - z)}{4d + 3\beta_{\text{bottom}}L} \tag{3.58}$$

The empirical observation of ARDE is that, as the AR increases, the etch rate decreases. However, in many cases what is measured is not the instantaneous etch rate. Instead, the etch time t_{etch} and plane wafer etch rate PWR are usually well-defined, leading to an expected ideal etch depth $L_{\text{ideal}} = t_{\text{etch}} \cdot PWR$. The observation is then of a reduced etch depth L_{ARDE} due to ARDE which can in turn be empirically related to etch rates. Nonetheless, the derived Eqs. (3.57) and (3.58) enable the direct calculation of L_{ARDE} which, additionally to providing insight into the ARDE phenomenon, also enables the single-step simulation of topographies through Boolean operations [48].

Since the RIE is assumed to be limited by a single species, L_{ARDE} can be calculated from the impinging flux at the bottom of the feature L at each time step and the definition of PWR from Eq. (2.8):

$$L_{\text{ARDE}} = \int_0^{t_{\text{etch}}} v(z{=}L, t)dt = \int_0^{t_{\text{etch}}} \hat{\Gamma}_{\text{imp}}(L) \cdot PWR\,dt = \int_0^{L_{\text{ideal}}} \hat{\Gamma}_{\text{imp}}(L)dL \tag{3.59}$$

Equation (3.59) has the following solution for the nonzero β_{wall} case

$$L_{\text{ARDE}} = \frac{8d}{4\beta_{\text{bottom}} + 4\sqrt{3\beta_{\text{wall}}}} A \left[\arctan\left(A e^{\frac{L_{\text{ideal}}\sqrt{(3\beta_{\text{wall}})}}{d}}\right) - \arctan A\right], \tag{3.60}$$

where

$$A = \sqrt{\frac{16\beta_{\text{wall}} - 3\beta_{\text{bottom}}^2}{16\beta_{\text{wall}} + 3\beta_{\text{bottom}}^2 - 8\beta_{\text{bottom}}\sqrt{3\beta_{\text{wall}}}}}\,. \tag{3.61}$$

For the zero β_{wall} case, the expression takes the simpler form

$$L_{\text{ARDE},\beta_{\text{wall}}=0} = \frac{4d}{3\beta_{\text{bottom}}} \ln\left(1 + \frac{3L_{\text{ideal}}\beta_{\text{bottom}}}{4d}\right). \tag{3.62}$$

With these expressions having been derived, it is now possible to precisely evaluate the impact of the restricted neutral impact with the increase of AR. To that end, a measure of etch depth attenuation due to ARDE is defined as $L_{\text{ARDE}}/L_{\text{ideal}}$. Both the attenuation and the achieved AR can be calculated for varying values of L_{ideal}, representing the effect of increasing the t_{etch}. These results are shown in Fig. 3.11 for a cylinder of diameter $d = 1$ a.u. and $\beta_{\text{bottom}} = 1\,\%$.

In Fig. 3.11, it can be seen that the attenuation is very sensitive to β_{wall}. In fact, for all positive values of β_{wall}, it can be seen that the AR reaches a finite value. This is an indication that the interactions between the neutral etchants and the polymer film, here described β_{wall}, must be very carefully engineered to enable higher ARs. If this is not carefully considered, the standard approaches of increasing reactor pressure and t_{etch} to overcome ARDE [129] will be fruitless.

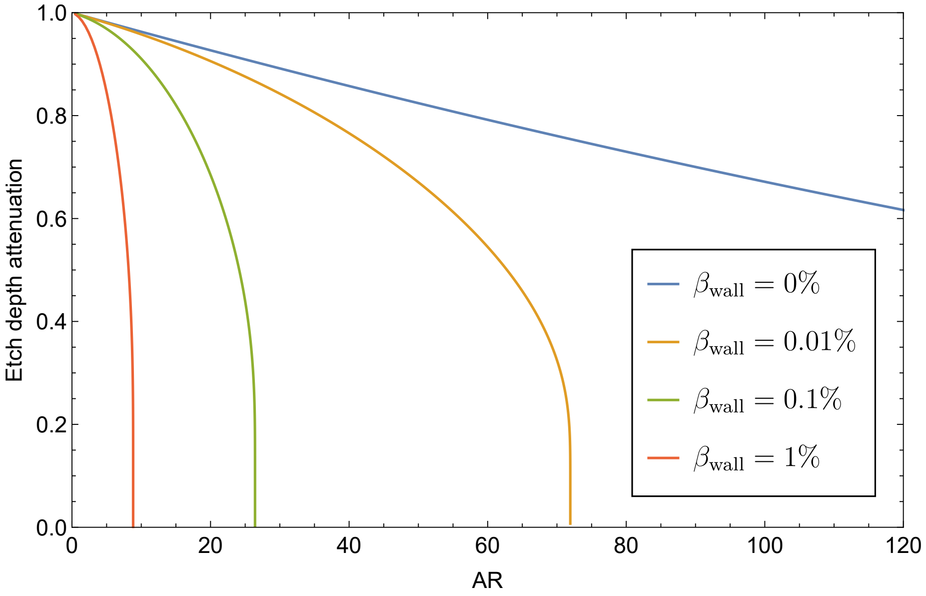

Figure 3.11: Etch depth attenuation due to ARDE as a function of AR calculated using Knudsen diffusivity for a cylinder with $d = 1$ a.u. and $\beta_{\text{bottom}} = 1\,\%$.

Notably, by calculating the limit $L_{\mathrm{ideal}} \to \infty$ for L_{ARDE} in Eq. (3.60) and dividing it by d, an expression for the maximum achievable AR which does not depend on d can be obtained. This limit is plotted in Fig. 3.12, where the interplay between β_{wall} and β_{bottom} can be evaluated. Although a β_{wall} far below 0.01 % is strictly necessary for enabling features with AR above 100, engineering effort must also be put at the interaction between the reactant and the exposed bottom surface. Nonetheless, the limit calculation of the maximum achievable AR diverges for $\beta_{\mathrm{wall}} = 0$ but not for $\beta_{\mathrm{bottom}} = 0$, therefore, the ultimate enabler of very high AR is the control over the interactions with the sidewall material.

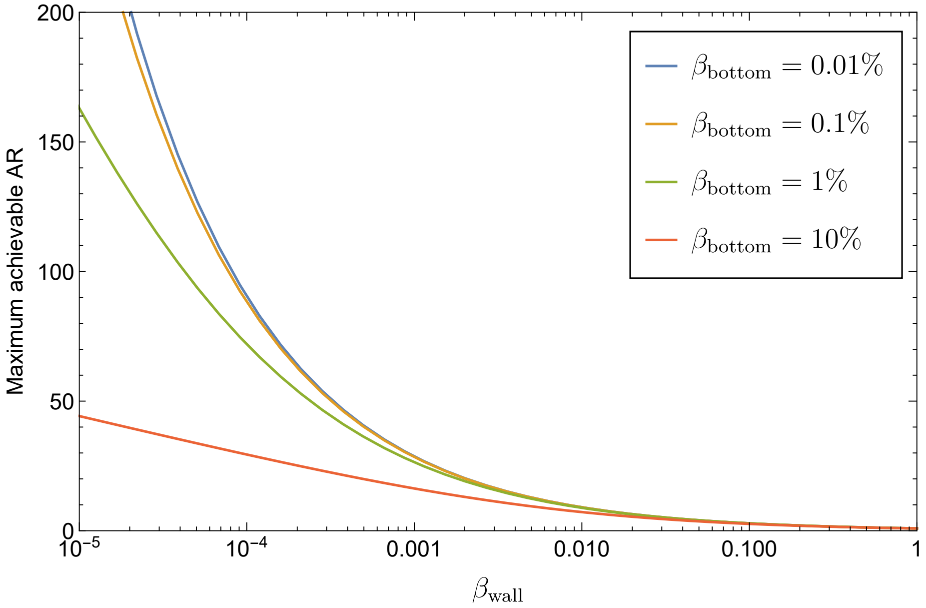

Figure 3.12: Maximum achievable AR in RIE restricted by neutral transport as a function of β_{wall} for different values of β_{bottom}.

3.6.2 Heteroepitaxial Growth of 3C-SiC on Si

3C-SiC is a promising material for power electronic applications, in particular in the 600−1200 V range [135]. Although the 4H-SiC allotrope has found more widespread commercial application [136], it is usually applied to a higher voltage range. To enable the further development and implementation of 3C-SiCs technology, the open scientific question of growing high-quality 3C-SiC substrates must be addressed. This material cannot be heteroepitaxially grown on a standard plane Si wafer without large defects due to the large lattice mismatch, even for comparatively more compatible Si(111) wafers [137].

To bridge this gap and enable highly crystalline 3C-SiC within the framework of well-established Si wafer technology, a methodology involving micro-pillars has been proposed by Kreiliger *et al.* [138]. In their methodology, hexagonal arrays of micro-pillars are etched on a Si(111) wafer using deep reactive ion etching (DRIE).

Then, 3C-SiC is heteroepitaxially grown on top of these micro-pillars using a low-pressure CVD reactor with ethylene (C_2H_4) and trichlorosilane (TCS) as reactants. By carefully engineering the dimensions and spacing of the micro-pillars, defects can be minimized, since the growing crystals coalesce into a continuous layer in a manner which is more favored by the lattice structure.

As there is a large degree of required optimization of the involved geometry, in particular with respect to the interaction between the shape of the micro-pillar and the crystal-direction dependent growth of 3C-SiC, topography simulation can play a helpful role. Previously, a detailed phase-field approach to model growth and coalescence has been proposed [139]. This model involves effects which are commonly not integrated within level-set (LS) based topography simulation, notably surface diffusion. However, the impinging reactant fluxes are modeled by assuming a combination of vertical and isotropic components. This is unusual for CVD processes since, as discussed in Chapter 2, the reactants are assumed to be isotropically distributed if no acceleration mechanism, such as a plasma sheath, is present [30].

This motivates the development of a simple reactive transport model in order to model this growth process with the LS method. Similarly to the case of anisotropic wet etching described in Section 2.3.1 and to LS modeling of solid phase epitaxial regrowth (SPER) [140], a crystallographic-orientation dependent (i.e., surface normal $\vec{n}$ dependent) velocity field $v_{\text{crystal}}(\vec{n})$ can be built via interpolation of calibrated growth rates R_m for each involved crystal plane m [87, 141]. However, since a low-pressure CVD reactor is inherently transport-controlled, the growth rate must be modulated by a local impinging flux

$$v(\vec{r},t) = \hat{\Gamma}_{\text{imp}}(\vec{r}) \cdot v_{\text{crystal}}(\vec{n}(\vec{r}))\,, \tag{3.63}$$

where $v_{\text{crystal}}(\vec{n}(\vec{r}))$ is given by Eq. (2.9). The development and calibration of $v_{\text{crystal}}(\vec{n})$ was performed by the colleague Alexander Toifl of the Christian Doppler Laboratory for High Performance Technology Computer-Aided Design (HPTCAD), while the development of the local impinging flux model is the focus of this thesis.

From a visual analysis of the reported growth profiles in [139], it can be noted that the majority of the growth occurs at the top of the pillar, however, with some infiltration present below the maximum lateral extent. This indicates that the involved reactants have a high but not 100 % sticking coefficient β, since there is growth in regions not directly visible to the reactor. Therefore, the direct flux must be taken into account in combination with the infiltration process which can be interpreted as Knudsen diffusion. To efficiently model this combination of factors without recurring to the complex calculations from, e.g., Section 3.5, the impinging flux can be divided into a sum of two components. One is due to the direct flux $\hat{\Gamma}_{\text{direct}}$ which can be calculated using the bottom-up approach discussed in Section 2.3.2 and the efficient algorithms present in Silvaco's Victory Process [55], and the other is the Knudsen flux $\hat{\Gamma}_{\text{Kn}}$. These components are combined via

$$\hat{\Gamma}_{\text{imp}} = B \cdot \hat{\Gamma}_{\text{direct}} + (1-B) \cdot \hat{\Gamma}_{\text{Kn}}\,, \tag{3.64}$$

where B is a model parameter which dictates the relative strength of the direct flux component. B can be interpreted as a rough approximation to β, assuming a single effective particle.

The evaluation of $\hat{\Gamma}_{\mathrm{Kn}}$ for evolving micro-pillars poses a specific set of problems. The central issue is that it is not straightforward to map from the dynamically evolving micro-pillar to an equivalent cylinder, which is the reference for the Knudsen diffusion equations derived so far. Although an EAR has been proposed for square pillars [110], its value is not rigorously calculated. Instead, the calculation of $\hat{\Gamma}_{\mathrm{Kn}}$ for the involved micro-pillars is done by directly considering the Thiele modulus h_T^2 from Eq. (3.27) as a model parameter. Since h_T^2 represents the ratio of the reaction rate to the transport rate [50, 124], this is a considerably coarse approximation. In essence, it is assumed that the transport rate is constant as the pillars coalesce, that is, the increased constriction due to coalescence is disregarded. Also, both reactants are jointly approximated by a single effective particle with a fixed reaction rate. This leads to the modeling ODE:

$$\frac{d^2\hat{\Gamma}_{\mathrm{Kn}}}{dz^2} = h_T^2\hat{\Gamma}_{\mathrm{Kn}}(z) \tag{3.65}$$

To evaluate Eq. (3.65), two BCs are necessary. Instead of setting the reactor supply boundary condition at a fixed plane $z{=}0$, a boundary plane z_0 is dynamically extracted from the simulated topography. The z_0 plane is defined as that for which the maximum lateral (x,y) extent is achieved. That is, only below the z_0 plane the Knudsen diffusion processes takes place, as it is the region where multiple particle-geometry interactions are more likely to happen due to constriction. The reactor efficiency boundary condition then becomes

$$\hat{\Gamma}_{\mathrm{Kn}}(z{\geq}z_0) = 1\,. \tag{3.66}$$

Additionally, unlike Section 3.6.1, the flux near the bottom of the micro-pillar is of little importance, since no growth is experimentally observed there. Thus, to obtain a simpler expression which captures the essentials of the exponential behavior from Fig. 3.10, a simpler "bottomless" BC is employed

$$\lim_{z\to-\infty} \hat{\Gamma}_{\mathrm{Kn}}(z) = 0 \tag{3.67}$$

Therefore, the Knudsen flux has a straightforward exact solution:

$$\hat{\Gamma}_{\mathrm{Kn}} = \begin{cases} 1, & z \geq z_0 \\ e^{h_T(z-z_0)}, & z < z_0 \end{cases} \tag{3.68}$$

This model has been implemented within Victory Process [55] and calibrated to the reported profiles from Masullo *et al.* [139]. The calibrated parameters are reported in Tab. 3.1. The results of the simulated topography after 60 min, including the time evolution of the facets and the comparison to the experimentally measured profiles, are shown in Fig. 3.13.

Thiele modulus	Direct flux component	Crystal growth rates [µm/h]			
h_T	B	R_{100}	R_{110}	R_{111}	$R_{1\bar{1}1}$
0.5	0.7	5.10	9.78	6.00	3.36

Table 3.1: Parameters for the heteroepitaxial growth model of 3C-SiC on Si micro-pillars calibrated to experimental data from [139].

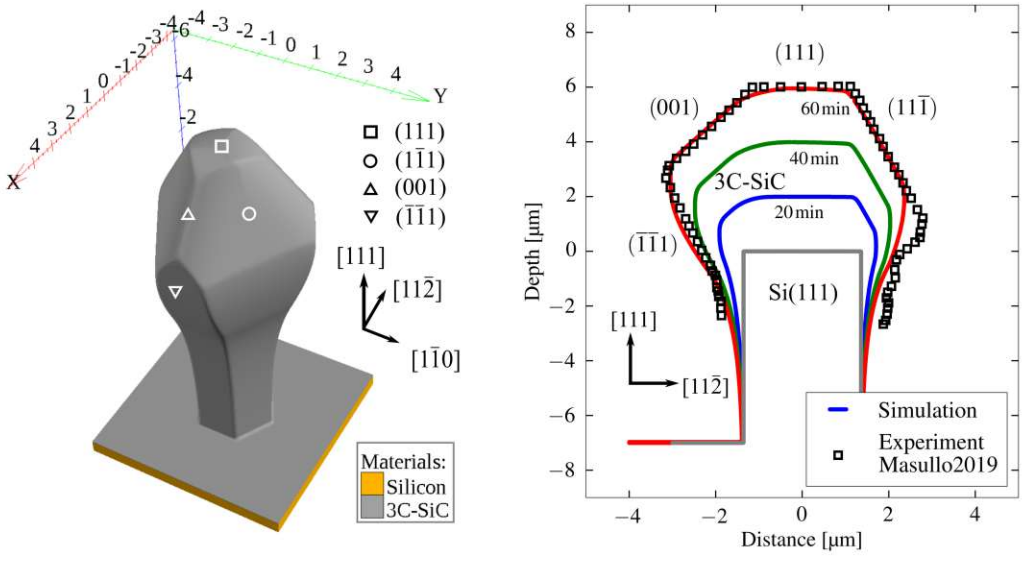

a) b)

Figure 3.13: a) Results of 3D growth simulation using the LS method after 60 min. b) Cross-section of the evolving 3C-SiC crystal and comparison to experimentally measured facets by Masullo *et al.* [139].

Figure 3.13 shows good agreement between the model combining both direct and Knudsen flux with the reported experiment, even after the use of rather coarse approximations. This is evidence that either the surface diffusion is not a critical determinant of the final profile, or that this process is effectively captured by the crystallographic growth rates R_m and the interpolation procedure. The discrepancy seen on the right-hand side of Fig. 3.13.b) is likely due to the use of a single boundary plane z_0 at an excessively high position, as z_0 is determined by the shape on the left-hand side of the image. Therefore, the flux is artificially restricted on the right-hand side. This can be alleviated by extracting a separate value of z_0 for each (x,y), or by a more accurate calculation approach such as the top-down tracking discussed in Section 2.3.3. Nonetheless, the success of the simulation means that it can be used for exploring different micro-pillar geometries. This is shown in Fig. 3.14 for simulated crystals after 30 min growth on four initial geometries, highlighting a path for future optimization.

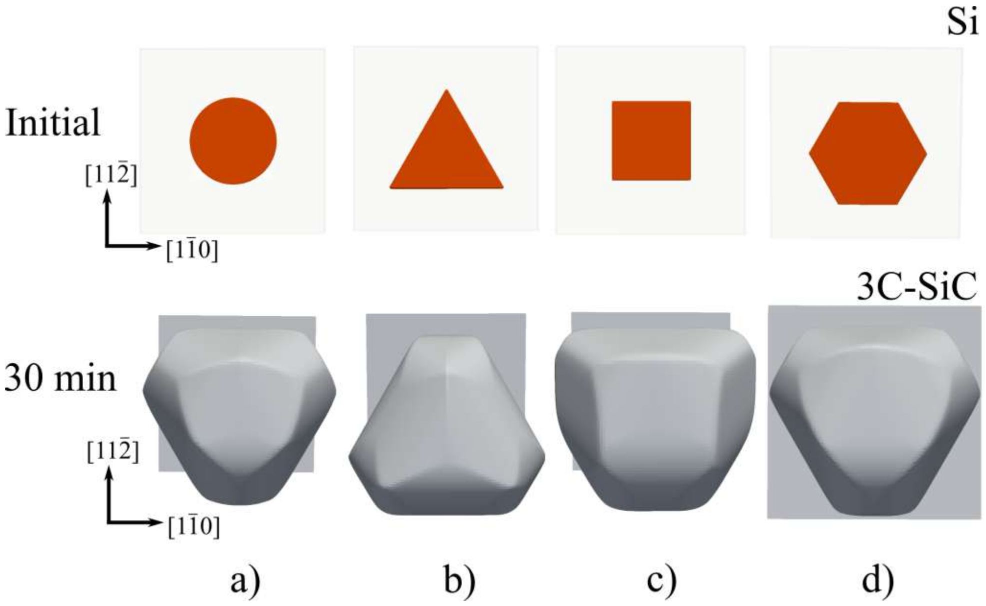

Figure 3.14: Simulated 3C-SiC crystals after 30 min growth for different initial Si micro-pillar geometries.

Chapter 4

Modeling of Thermal Atomic Layer Processing

From the many existing thin-film processing techniques, a certain class of methods has recently garnered increased attention: Thermal atomic layer processing (ALP) [129]. These methods are defined by their use of self-limiting — that is, a reaction which stops occurring after saturating the available surface sites — and thermodynamically favored surface-chemical behavior to achieve a very high degree of control of film quality and conformality. Such self-limiting reactions can be employed to enable controllable film growth, in what is called thermal atomic layer deposition (ALD) [142], or to precisely remove material through atomic layer etching (ALE) [143].

Due to its isotropic nature, thermal ALP is a key technology for three-dimensional (3D) integration [143], since it enables control over the materials at the sidewalls of high aspect ratio (AR) structures. To support the further development of these methods and to understand the impact of the processing conditions on the 3D structures, accurate modeling is required. Since the processes involve uncharged thus isotropically reflecting species, and the structures typically have high AR, thermal ALP is a great candidate for Knudsen diffusion-type modeling. In addition, these processes are commonly limited by a single reactant, therefore, single-particle models can be applied where the particle represents said chemical species. However, unlike the equations derived in Chapter 3, the constant sticking probability approximation cannot be used. As the methods themselves exploit self-limiting surface reactions, the models must include a more complete description of Langmuir surface kinetics including the coverage-dependent sticking coefficient $\beta(\Theta)$ presented in Section 2.2.

Own contributions: An integration of the aforementioned reactive transport model with level-set (LS) based topography simulation as well as its application are presented. This model is calibrated to reported experiments in order to derive physically meaningful insight from its parameters. Lastly, the model is applied to investigate non-idealities in a potential platform for 3D integration of novel memories. This work has been partially published at the SISPAD 2022 conference [144] and in a follow-up journal article currently under review [145].

4.1 Thermal Atomic Layer Deposition and Etching

ALP is a class of processing techniques which is defined by its high degree of authority over quality aspects of the processed structure [129]. The two main subcategories within ALP are the growth and etching procedures, respectively named ALD [142] and ALE [143]. The defining aspect of ALP techniques is that they divide the growth or etch reaction into at least two self-limiting reaction steps. Since each reaction is individually self-limiting and the surface evolution only occurs from the combination of reactions, excellent control over the conformality and thickness can be achieved. Similar self-limiting behavior is observed in the aluminum oxidation in Josephson junctions [29].

What defines *thermal* ALP in particular is that the involved reactions are thermodynamically favored by the reactor pressure and temperature [143, 146]. In contrast, plasma-assisted methods include an external electric field to generate neutral and ion species with differing chemical properties. In directional ALE, one of the reaction steps involves accelerated ions which modify the surface through their kinetic energy instead of a chemical reaction [129]. Plasma-assisted ALD instead takes advantage of highly chemically reactive but unstable neutral species which would otherwise not be possible in the same reactor temperature [147].

One crucial advantage of thermal ALP is that these techniques a higher degree of conformality in comparison to other processing methods such as conventional chemical vapor deposition (CVD) [110]. Conformality is the ability to uniformly modify a surface with a high degree of independence from the AR, so that the entire structure is grown or etched at the same rate. This is necessary for high AR structures such as dynamic random-access memory (DRAM) capacitors [148] or 3D NAND memory channel holes [149].

Should a given reactor setup and involved chemistry yield an ideal self-limiting reaction, then perfect conformality is in principle always achievable by adapting the reactor pulse time t_p until saturation is reached. Having determined the required t_p, the process is then determined straightforwardly by two parameters. The first parameter for ALD is the growth per cycle (GPC), or, equivalently, the etch per cycle (EPC) for ALE. These parameters are regularly measured and are usually fixed by the reactor and chemical setup [129]. Since they are in essence fixed, control over final grown or etched thickness is achieved by the second parameter: The number of cycles N_{cycles}.

In practice, however, this ideal behavior is not always observed for two main motives [110]. Firstly, the chemical reactions might not be perfectly self-limiting, thus an increase in t_p might not necessarily lead to saturation. Also, the reactant transport might be severely constricted, leading to regions where there is insufficient supply, i.e., the processing regime is transport-controlled. These two phenomena, namely chemical reactions and transport, are intrinsically linked and must be jointly considered in a *reactive transport* model, as first discussed in Chapter 2.

Before moving into describing the developed reactive transport model, it is important to briefly review the involved chemical reactions. The ALD of aluminum oxide (Al_2O_3) from water (H_2O) and trimethylaluminum (TMA), or $Al(CH_3)_3$, has emerged as a model system [142, 146]. Although this process has found application in DRAM [148], more importantly it has become the paradigmatic system for ALD due to its near-ideal surface chemistry. An idealization of this process is illustrated in Fig. 4.1, showing an initial OH-terminated surface which reacts with the TMA pulse. This reaction is illustrated as being ideally self-limiting and irreversible, so the TMA does not interact with a methyl-terminated surface and does not desorb as the reactor is purged. Similarly, the H_2O reacts irreversibly with the methyl-terminated surface only.

This idealized process can be represented by the following chemical reactions [142]:

$$\mathrm{AlOH}^* + \mathrm{Al(CH_3)_3} \rightarrow \mathrm{AlOAl(CH_3)_2^*} + \mathrm{CH_4}, \text{ and} \tag{4.1}$$

$$\mathrm{AlCH_3^*} + \mathrm{H_2O} \rightarrow \mathrm{AlOH}^* + \mathrm{CH_4}, \tag{4.2}$$

where the superscript * indicates a surface species. Although Eqs. (4.1) and (4.2) are useful for a cursory understanding of the processes, in reality there is still uncertainty about the details of the surface reactions including the involved stoichiometric factors [150].

For ALE, the involved chemistries are considerably more complex. It is substantially more challenging to find thermodynamically favored reactions which have as a product a volatilized surface species [143]. Usually, one of the reaction steps in fact deposits on the surface, changing its chemical composition. Then, the following reactions undergo a complex chemical process leading to a volatile etch product. There are a plethora of proposed methods to achieve this complex feat [143]. Similarly to ALD, Al_2O_3 can be used as the basis for an illustrative ALE process.

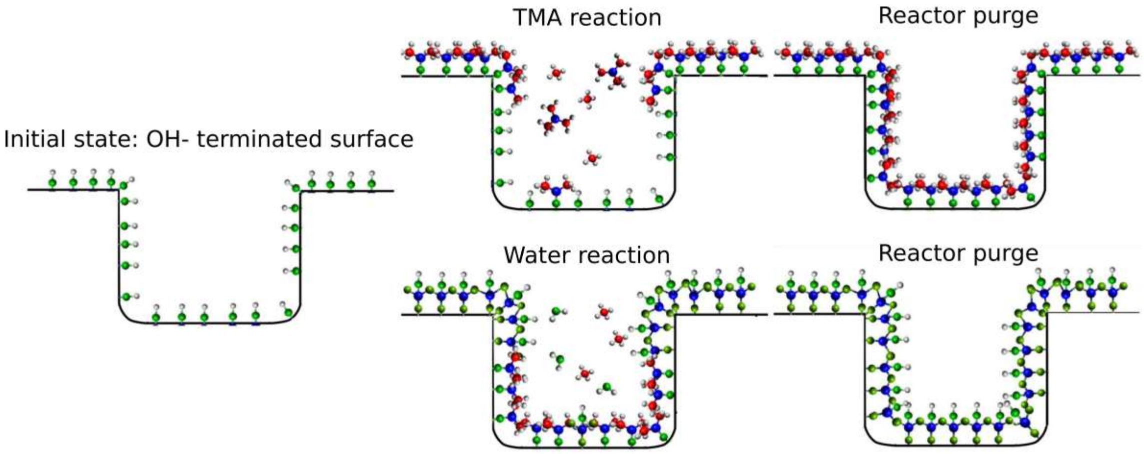

Figure 4.1: Illustration of ALD of Al_2O_3 from TMA and H_2O. Adapted from Cremers *et al.*, *Appl. Phys. Rev.* 6, (2019) p. 021302. [110], © The Authors, licensed under the CC BY 4.0 License, `https://creativecommons.org/licenses/by/4.0/`.

Lee and George [151] propose the thermal ALE of Al_2O_3 from fluorination and ligand-exchange using tin(ii) acetylacetonate ($Sn(acac)_2$) and hydrogen fluoride (HF). As an initial conditioning step, HF gas is introduced, converting the top layer of Al_2O_3 to aluminum fluoride (AlF_3). The ALE cycle then properly begins with the introduction of $Sn(acac)_2$ which then causes the following ligand-exchange

$$\mathrm{Al_2O_3|2AlF_3^* + 6Sn(acac)_2 \rightarrow Al_2O_3|}x\mathrm{SnF(acac)^* + 2Al(acac)_3 + (6-}x\mathrm{)SnF(acac)}\,, \tag{4.3}$$

where the | indicate a different surface species over a certain substrate and x is a temperature-dependent stoichiometric factor. The second ALE reaction is obtained by re-introducing HF which volatilizes any remaining tin-based compounds and again converts the top layer to AlF_3:

$$\mathrm{Al_2O_3|}x\mathrm{SnF(acac)^* + 6HF \rightarrow 2AlF_3^* + }x\mathrm{SnF(acac) + H_2O} \tag{4.4}$$

In summary, thermal ALP processes involve rich and complex chemical behavior. This complexity has only been briefly explored as this is an active field of research. For example, super-cycle combinations of ALD and ALE can be used to enable area-selective deposition (ASD) by exploiting differences in nucleation delays for each underlying material [152]. Nonetheless, all crucial chemical phenomena occur at the surface, thus a phenomenological approach, such as the first-order Langmuir surface kinetics introduced in Section 2.2, can provide valuable insight.

4.2 Reactive Transport in Atomic Layer Processing

As introduced in Section 4.1, there exists a wealth of complex chemistry in ALP. In order to develop a model which might be applied to real high AR structures, this complexity must be encapsulated in a simpler phenomenological model, since the underlying quantum chemical reality cannot be modeled at such large scale [153, 154]. To illustrate the construction of phenomenological first-order Langmuir surface kinetics, the H_2O step of the ALD of Al_2O_3 is taken as an example. Figure 4.2 depicts the three reaction pathways considered by such a model: An incoming H_2O molecule can either adsorb or reflect upon interacting with the surface, mediated by the coverage-dependent sticking coefficient $\beta(\Theta)$ from Eq. (2.4). In addition, an already adsorbed molecule is allowed to spontaneously desorb given a fixed evaporation flux Γ_{ev}.

Under the additional assumption that the H_2O supply is the only limiting factor (i.e., $\Theta_{\mathrm{TMA}}(\vec{r})$=1), the state of the surface is fully determined by the distribution of the H_2O coverage $\Theta_{\mathrm{H_2O}}(\vec{r})$ given by Eq. (2.3). That is, the particle involved in the reactive transport is the limiting chemical reactant. The complex chemical behavior is then condensed into two phenomenological parameters: β_0 and Γ_{ev}. The challenge with solving Eq. (2.3) is that it depends on the impinging water flux Γ_{imp} which itself depends on the surface state according to $\beta(\Theta)$.

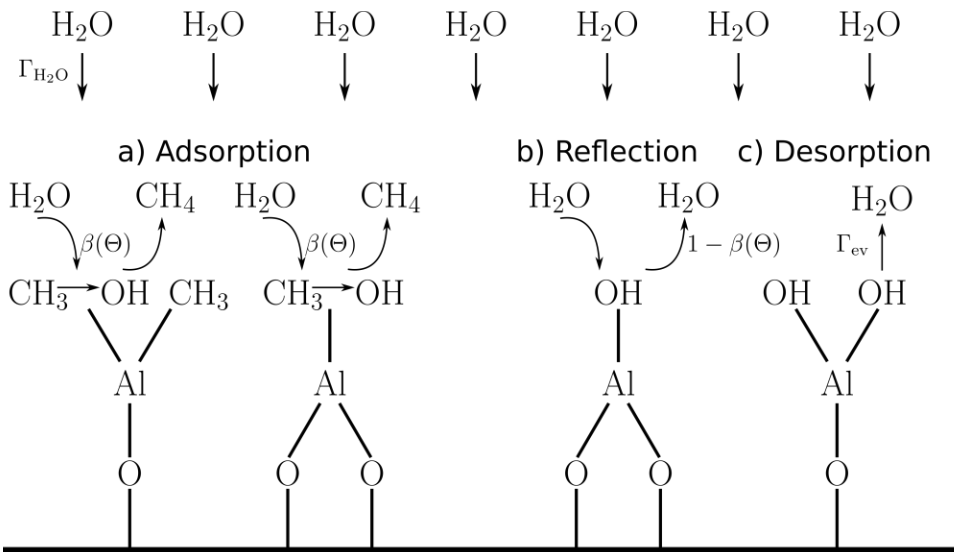

Figure 4.2: Reaction pathways modeled by first-order Langmuir kinetics of the H_2O step of the ALD of Al_2O_3. Reprinted from Aguinsky *et al.*, arXiv: 2210.00749, (2022) [145], © The Authors, licensed under the CC BY-NC-ND 4.0 License, `https://creativecommons.org/licenses/by-nc-nd/4.0/`.

To break this loop, Eq. (2.3) is discretized using the forward Euler method up to the pulse time t_p, obtaining

$$\Theta^{n+1}_{H_2O}(\vec{r}) = \Theta^{n}_{H_2O}(\vec{r}) + h_t s_0 \Gamma^{n}_{\mathrm{imp},H_2O}(\beta(\Theta^{n}_{H_2O}), \vec{r})\beta_0(1 - \Theta^{n}_{H_2O}(\vec{r})) - h_t s_0 \Gamma_{\mathrm{ev}} \Theta^{n}_{H_2O}(\vec{r}) \, , \tag{4.5}$$

where n is a time integration index going from 0 to N_t total steps, such that the time step length is $h_t = t_p/(N_t + 1)$. The initial condition is $\Theta^{0}_{H_2O}(\vec{r}) = 0$. Assuming that the $\Gamma_{\mathrm{imp},H_2O}$ is normalized to Γ_{source} according to Eq. (2.7), a simple estimation for the stability of Eq. (4.5) is:

$$h_t < \frac{1}{s_0\left(\beta_0 \Gamma_{\mathrm{source}} + \Gamma_{\mathrm{ev}}\right)} \tag{4.6}$$

The surface site area s_0 can be calculated from the stoichiometric ratio between the number of deposited atoms present in the reactant formula to those in the film formula $b_{\mathrm{reactant}}/b_{\mathrm{film}}$, the film mass density ρ, the film molar mass M, the GPC, and Avogadro's constant N_0 as [109]

$$s_0 = \frac{b_A}{b_{\mathrm{film}}} \frac{M}{N_0 \cdot \mathrm{GPC} \cdot \rho} \, . \tag{4.7}$$

For the H_2O step of the ALD of Al_2O_3, $b_{H_2O}/b_{Al_2O_3} = 1/3$, and the remaining factors can be experimentally measured and are usually reported. It is important to note that Eq. (4.7) is only an approximation to the surface site area, since, e.g., the effects of steric hindrance [68] are not included.

Although the discretization from Eq. (4.5) solves the issue of the coupling between reactant transport and surface chemistry, it does so at the cost of performing the transport calculation N_t times per advection step. In topography simulations of conventional processes such as reactive ion etching (RIE), the involved Langmuir equations are assumed to be on the steady-state [41, 43], thus only a single transport calculation is required per advection step. Therefore, the use of an accurate top-down pseudo-particle tracking approach to Γ_{imp}, presented in Section 2.3.3, can be exceedingly demanding for computational resources. Nonetheless, the use of Monte Carlo pseudo-particle tracking has been reported for ALD [101, 155].

To avoid this large computational cost and, therefore, to enable more efficient investigations of the effect of the parameters an one-dimensional (1D) diffusive model can be used. The approach of combining Knudsen diffusion and Langmuir kinetics has been first introduced for ALD by Yanguas-Gil and Elam [30, 111, 124]. However, their approach assumes irreversible adsorption, i.e., Γ_{ev}=0. According to the formulation of Chapter 3, the diffusive reactive transport ordinary differential equation (ODE) in the preferential transport direction $z \in [0, L]$ can be written as follows:

$$D\frac{d^2\Gamma_{\mathrm{imp}}}{dz^2} = \bar{s}\beta_0(1-\Theta(z))\frac{\bar{v}}{4}\Gamma_{\mathrm{imp}}(z) \tag{4.8}$$

$$\Gamma_{\mathrm{imp}}(0) = \Gamma_{\mathrm{source}} \tag{4.9}$$

$$D\left.\frac{d\Gamma_{\mathrm{imp}}}{dz}\right|_{z=L} = -\beta_0(1-\Theta(L))\frac{\bar{v}}{4}\Gamma_{\mathrm{imp}}(L) \tag{4.10}$$

The formulation in Eq. (4.8), differently than that from [124], enables more versatility in the calculation of D. The diffusivity can be calculated not only via the standard Knudsen diffusivity from Eq. (3.24), but it can also include the geometric factors for rectangular trenches discussed in Section 3.3, as well as transitional flow through the Bosanquet interpolation formula from Eq. (3.44). The thermal speed $\bar{v}$ is calculated using the reactor temperature and reactant molar mass using Eq. (3.4). The source flux Γ_{source} is inferred from the reactant partial pressure using the Hertz-Knudsen relationship from Eq. (3.7).

Equations (4.8) to (4.10) require a numerical solution. They are solved using a central finite differences scheme by dividing the z domain in $N_z + 1$ slices of size $h_z = L/(N_z + 1)$ and index k. The following tridiagonal equation system is obtained:

$$\Gamma_{k+1} - \left[2 + \frac{h_z^2}{3}\frac{\bar{v}^2}{D^2}\beta_0\left(1-\Theta_k\right)\right]\Gamma_k + \Gamma_{k-1} = 0 \tag{4.11}$$

$$\Gamma_0 = \Gamma_{\mathrm{source}} \tag{4.12}$$

$$-\left[2 + \left(\frac{h_z^2}{3}\frac{\bar{v}^2}{D^2} + \frac{h_z}{2}\frac{\bar{v}}{D}\right)\beta_0\left(1-\Theta_{N_z}\right)\right]\Gamma_{N_z} + 2\Gamma_{N_z-1} = 0 \tag{4.13}$$

This tridiagonal system is solved using the general banded matrix solver from LAPACK [156] with the OpenBLAS library [157].

The crucial assumption behind phenomenological modeling is that the model parameters, namely β_0 and Γ_{ev}, are strongly correlated to the reactor conditions. Therefore, before moving to the parameter investigations with support of experimental data in Section 4.4, it is important to investigate the effects of the model parameters over conformality. To quantify conformality, two calculations are performed for each pair of parameters. First, the saturation coverage Θ_{sat} is calculated at $z{=}L$ as the steady-state convergence ($d\Theta/dt = 0$) of Eq. (4.5). Then, a second calculation is performed, now to calculate the required t_p to achieve 95% of Θ_{sat}. A region of the parameter space is shown in Fig. 4.3, calculated with standard Knudsen diffusivity for a cylinder with $d = 1\,\mu\mathrm{m}$ and $L = 100\,\mu\mathrm{m}$, and a fictitious reactor chemistry with $s_0 = 2 \cdot 10^{-19}\,\mathrm{m}^{-2}$ and $\Gamma_{\mathrm{source}} = 10^{24}\,\mathrm{m}^{-2}\mathrm{s}^{-1}$.

Figure 4.3 indicates that the required t_p is mostly impacted by the β_0 parameter, as the gradient varies little across the y axis. Instead, the impact of Γ_{ev} is on restricting the maximum achievable Θ_{sat}, as seen in the upper left-hand side of the figure. That is, Γ_{ev} severely limits the maximum AR which can be conformally processed by an ALP reactor configuration, even for values as low as one millionth of Γ_{source}.

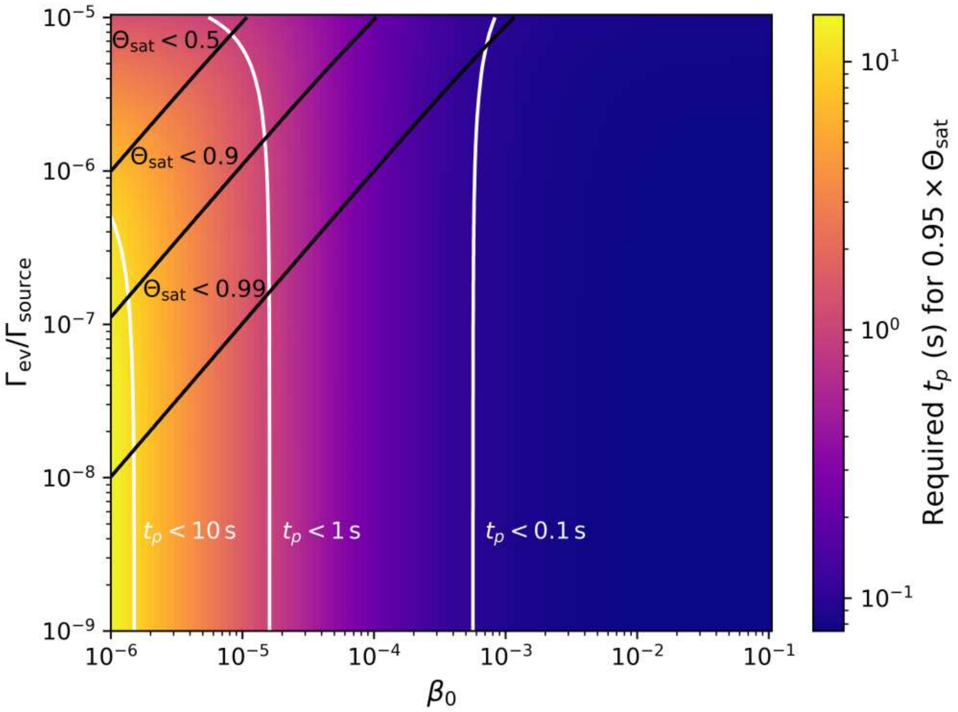

Figure 4.3: Investigation of phenomenological model parameters (β_0 and Γ_{ev}) on the required t_p to reach 95 % of Θ_{sat} for a cylinder with $d = 1\,\mu\mathrm{m}$ and $L = 100\,\mu\mathrm{m}$ and a fictitious chemistry with $s_0 = 2 \cdot 10^{-19}\,\mathrm{m}^{-2}$ and $\Gamma_{\mathrm{source}} = 10^{24}\,\mathrm{m}^{-2}\mathrm{s}^{-1}$. Reprinted from Aguinsky *et al.*, arXiv: 2210.00749, (2022) [145], © The Authors, licensed under the CC BY-NC-ND 4.0 License, `https://creativecommons.org/licenses/by-nc-nd/4.0/`.

4.3 Integration with the Level-Set Method

Ultimately, the reactive transport model presented in Section 4.2 must be integrated within a topography simulator to evaluate the experimental quantities of interest, especially the film thicknesses, as well as to enable simulations of device operation. To achieve this integration in a LS based topography simulator, a velocity field $v(\vec{r}, t)$ must be constructed, as discussed in Section 2.2. However, unlike the growth rate proposed for conventional CVD [30] in Eq. (2.5), a velocity field for ALP requires a careful consideration of the involved time scales.

As conventional CVD is a steady-state process, the actual reactor operation time can directly be used in the solution of the LS equation in Eq. (2.2). In ALP, the pulse time t_p does not play the same role due to the self-limiting nature of the reactions. Instead, the changes in profile are controlled by the N_{cycles} and the involved GPC or EPC. Thus, to maintain unit consistency in Eq. (2.2), an artificial time t^* for the calculation of the evolution of the topography is defined as

$$t^* = \frac{N_{\text{cycles}}}{C}\,, \tag{4.14}$$

where C is a numerical constant. For the reasons discussed below, it has been observed that choosing C such that $t^* \approx 1$ is sufficient. Under the assumption that the reactive transport is limited by a single species, the factor limiting the conformality is the coverage distribution of said species. Therefore, the velocity field is constructed from $\Theta(z)$ calculated using Eqs. (4.5) and (4.11) as

$$v(\vec{r}, t) = v(z, t) = C \cdot \Theta(z) \cdot \begin{cases} \text{GPC, or} \\ -\text{EPC}\,. \end{cases} \tag{4.15}$$

This is in contrast to the modeling of aluminum oxidation, where the self-limiting nature is directly captured by the LS method [29]. Instead, Eq. (4.15) delegates the self-limiting aspects of the calculation to $\Theta(z)$, while the surface advection proceeds normally for the duration of t^*.

Effectively, the introduction of t^* in Eq. (4.14) means that multiple, but not all, ALP cycles are bundled in a single LS advection time step. LS based simulation treats $v(\vec{r}, t)$ as constant only during a single advection step which is limited to at most one grid spacing Δx according to the Courant-Friedrichs-Lewy (CFL) condition [59, 79]. That is, the actual bundling of cycles is given by $\Delta x / \max |v(\vec{r}, t)|$ and not t^*, as the inputs d and L of the calculation of $v(\vec{r}, t)$ are updated after each advection step. Notwithstanding, Δx must be carefully chosen so that variations in the distribution of $\Gamma_{\text{imp}}(\vec{r})$ are minimal *during* the advection step.

The calculation of $\Gamma_{\text{imp}}(\vec{r})$ presented in Section 4.2 is performed on N_z slices which might not necessarily correspond to the required z coordinates for the solution of the LS equation. This is addressed by storing the values of Θ at each k slice as a look-up table. Then, the values are linearly interpolated for the z coordinate of each evolving surface point $\vec{r}$. Since the presented model does not require any modifications to the LS method, it has been implemented using the Python interface of ViennaLS [158] as well as the user-facing Open Model Library of Silvaco's Victory Process [55].

4.4 Atomic Layer Deposition of Al_2O_3 from TMA and Water

To validate the proposed reactive transport model and, furthermore, to extract chemical insight from its parameters, experimental topographies must be considered. As previously discussed, the ALD of Al_2O_3 from H_2O and TMA, represented in Eqs. (4.1) and (4.2), has emerged as a paradigmatic system due to its near-ideal chemical characteristics [142, 146]. Therefore, there are multiple experimental studies reported for this process. Ultimately, the goal is to simulate film deposition profiles in trenches, as illustrated in Fig. 4.4, and thus calibrate and analyze the model parameters with support from reported experimental data.

In addition to the investigations of the surface chemistry of this ALD process [159], there has been increased attention in deliberately exploring the reactive transport in the transport-controlled regime. Gao *et al.* developed a silicon (Si)-based lateral high AR structure tailored for film conformality analyses [160] which was quickly adopted by several research groups. By suspending a polycrystalline Si membrane over an array of pillars, a lateral trench with very high AR is obtained. Since the involved transport processes are isotropic, this lateral cavity is equivalent to the vertical trench with initial opening d represented in Fig. 4.4. In addition, since this membrane can be peeled off using adhesive tape, the film thickness analyses can proceed with conventional optical profilometry instead of costly and complex electron micrography.

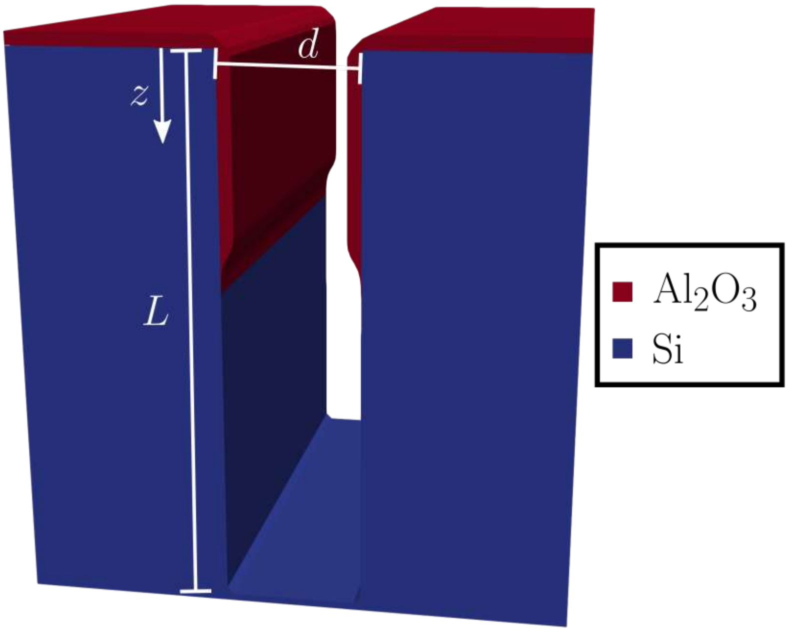

Figure 4.4: Illustration of simulated transport-controlled ALD of Al_2O_3 thickness distribution in the z direction in a Si trench with initial opening d and length L. Reprinted from Aguinsky *et al.*, arXiv: 2210.00749, (2022) [145], © The Authors, licensed under the CC BY-NC-ND 4.0 License, https://creativecommons.org/licenses/by-nc-nd/4.0/.

The following Sections 4.4.1 and 4.4.2 compare the proposed model to reported experimental film thickness for the H_2O-limited [161] and TMA-limited [109, 161, 162] regimes, respectively, in similar lateral high AR trenches ($d = 0.5\,\mu m$, except where noted, and $L > 1000\,\mu m$). For each regime, the reactive transport is modeled with a single particle which is assumed to be the limiting chemical species. All relevant physical parameters are taken directly from the original publications. However, some physical parameters are not reported, thus they are estimated as follows. For Arts *et al.* [161], the H_2O pulse time is estimated to be 0.1 s and the TMA pulse time to be 0.4 s. In Ylilammi *et al.* [109], the unreported TMA partial pressure is estimated to be 325 mTorr. Finally, for Yim *et al.* [162] the TMA partial pressure is assumed to be 160 mTorr. These assumptions are reasonable since they fall well within the range of possible values in the reported reactor conditions, as well as that they mostly impact the experimentally reported penetration depth.

Only Knudsen diffusion is considered, except where otherwise indicated. To use the standard Knudsen diffusivity equation from Eq. (3.24) in Eq. (4.11), the simulated geometry must be mapped to an equivalent long cylinder. To that end, the hydraulic diameter approximation from Eq. (3.33) is applied. However, from the discussion in Section 3.3, it must be remarked that this approximation is not rigorously justified. Thus, the calibrations discussed in the following are only valid for similar geometries and reactor conditions. Fortunately, even though the experimental results are obtained from several research groups, they all use very similar trenches and operate in similar vacuum conditions. Therefore, the use of the hydraulic diameter approximation is justified.

4.4.1 Temperature dependence of the H_2O step

Due to its inherent complexity, the metal-organic TMA has received more research attention. Also, its higher molar mass naturally causes a lower thermal speed and, therefore, it is usually the transport-limiting species. Recently, however, Arts *et al.* reported an experiment to investigate the sticking probability of H_2O using a simplified Knudsen diffusion method by deliberately engineering an H_2O-limited regime [161]. In addition to their estimates of β_0, they also report different Al_2O_3 film thickness profiles for three calibrated substrate temperatures: 150 °C, 220 °C, and 310 °C. These profiles are reproduced with the proposed reactive transport model integrated with LS based topography simulation, shown in Fig. 4.5. The calibrated parameters are manually obtained, and they are shown in Tab. 4.1.

The simulated thickness profiles from Fig. 4.5 show good agreement with experimental data. It is important to note that such agreement was not possible by assuming irreversible reactions (i.e., Γ_{ev}=0) which is strong evidence that reversibility plays a key role. The estimated values of β_0 are generally consistent with those estimated in the original publication which is expected since their methodology is also based on Knudsen diffusion and first-order Langmuir kinetics. However, their approach assumes irreversible reactions and only considers the slope of the thickness curve at 50% height. This is likely the reason for the discrepancy for the value of β_0 at 150 °C, since it is the configuration with a higher calibrated value of Γ_{ev}.

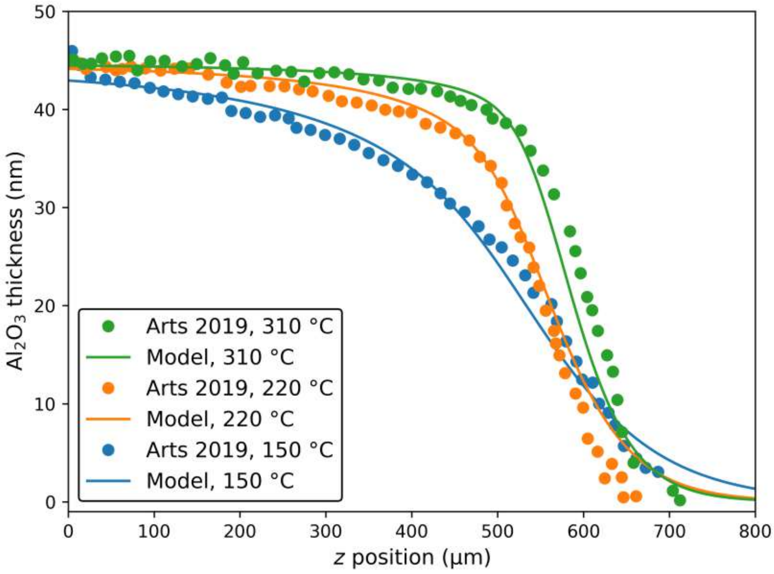

Figure 4.5: Comparison of simulated Al_2O_3 thicknesses in the H_2O-limited regime to experimental profiles reported by Arts *et al.* [161]. Reprinted from Aguinsky *et al.*, arXiv: 2210.00749, (2022) [145], © The Authors, licensed under the CC BY-NC-ND 4.0 License, `https://creativecommons.org/licenses/by-nc-nd/4.0/`.

Parameter	150 °C	220 °C	310 °C
Γ_{ev} ($m^{-2}s^{-1}$)	$6.5 \cdot 10^{19}$	$5.5 \cdot 10^{19}$	$3.5 \cdot 10^{19}$
β_0	$5.0 \cdot 10^{-5}$	$1.2 \cdot 10^{-4}$	$1.9 \cdot 10^{-4}$
β_0, estimated range from [161]	$1.4 \cdot 10^{-5}$ – $2.3 \cdot 10^{-5}$	$0.8 \cdot 10^{-4}$ – $2.0 \cdot 10^{-4}$	$0.9 \cdot 10^{-4}$ – $2.5 \cdot 10^{-4}$

Table 4.1: Phenomenological model parameters for the H_2O step of ALD of Al_2O_3 calibrated to reported experimental profiles by Arts *et al.* [161], including their estimates for β_0.

Since the parameters were extracted for three different temperatures, it is possible to perform an indicative Arrhenius analysis. This is present in Fig. 4.6, where the increase in β_0 and decrease of Γ_{ev} with higher T is made clear. This is evidence that, as temperature increases, permanent adsorption becomes more thermodynamically favorable. In addition, the fitted activation energy $E_A = 0.178\,\mathrm{eV}$ of β_0 can be interpreted as the reaction activation energy for a pristine surface. The fitted value is lower than what is suggested by first-principle studies [163], however, it is consistent with recent experimental studies. Sperling *et al.* report an experimental analysis using *in situ* infrared spectroscopy, extracting an activation energy of $(0.166 \pm 0.020)\,\mathrm{eV}$ for a two-stage reaction [159].

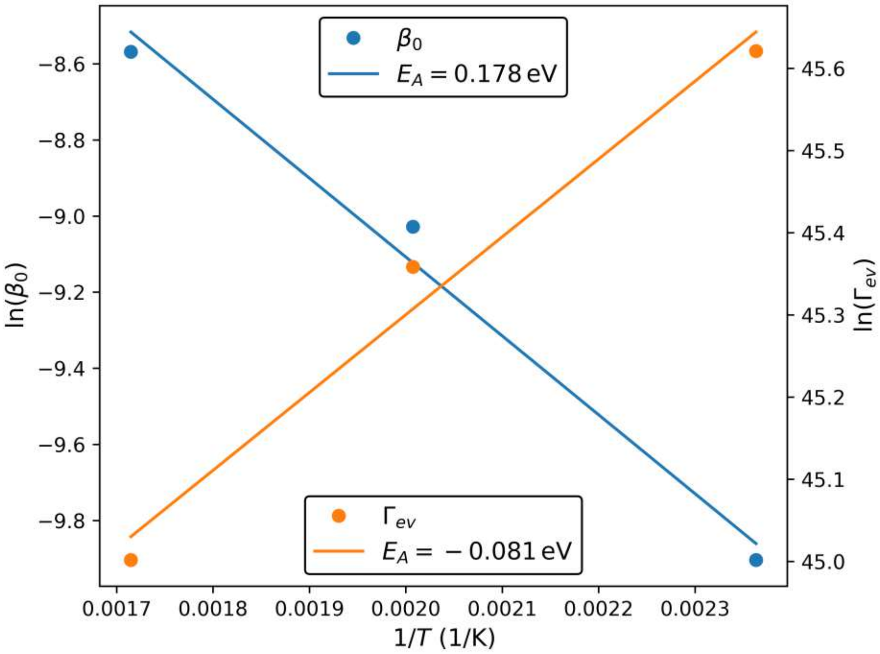

Figure 4.6: Arrhenius analysis of model parameters for H_2O step including the fitted activation energies E_A. Reprinted from Aguinsky *et al.*, arXiv: 2210.00749, (2022) [145], © The Authors, licensed under the CC BY-NC-ND 4.0 License, `https://creativecommons.org/licenses/by-nc-nd/4.0/`.

Having obtained an Arrhenius expression of the form $Ae^{\frac{-E_A}{k_B T}}$ for both model parameters, they can now be expressed in terms of a single physical variable: T. Therefore, the parameter analysis from Fig. 4.3 reduces from three to two dimensions which is shown in Fig. 4.7. As expected from a more thermodynamically favored reaction, the Θ_{sat} increases and the required t_p to reach 95 % of Θ_{sat} decreases with temperature. In practice, however, Θ_{sat} is not always experimentally accessible. Alternatively, the step coverage SC, defined as the ratio of film thickness at $z{=}L$ to that of a fully exposed plane, is commonly measured.

The proposed reactive transport model enables the estimation of the saturation step coverage from the steady-state limit of Eq. (4.5) as

$$\mathrm{SC}_{\text{sat}} = \frac{\Theta_{\text{sat}}(z=0)}{\Theta_{\text{sat}}(z=L)}\,. \tag{4.16}$$

This quantity is also calculated in Fig. 4.7 and, interestingly, it is almost constant and near unity through the entire T range. This is an indication that, even though low temperatures enable conformal films according to the SC metric, the film quality might be low. The low Θ_{sat} is an indication of possible defects such as voids and vacancies which is supported by the experimental observation that film deposited at lower temperatures require more energy to crystallize [164].

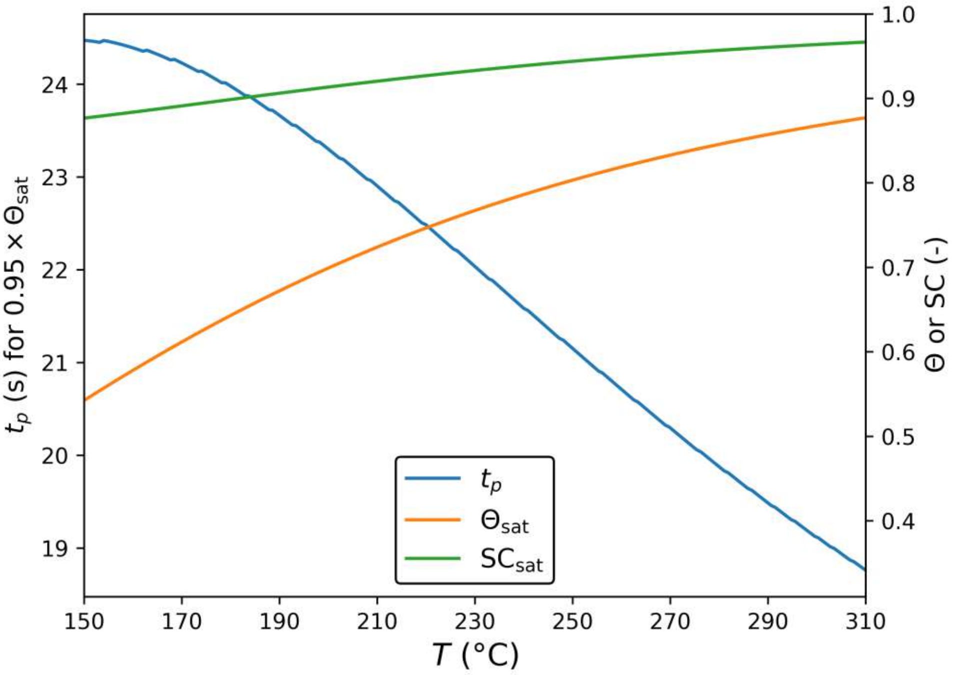

Figure 4.7: Effect of temperature T on the conformality metrics t_p, Θ_{sat}, and SC_{sat} using the Arrhenius fit from Fig. 4.6. Reprinted from Aguinsky *et al.*, arXiv: 2210.00749, (2022) [145], © The Authors, licensed under the CC BY-NC-ND 4.0 License, `https://creativecommons.org/licenses/by-nc-nd/4.0/`.

4.4.2 Geometric analysis of the TMA step

As previously indicated, the TMA step has received more research attention, therefore, multiple research groups report TMA-limited Al_2O_3 profiles using similar lateral high AR structures [109, 161, 162]. However, as shown in Fig. 4.7, film quality tends to increase with temperature, therefore, the TMA-limited studies all fall in a restricted reactor temperature range (275 °C for [161] and 300 °C for [109, 162]). These temperatures are all near the upper stability limit of TMA of ≈ 300 °C [146]. Thus, to investigate the robustness of the model parameters with respect to reactor temperature, all reported profiles are reproduced with the same parameters which are shown in Tab. 4.2. The comparison of the experimental profiles to simulation is given in Fig. 4.8.

The original publications provide their own estimates of β_0, also condensed in Tab. 4.2. The reported values are broadly consistent with the estimate using the proposed reactive transport model which is expected since all methods consider similar diffusive transport processes. However, both Arts *et al.* [161] and Yim *et al.* [162] assume irreversible reactions, whereas Ylilammi *et al.* consider reversible kinetics albeit with a different calculation methodology for the Knudsen diffusive process [109, 165]. This leads to Ylilammi *et al.* achieving the more similar estimate of β_0.

Γ_{ev} ($m^{-2}s^{-1}$)	β_0	β_0 from [109]	β_0 from [161]	β_0 from [162]
$3.0 \cdot 10^{19}$	$7.5 \cdot 10^{-3}$	$5.7 \cdot 10^{-3}$	$(0.5–2.0) \cdot 10^{-3}$	$4.0 \cdot 10^{-3}$

Table 4.2: Calibrated phenomenological model parameters for the TMA step of ALD of Al_2O_3 to multiple reported experimental profiles [109, 161, 162], including the estimates of β_0 from the original publications.

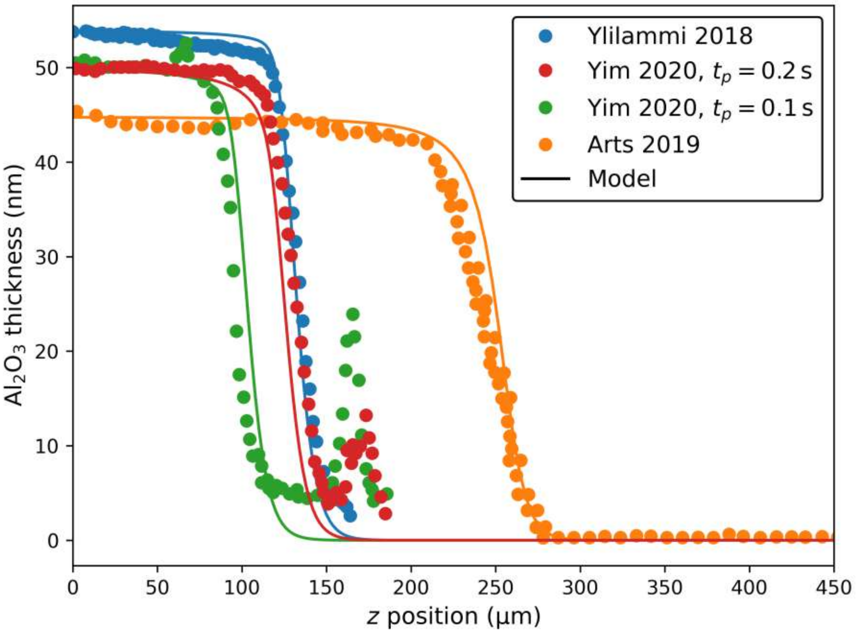

Figure 4.8: Comparison of simulated Al_2O_3 thicknesses in the TMA-limited regime using the parameters from Tab. 4.2 to experimental profiles in different reactors reported by Ylilammi *et al.* [109], Yim *et al.* [162], and Arts *et al.* [161]. Reprinted from Aguinsky *et al.*, arXiv: 2210.00749, (2022) [145], © The Authors, licensed under the CC BY-NC-ND 4.0 License, `https://creativecommons.org/licenses/by-nc-nd/4.0/`.

Figure 4.8 shows that a single parameter set is sufficient to adequately simulate the experimental profiles obtained from separate research groups using different ALD reactors. This strongly supports the hypothesis that not only the phenomenological model adequately captures the most relevant chemical aspects, but also that the model parameters are fixed by the chemical and reactor conditions, most importantly the reactor T. Furthermore, the larger deviation with respect to the simulation is that for the profile reported by Arts *et al.* [161] which was obtained using a slightly lower reactor temperature of 275 °C. This indicates that a similar temperature dependence of β_0 could be present, however, more data would be required to evaluate this claim. The secondary peaks in the experimental data from Yim *et al.* are reported to be spurious interactions of the measurement technique with the remaining sustaining pillars [162] and are, therefore, disregarded.

Yim *et al.* report additional experiments where the N_{cycles} is varied between 250 and 1000 cycles. The simulated geometries, obtained with the same parameters from Tab. 4.2, are compared to the experimental profile in Fig. 4.9. The lowest number of cycles shows good qualitative agreement. The penetration depth is slightly underestimated which could simply indicate that the estimate for the partial pressure should be adjusted. However, for $N_{\mathrm{cycles}} = 1000$ the disagreement is more pronounced also in the profile slope.

This is likely due to the lateral structure being over 40 % constricted in this case, since the same 100 nm growth also occurs on the removed membrane. Therefore, the approximation that the entire geometry can be modeled by a single representative trench width d fails. Additionally, this severe constriction changes the Knudsen number which, as discussed for Eq. (3.40), affects the validity of the hydraulic diameter approximation.

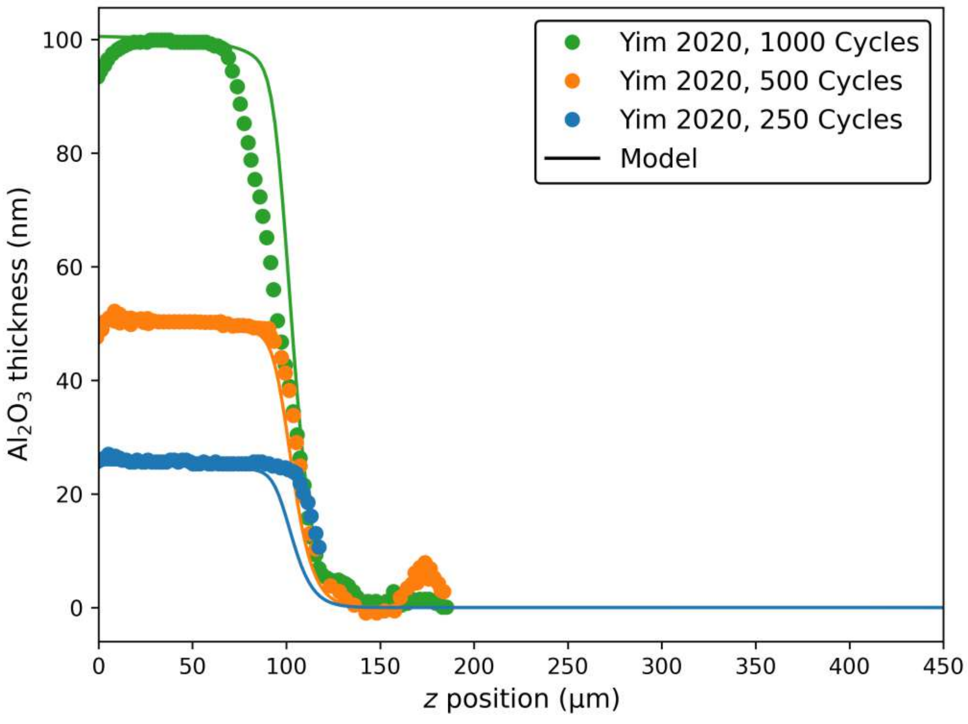

Figure 4.9: Comparison of deposited Al_2O_3 film thickness profiles with varying number of ALD cycles reported by Yim *et al.* [162] to simulations using the parameters from Tab. 4.2.

Additionally, Yim *et al.* report profiles obtained with lateral high AR structures with different trench openings [162]. These trenches are simulated with the parameters from Tab. 4.2 and shown in Fig. 4.10 with the label "Knudsen". The simulation shows good agreement for the trench with $d = 0.5\,\mu\text{m}$, however, the trench with $d = 0.1\,\mu\text{m}$ shows a slight deviation. This is due to the trench becoming completely constricted, similarly to the discussion for Fig. 4.9.

The simulation for the largest trench with $d = 2.0\,\mu\text{m}$ also deviates from the experimental data. As the width increases, the Knudsen number decreases according to Eq. (2.6), and is estimated to be $\text{Kn} \approx 8.9$ in this case. Therefore, the flow is in the transitional regime and the impact of molecule-molecule collisions cannot be disregarded. To improve accuracy, the Bosanquet interpolation formula [116] from Eq. (3.44) is applied, with D_{gas} calculated from Chapman-Enskog diffusivity [120] using the hard-sphere molecule diameters [109] $d_{\text{TMA}} = 591\,\text{pm}$ for TMA and $d_{\text{N}_2} = 374\,\text{pm}$ for nitrogen gas (N_2), the carrier gas. The simulation with improved accuracy is also shown in Fig. 4.10 with label "Bosanquet".

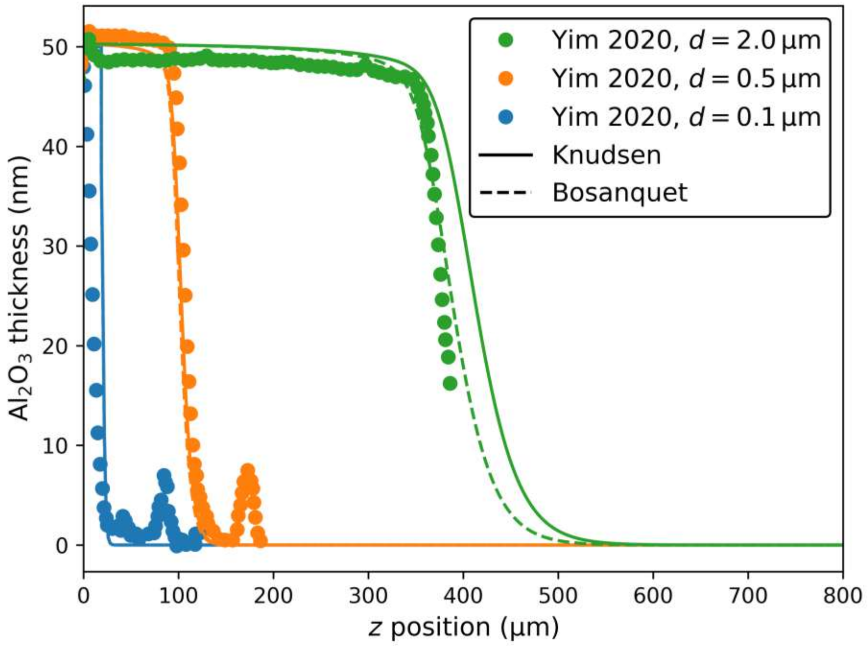

Figure 4.10: Comparison of deposited Al_2O_3 thickness in lateral trenches with different initial openings d reported by Yim *et al.* [162] to simulation. The lines labeled "Knudsen" assume pure Knudsen diffusion, while the lines labeled "Bosanquet" also include gas-phase diffusivity through the Bosanquet interpolation formula. Reprinted from Aguinsky *et al.*, arXiv: 2210.00749, (2022) [145], © The Authors, licensed under the CC BY-NC-ND 4.0 License, `https://creativecommons.org/licenses/by-nc-nd/4.0/`.

4.5 Atomic Layer Processing for Novel 3D Memory Technologies

One key technology which can be unlocked by the continuing development of thermal ALP is the 3D integration of novel memories [143]. The ongoing success of 3D NAND flash memory demonstrates that it is possible to create a charge storage structure — whether a charge trap or a floating gate — in a vertical 3D stack without relying on planar technology [105]. This stacking has enormously increased the density of memory technology, therefore, similar ideas can be applied to novel memory technologies such as resistive random-access memory (ReRAM) [166]. To enable the patterning of these sophisticated material stacks at the sidewalls of a high AR structure, conformality in thermal ALP will have to be taken to its limits. Topography modeling can be an invaluable tool in this development by providing insight into the reactive transport issues limiting conformality, as well as enabling the investigation and simulation of devices with realistic shapes.

To aid the development of new 3D memory technologies, Fischer *et al.* from Lam Research have developed a 3D NAND-like test structure and used it to investigate thermal ALD and ALE [149]. These structures are oxide-nitride (ON) stacks with either 76 or 98 ON pairs, to a maximum height of 4 µm or 5 µm respectively. After the ON deposition, a cylindrical hole is etched using RIE [26]. This hole is then used as the basis for the thermal ALP experiments. Afterward, the samples are cleaved and subsequently imaged with transmission electron micrography (TEM).

The material chosen to be investigated on the test structure is hafnium oxide (HfO_2) which is a promising material for novel memory technologies [166]. It was deposited using thermal ALD from H_2O and an undisclosed hafnium-based reactant [149], achieving a SC of 85 %. To simulate the reported thickness profile, the hafnium reactant is taken to be the limiting species and is assumed to be tetrakis(ethylmethylamino)hafnium (TEMAH), with the necessary parameters taken from [167]. The calibrated parameters are shown in Tab. 4.3, and the simulated geometry is compared to the experimental data in Fig. 4.11.

Having demonstrated ALD of the investigated HfO_2, the next step in the development of thermal ALP is the establishment of an etching method. Fischer *et al.* propose thermal ALE of HfO_2 from dimethylaluminum chloride (DMAC) and HF [149], following a similar ligand-exchange reaction to that from Eqs. (4.3) and (4.4). They thoroughly investigate the necessary DMAC dosing by exploring two different reactors: Low-pressure and high-pressure. Several reactor conditions were investigated, extracting an EPC profile from TEM measurements for each experiment.

Γ_{ev} ($\text{m}^{-2}\text{s}^{-1}$)	β_0
$3.5 \cdot 10^{22}$	$7.0 \cdot 10^{-3}$

Table 4.3: Calibrated model parameters for ALD of HfO_2 for the hafnium step to experimental data from Fischer *et al.* [149].

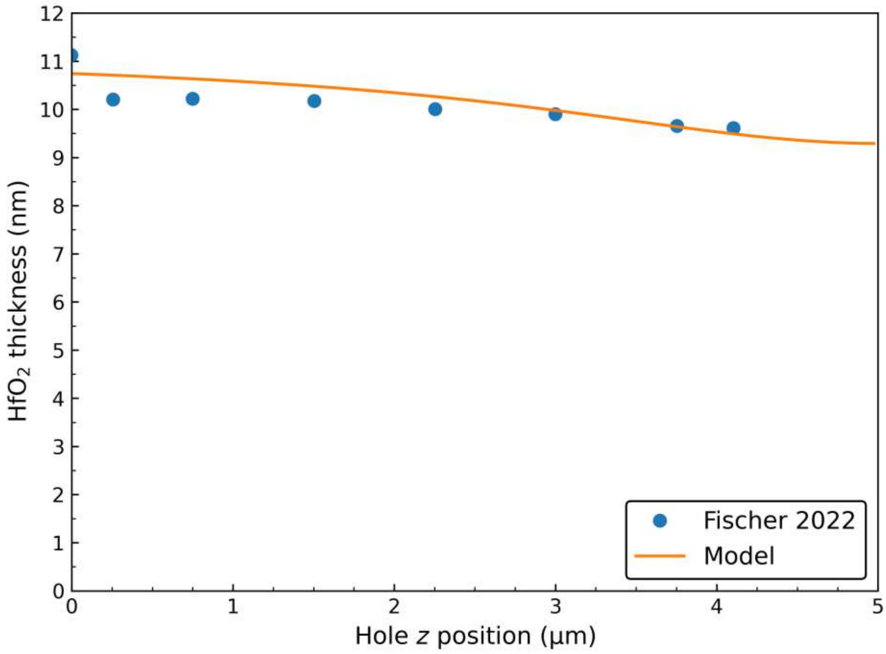

Figure 4.11: Comparison of simulated topography using parameters from Tab. 4.3 to ALD of HfO_2 in a 3D NAND-like test structure reported by Fischer *et al.* [149].

The low-pressure reactor experiments were performed at 250 °C and had no background gas for a process pressure of 30 mTorr for both the DMAC and the HF steps. Two HF dose configurations were investigated by varying the pulse time: A low dose of 5 s and a high dose of 30 s. The DMAC dose was varied by changing its pulse time between 5 s and 90 s.

The high-pressure experiments performed etching at 350 °C using N_2 as a carrier gas for a total process pressure of 1 Torr. The DMAC partial pressure was kept as 48 mTorr, thus its dose was varied by changing the pulse time between 3 s and 90 s. Two sets of experiments varying the HF dose were also performed. The low HF dose was achieved with a partial pressure of 150 mTorr for a pulse time of 2 s. The high HF dose had a partial pressure of 400 mTorr for 60 s. It was observed by the authors of the original publication that there is a decline in EPC for comparatively lower DMAC doses. They conclude that a substantially large dose is necessary to enable thermal ALE.

Nonetheless, reactive transport modeling can be used to further characterize and fine-tune this process. This is achieved by applying the model described in Section 4.2 assuming the DMAC is the limiting reactant. It has been reported that the HF dose has only a very slight impact in the EPC profile [149], therefore, it is reasonable to assume that the process is DMAC-limited. The effects of HF are captured by a global reduction in the maximum EPC which is extracted from each experiment. The simulated EPC profiles are obtained by dividing the etch depth at each z position by $N_{\text{cycles}} = 20$ and are shown in Fig. 4.12 in comparison to experimental data from Fischer *et al.* [149]. The calibrated parameters are in Tab. 4.4, including s_0.

Given the complex fluorination and ligand-exchange chemical process, s_0 cannot be calculated using the "billiard ball" approximation from Eq. (4.7). Instead, it is taken as an additional model parameter. For the high-pressure reactor, the flow is clearly not in the molecular flow regime. Thus, the Bosanquet interpolation formula is used with $d_{N_2} = 374\,\mathrm{pm}$ [109] and the DMAC radius estimated from its liquid density to be $d_{\mathrm{DMAC}} = 748\,\mathrm{pm}$.

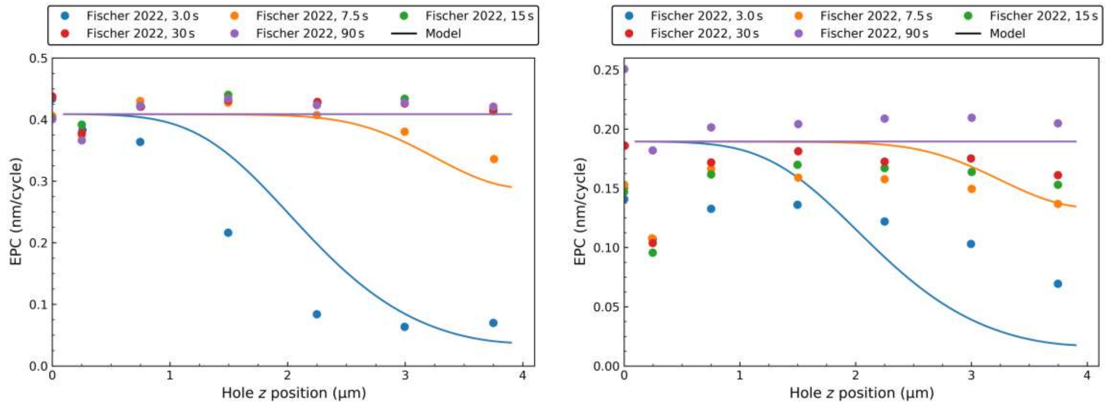

a) High pressure, high HF dose

b) High pressure, low HF dose

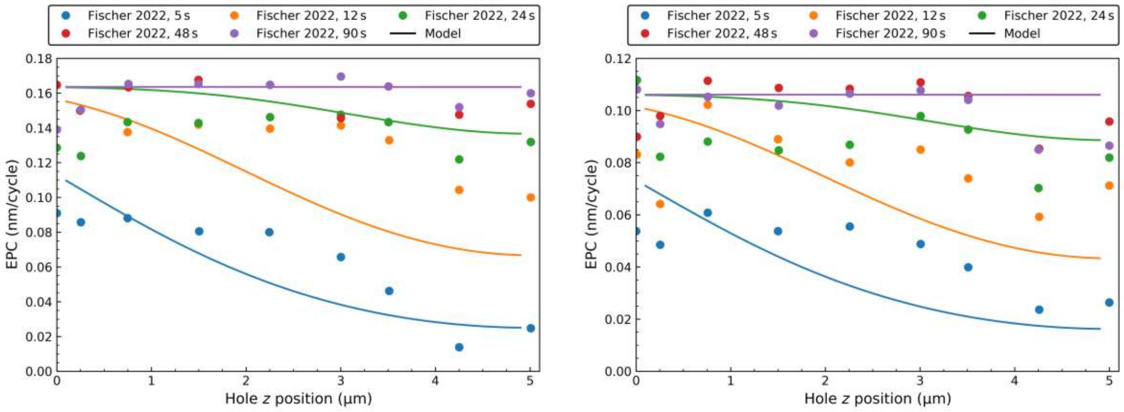

c) Low pressure, high HF dose

d) Low pressure, low HF dose

Figure 4.12: Comparison of simulated ALE using parameters from Tab. 4.4 to DMAC-limited ALE of HfO_2 in a 3D NAND-like test structure reported by Fischer *et al.* [149]. Both a low-pressure (30 mTorr) and a high-pressure (1 Torr) reactor conditions are simulated, including different doses of HF and DMAC.

Reactor condition	Γ_{ev} $(\mathrm{m}^{-2}\mathrm{s}^{-1})$	β_0	s_0 (m^{-2})
Low pressure, 250 °C	$2.5 \cdot 10^{17}$	$6.0 \cdot 10^{-4}$	$7.0 \cdot 10^{-21}$
High pressure, 350 °C	$1.0 \cdot 10^{18}$	$5.0 \cdot 10^{-3}$	

Table 4.4: Calibrated model parameters for DMAC-limited ALE of HfO_2 to experimental data from Fischer *et al.* [149].

Due to the comparatively higher noise of TEM data in comparison to the optical profilometry reported in Section 4.4, the calibrated simulations in Fig. 4.12 demonstrate only qualitative agreement. Nonetheless, the parameters reported in Tab. 4.4 already enable a preliminary analysis. They enable a first estimation of β_0 for DMAC which has not been hitherto reported. Additionally, the increase in β_0 with increasing temperature is an indication of Arrhenius-like behavior similar to Fig. 4.6. However, further experimental studies with a more detailed description of the temperature range are required to substantiate this hypothesis. Surprisingly, unlike the analysis in Section 4.4.1, the evaporation flux also appears to increase with temperature, an unexpected behavior which warrants further investigation.

Even though the obtained results are qualitative in nature, they already show a path for the investigation of device performance. The entire 3D NAND-like stack from [149] has been simulated using Silvaco's Victory Process [55], shown in Fig. 4.13. Both the ON deposition and the RIE are assumed to be ideal and are thus geometrically modeled. The thermal ALP of HfO_2 is modeled with the presented reactive transport model implemented in the Open Model Library. For the ALD step, the parameters from Tab. 4.3 are used. From the multiple reported thermal ALE conditions, the low-pressure, high HF dose, and the 12 s DMAC dose are assumed with parameters from Tab. 4.4. The simulation shows a clear tapering of the HfO_2 film thickness. Although the test structure itself is not a physically operable device, this simulation shows a path for optimization of device performance. Device engineers can, for example, use this tapering information to obtain realistic insights into the novel memory performance in the presence of non-ideal thermal ALP.

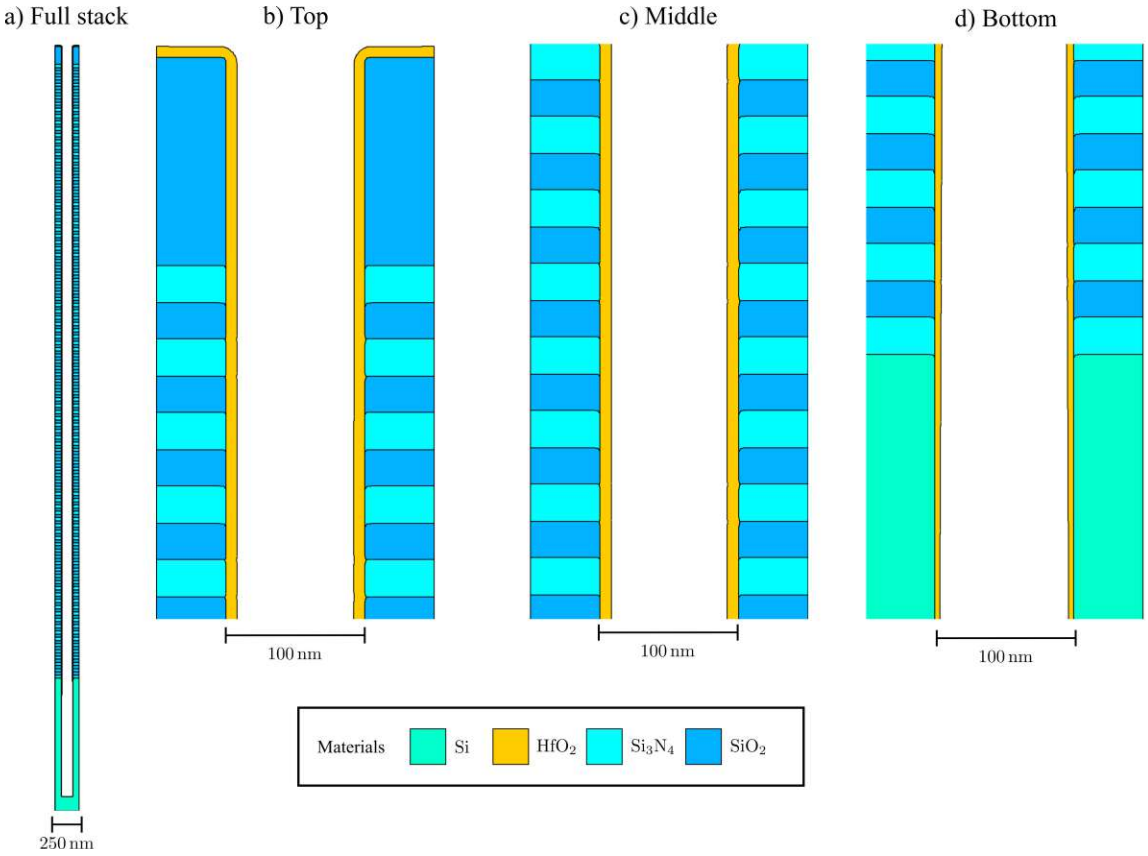

Figure 4.13: Cross-section of simulated thermal ALP of HfO_2 inside 3D NAND-like test structure [149] showing different film thickness at three different regions of the full stack (top, middle, and bottom).

Chapter 5

Modeling of Low-Bias SF_6 Plasma Etching of Si

Conventionally, plasma etching techniques exploit the presence of a plasma sheath which vertically accelerates ions, to enable high aspect ratio (AR) structures [131]. Nevertheless, there are many situations which do not involve high AR features, instead requiring isotropic or near-isotropic etching conditions. This is the case in, for example, optical devices such as microlenses [49] or microcavity resonators [168], for on-chip cooling microchannels [169], or for microelectromechanical systems (MEMS) membranes [170]. In these situations, plasma etching is still an invaluable tool as long as the electric field between the plasma and the wafer, i.e., the voltage bias, is kept low [31]. The plasma is then employed as a low-temperature source of etchants, leading to etch characteristics similar to those obtained by isotropic wet etching [171].

Low-bias plasma etching offers several advantages with respect to isotropic wet etching. Its results are usually more controllable, reproducible, and uniform [49], as well as leading to better surface cleanliness which is key for optical applications [168]. However, it is known that the shape of features resulting from low-bias plasma etching is not the same as those from ideal isotropic wet etching [171]. Therefore, the development of this technology requires a deep understanding of the mechanisms leading to non-ideal isotropy. This is particularly necessary for optical applications, where exact control over the shape is paramount.

To bridge this gap, this chapter presents a modeling study of low-bias plasma etching of silicon (Si) from the most established gas source: sulfur hexafluoride (SF_6) [45, 172]. The underlying plasma complexity is condensed into a single particle aggregating etchants with similar properties, i.e., "neutrals" [43, 134]. This work used measurements obtained from a collaboration with experimentalist colleagues from the University of Vienna and TU Wien to evaluate the reactant flux modeling approaches from Section 2.3. Having determined the most suitable approach, the reactive transport process is interpreted with respect to the involved phenomenological model and applied to experimental data reported in the literature [49, 171]. The issue of reactor loading is addressed, and several reported trenches are reproduced with the model. Finally, a phenomenological relationship between the most critical model parameter, the Si sticking coefficient, and a measurable degree of isotropy is proposed.

Own contributions: The evaluation of the flux models in the context of topography simulation of low-bias SF_6 plasma etching of Si are conducted, as well as the interpretations and analyses of these simulations. The most important analysis is the developed empirical relationship between a phenomenological parameter and experimental topographies. This work has been originally presented at the EUROSOI-ULIS 2021 conference [173] and as an invited research article [88]. The analyses stemming from the experimental collaboration has been originally published in [174] and is discussed in further detail in Chapter 6.

5.1 Low-Bias Etching of Si from SF_6 Plasma

To avoid the issues arising from wet etching, a vapor-phase, plasma-less, process can be used to obtain isotropic etch characteristics. This process has been studied since the 1960s after the synthesis of xenon difluoride (XeF_2) [175] which is the most studied etchant [170] even though other reactants such as fluorine gas (F_2) have also been investigated [176]. Their widespread adoption has been hindered by the complexity of the involved equipment and chemicals. For instance, XeF_2 reacts with water vapor and forms hydrogen fluoride (HF) [177]. The latter spontaneously etches silica (SiO_2), which is a common masking material in complementary metal-oxide-semiconductor (CMOS) processing, leading to selectivity challenges. This complexity has led to vapor-phase processes being restricted to niche applications [171].

Therefore, low-bias plasma etching processes have emerged as the main CMOS-compatible alternatives to isotropic wet etching. After the investigation of the etch characteristics of several fluorinated gases, SF_6 has emerged as the preferred process due to its inert handling characteristics and higher etch rates [172]. In fact, this anomalous high etch rate is an active field of research [45, 178], and it is thought that the sulfur atoms play an active role in catalyzing the etch reaction. However, this increased reaction probability and etch rate themselves play a role in limiting the achievable isotropy. A more efficient reaction likely increases the sticking coefficient β and, as discussed in Section 2.3.1, an ideally isotropic reaction has $\beta \to 0^+$.

Low-bias plasma etching of SF_6 then stands in a very challenging intersection of technological trade-offs. The industrially-established status of SF_6 etching technology, notably with inductively couple plasma (ICP) reactors, makes it very desirable to achieve isotropic etch characteristics. Simultaneously, the selfsame qualities which have made it an established process thwart the desired etch characteristics. Nonetheless, this process has been shown to lead to structures with desired traits, even though the etching process is not perfectly isotropic. Originally, the process was introduced for Si microlens fabrication [49], where the lower isotropy of a masked etch step is mitigated by a second, maskless, etch step. More recently, this process has been refined by controlling the roughness of the final surface [179, 180], ultimately leading to high-finesse optical microcavity resonators [168].

Nonetheless, the challenge of controlling the isotropy, and thus the precise final shape of the structure, remains. Increased attention has been placed on experimentally investigating and quantifying the isotropy in a masked etch step [171, 181]. Additional insight to this open question can be brought by accurate topography simulation, which will be discussed in the subsequent sections. To obtain physically meaningful simulations, they must be compared and calibrated to relevant experimental data. The ICP reactor setups used in the experiments are shown in Tab. 5.1.

The evaluation of the reactive transport models, discussed in Section 5.2, is done with respect to experimental data obtained from collaboration partners from the University of Vienna and TU Wien, originally described by Wachter *et al.* in [168]. This two-step (first step with a photoresist mask, second step maskless) etching process is described in more detail in Section 6.1. The remaining analyses in this chapter are performed in comparison to single-step (with photoresist) etched profiles reported by Larsen *et al.* [49] and Panduranga *et al.* [171].

Parameter	Wachter *et al.* 2019 [168]	Panduranga *et al.* 2019 [171]	Larsen *et al.* 2005 [49]
Pressure (mTorr)	-	30	10
Flow rate (sccm)	100	50	200
Coil power (kW)	2	2	3
Table power (W)	15	0	0
Chuck temperature (°C)	30	20	20

Table 5.1: Reported ICP reactor configurations of experiments to which the topography simulation is compared.

5.2 Evaluation of Flux Modeling Approaches

Previously, a feature-scale model of SF_6 etching of Si has been proposed [182]. This model achieved good agreement with experiments by including a very accurate model for the ion energy and angular distribution functions. However, this description of the angular distribution functions is more relevant for high-bias applications since it plays a key role in determining the anisotropy. Additionally, said model is strictly two-dimensional (2D), therefore unable to differentiate between trenches and cylindrical holes which, as discussed in Chapter 3, can significantly impact the final geometry.

Thus, a fully three-dimensional (3D) model is necessary. In the context of phenomenological modeling, the goal is to determine the simplest possible model which is able to satisfactorily reproduce the experimental topographies. Then, having determined the suitable phenomenological model, it is possible to interpret it with respect to the physical processes and the involved parameters. To that end, the following approaches to calculate the local fluxes, first introduced in Section 2.3, are evaluated in comparison to experimental data: Constant flux, bottom-up visibility calculation, and top-down pseudo-particle tracking.

In all cases, only a single particle is considered. However, unlike the discussion in Chapter 4, this particle is not interpreted as representing a distinct chemical species. There is still debate about the precise mechanism of etching [45], although some recent first-principle studies highlight the role of $SF_5{}^+$ and SF_n ($n \leq 6$) radicals [183]. Instead, the particle is assumed to be an aggregate of etchants with similar properties, in what is conventionally named as "neutrals" [43, 134].

For the top-down approach, constant and effective sticking coefficient β_{eff} approximation from Eq. (2.18) is assumed. Since the etching process is nearly isotropic, the resulting features do not involve high AR. Therefore, no approximate one-dimensional (1D) model is available for evaluation. For the calculation of the surface evolution, these approaches are integrated with level-set (LS) based topography simulators: Silvaco's Victory Process [55] and the open-source simulator ViennaTS [57].

The calibration and evaluation of the flux modeling approaches are done with respect to 3D optical profilometer data of etched microcavities provided by collaboration partners from the University of Vienna and TU Wien, first reported in [168]. In their experiment, multiple cavities with different initial photoresist cylindrical openings d were simultaneously etched in a two-step process under the reactor conditions reported in Tab. 5.1 under "Wachter *et al.* 2019". The first etch step was performed with the photoresist mask present for an etch time of 320 s. Afterward, the photoresist was removed using acetone. Then, a second etch step was performed for 48 min. The resulting microcavities were characterized with a white light profilometer after cleaning and polishing. The optical device, its manufacturing and subsequent analyses are presented in more detail in Chapter 6.

For the evaluation of the flux modeling approaches, three representative cavities are chosen, with d values of 12.4 µm, 34 µm, and 52 µm. That is, they are the smallest, intermediate, and largest cavities available from the 100 cavities etched on the same chip. The calibrations are performed using the normalized flux convention from Eq. (2.7), i.e., the main calibration parameters are the plane-wafer etch rate $PWR_{\text{Si/resist}}$ for each individual material and each etch step. The top-down approach has as additional parameters the material-dependent constant sticking coefficients $\beta_{\text{Si/resist}}$. For the top-down approach, the parameters are automatically calibrated with the methodology described in Section 6.2 and are shown in Tab. 5.2. To obtain the clearest possible comparison for the bottom-up and constant flux approaches, the first step PWR_{Si} is manually adjusted to obtain the best possible fit, requiring a different value for each microcavity reported in Tab. 5.3. The second step PWR_{Si} and PWR_{resist} values from Tab. 5.2 are used in all simulations. A cross-section of the simulated topographies in comparison to the profilometer data is shown in Fig. 5.1.

Implicitly, the bottom-up and constant flux approaches assume the phenomenological surface models of $\beta = 1$ and $\beta \to 0^+$, respectively, as discussed in Section 2.3. As can be seen in Tab. 5.3, these flux approaches require a different fitted value of PWR_{Si} for each d. This is an indication that the implied phenomenological surface models do not capture the underlying physical reality since, in principle, there is no physical explanation for starkly differing $PWRs$ in features on the same chip.

Parameter	Calibrated value
First etch step PWR_{Si}	$2.15\,\mu\mathrm{m\,min^{-1}}$
Second etch step PWR_{Si}	$0.66\,\mu\mathrm{m\,min^{-1}}$
PWR_{resist}	$0.21\,\mu\mathrm{m\,min^{-1}}$
β_{Si}	$7.5\,\%$
β_{resist}	$6.1\,\%$

Table 5.2: Parameters for top-down simulation of SF_6 etching of Si microcavities automatically calibrated to experimental data.

d	Constant flux, first step PWR_{Si}	Bottom-up, first step PWR_{Si}
$12.4\,\mu\mathrm{m}$	$1.45\,\mu\mathrm{m\,min^{-1}}$	$23\,\mu\mathrm{m\,min^{-1}}$
$34.0\,\mu\mathrm{m}$	$1.94\,\mu\mathrm{m\,min^{-1}}$	$6.0\,\mu\mathrm{m\,min^{-1}}$
$52.0\,\mu\mathrm{m}$	$2.09\,\mu\mathrm{m\,min^{-1}}$	$3.6\,\mu\mathrm{m\,min^{-1}}$

Table 5.3: First step plane-wafer Si etch rates PWR_{Si} for each initial photoresist opening diameter d manually calibrated to experimental data.

Instead, it is more physically sound to introduce an additional parameter, a variable β_{Si}, than relying on multiple $PWRs$. Additionally, it can be seen in Fig. 5.1 that the bottom-up model does not capture the correct local etch rates at the sidewalls, leading to the incorrect curvature. The constant flux model fails by simulating an unrealistically flat bottom, as it applies the same etch rate to all exposed surfaces. Therefore, the area below the initial opening remains perfectly flat which is not observed in the experiment.

From this analysis as well as the observation of the better fit in Fig. 5.1, it can be concluded that the top-down pseudo-particle tracking approach is the best-suited phenomenological model for low-bias SF_6 etching of Si. The necessity of different *PWRs* for each etch step is evidence of the effect of reactor loading, which is further discussed in Section 5.3. In addition, the suitability of the constant sticking approximation is a strong indication that the etching regime is transport-controlled and, thus, the surface coverage of the reactants is low, as in the discussion of Eq. (2.18). It is important to note, however, that β_{Si} is *not* identical to the clean-surface β_0, the latter being reported to be in the range between 0.57 [181] and 0.7 [45]. Instead, β_0 provides an upper bound of the possible values of β_{Si}:

$$\beta_{\mathrm{Si}} \leq \beta_0 \tag{5.1}$$

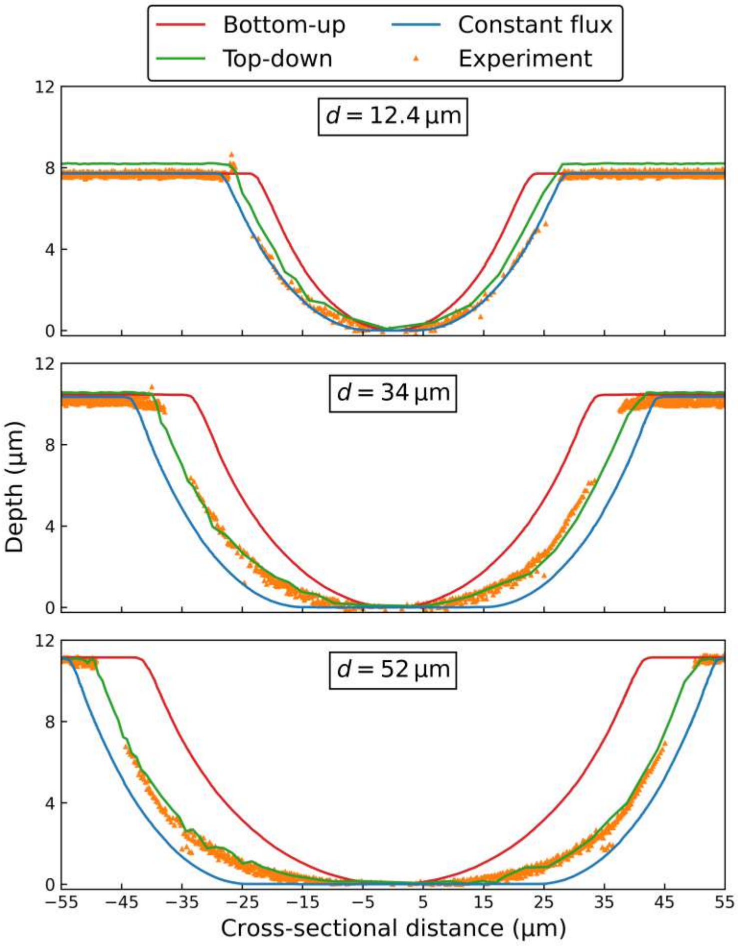

Figure 5.1: Comparison of cross-sections of simulated surfaces using the best parameters for each of flux modeling approaches to optical profilometry measurements of fabricated Si microcavities with different initial openings d. Adapted from Aguinsky *et al.*, *Solid State Electron.* 191, (2022) p. 108262. [88], © The Authors, licensed under the CC BY 4.0 License, `https://creativecommons.org/licenses/by/4.0/`.

One key strength of topography simulations is that they enable the exploration of states which are not available experimentally. The state of the microcavity with initial $d = 12.4\,\mu m$ is shown in Fig. 5.2 for the three proposed flux modeling approaches after the initial etch step but before photoresist removal. Although in principle available, this state was not experimentally recorded due to resource constraints, as it would require electron microscopy. For the top-down simulation, the parameters from Tab. 5.2 are used, while for the bottom-up and constant flux simulations the values of PWR_{Si} are adjusted to yield the same microcavity depth. This highlights the success of the top-down approach and the limitations of the others. The bottom-up approach is unable to capture the undercut which is a known experimental feature [171], leading to an unrealistically bulbous structure. Also, the perfectly flat bottom of the constant flux approach is again featured. Finally, the simulations indicate the presence of photoresist tapering, which is a direction of interest for further process optimization.

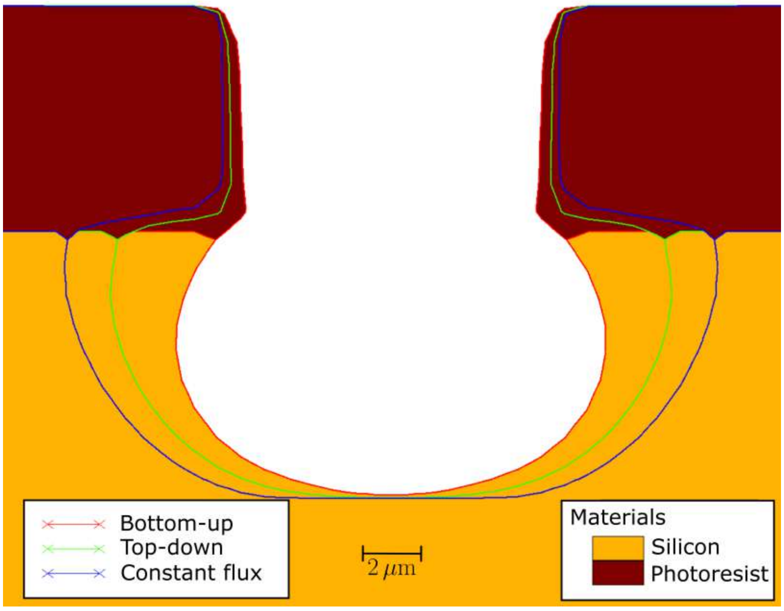

Figure 5.2: Simulated microcavity with initial photoresist opening $d = 12.4\,\mu\text{m}$ after the first etch step. Adapted from Aguinsky *et al.*, *Solid State Electron.* 191, (2022) p. 108262. [88], © The Authors, licensed under the CC BY 4.0 License, `https://creativecommons.org/licenses/by/4.0/`.

5.3 Reactor Loading Effect

As already seen in Tab. 5.2, there appears to be a reduction in the PWR_{Si} for the second etch step. This is a strong indication of the presence of the reactor loading effect, that is, a reduction in the etch rate due to an increase in the exposed wafer surface [46, 131]. With more exposed Si, which is the case for the second etch step after photoresist removal, the same number of reactants are spread across a larger area, leading to lower etch rates. This effect is different from AR dependence due to Knudsen transport, discussed in Section 3.6.1, since it does not depend on characteristics of the etched feature. The reactor loading effect, often just named "loading effect", is also distinct from microloading [184] which is a variation on etch rates due to the *local density* of features, even if the total exposed area is equal.

In principle, reactor loading can be modeled if the total exposed wafer area is known [46]. However, this information is not always accessible, and, additionally, such models still require fitting coefficients. Instead, the approach taken is to treat the $PWRs$, thus the loading effect, as a model parameter not only for each reactor condition but also for each photoresist or hardmask configuration. At the core of this approach is the approximation that the exposed area is constant *during* the etch step which is valid for low photoresist or hardmask etch rates.

This effect has been experimentally investigated by Panduranga *et al.* [171]. In their work, they attempt to deliberately construct a regime with lower etch rates by placing the individual chips over a larger and unmasked silicon carrier wafer.

They investigate two distinct situations: A low loading regime, by placing the chips directly over the stainless steel carrier plate, and a high loading regime with chips on the silicon carrier wafer. To quantify the etch depth, the chips are initially patterned with a hardmask (chromium-on-oxide) containing cylindrical holes with $d = 500\,\mu\text{m}$. Then, the etching proceeds on an ICP reactor with the conditions reported in Tab. 5.1. The final shape of the surface is measured with a mechanical profilometer.

The original authors assume that there are no limitations due to visibility, thus they calculate the $PWRs$ from the etch depths at the center. However, since visibility effects often play a subtle role, the simulation considers the entire geometry. The PWR_{Si} is manually adjusted for each of the reported regimes to encounter the best fit to the reported experimental depths. The resulting parameters are disclosed in Tab. 5.4 and the time evolution of the etch depth at the center of the cylindrical opening is shown in Fig. 5.3. The good agreement is evidence that the approach of modeling the loading effect through treating the PWR as a fitting parameter is valid. In comparison to the original work, the values are within the range of reported etch rates for the high loading regime (between 2.07 and $2.47\,\mu\text{m}\,\text{min}^{-1}$).

Low loading PWR_{Si}	High loading PWR_{Si}
$4.92\,\mu\text{m}\,\text{min}^{-1}$	$2.40\,\mu\text{m}\,\text{min}^{-1}$

Table 5.4: Plane-wafer etch rates for the low and high reactor loading regimes calibrated to experimental etch depths reported in [171].

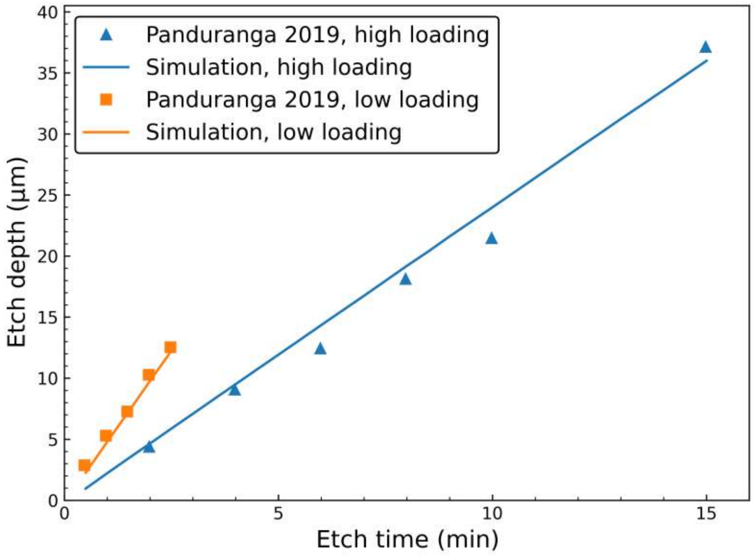

Figure 5.3: Time evolution of simulated etch depths in the low and high reactor loading regimes compared to experimental data reported by Panduranga *et al.* [171]. Adapted from Aguinsky *et al.*, *Solid State Electron.* 191, (2022) p. 108262. [88], © The Authors, licensed under the CC BY 4.0 License, `https://creativecommons.org/licenses/by/4.0/`.

5.4 Etching on Trenches

As previously indicated, 3D simulations are necessary to differentiate between cylindrical holes and rectangular trenches. Since they have the same cross-section, they are identical from the point of view of a 2D model, even though they might have substantially different particle fluxes distributions. Section 3.3 discusses this challenge in the context of Knudsen transport, highlighting that problems can arise if the mapping between trenches and cylinders is performed haphazardly. However, the top-down approach on a 3D simulation domain, shown in Section 5.2 to be the most suitable for low-bias SF$_6$ plasma etching of Si, handles this issue natively. While cylindrical holes can be directly simulated, long rectangular trenches require restricting the simulation domain to small lateral section and applying reflective boundary conditions to obtain an infinite trench.

Therefore, the same 3D top-down approach, first evaluated for a cavity with cylindrical symmetry, can be applied to etched trenches reported in the literature. In their seminal work proposing two-step low-bias SF$_6$ etching of Si in the context of microlens fabrication, Larsen *et al.* report scanning electron micrography (SEM) characterizations of multiple trenches after the first, masked, etch step [49]. These trenches were obtained using different initial photoresist openings (d) and etch times (t), as the original intent was to thoroughly describe the first etch step. The employed reactor conditions are given in Tab. 5.1. The etching on the trenches is simulated starting from an initial geometry consisting of the reported photoresist height (1.5 µm) and opening d over a Si slab of 140 µm × 40 µm and reflective boundary conditions. All trenches are simulated with the same parameter set, shown in Tab. 5.5, obtaining the cross-sectional fits in Fig. 5.4.

Figure 5.4 shows excellent agreement between the simulation and the experimental data for trenches with $t < 610\,\mathrm{s}$. The likely source of the discrepancy for larger etch times is the reported photoresist bending in those scenarios [49]. Effectively, the photoresist opening is increased by approximately 1 µm which is not captured by the simulation thus leading to a slight underestimation of the etch rates. This is supported by this discrepancy being smaller for the trench with $d = 62\,\mu\mathrm{m}$, since the effective increase in the opening is small in comparison to d. Nonetheless, the remarkable agreement for widely different trenches and etch times strongly support the top-down approach for this process.

Parameter	Calibrated value
PWR_{Si}	$7.80\,\mu\mathrm{m\,min^{-1}}$
PWR_{resist}	$0.00\,\mu\mathrm{m\,min^{-1}}$
β_{Si}	35 %
β_{resist}	6.1 %

Table 5.5: Top-down model parameters manually calibrated to etched trench SEM profiles reported by Larsen *et al.* [49].

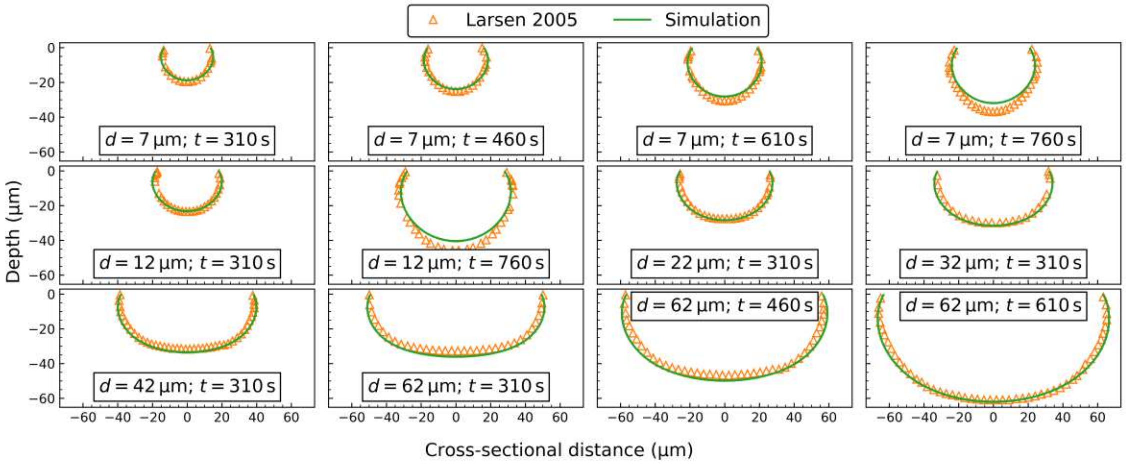

Figure 5.4: Comparison of simulated trenches to reported SEM profiles from Larsen *et al.* [49]. Trenches have different initial photoresist openings d and etch times t. Adapted from Aguinsky *et al.*, *Solid State Electron.* 191, (2022) p. 108262. [88], © The Authors, licensed under the CC BY 4.0 License, `https://creativecommons.org/licenses/by/4.0/`.

This is further supported by calibrating the simulation to trenches characteristics reported by Panduranga *et al.* [171]. Other than the different hardmask initial opening geometry, the experimental configuration is the same as that reported for the high loading regime in Section 5.3 and Tab. 5.1. The simulations are performed using the same parameter set for all reported trenches with different initial hardmask openings d. The hardmask height (0.39 µm) is considered, as well as reflective boundary conditions to capture an infinite trench geometry.

The parameters are manually calibrated to the reported values of two geometric quantities of interest — the undercut H and the etch depth V— for different etch times [171] and are stated in Tab. 5.6. As an illustration, a comparison between a simulated geometry and a SEM image is shown in Fig. 5.5 for the trench with $d = 8\,\mu m$, including a representation of H and V. The time evolution of these geometrical quantities during etching is shown in Fig. 5.6. Due to the use of a mechanical stylus profilometer in the measurement of the undercut, there is substantial noise in the reported values. This leads to challenges in the calibration procedure which instead focuses on the etch depth and describes the evolution of the undercut qualitatively.

Parameter	Calibrated value
PWR_{Si}	$2.40\,\mu m\,min^{-1}$
PWR_{hardmask}	$0.00\,\mu m\,min^{-1}$
β_{Si}	50 %
$\beta_{\mathrm{hardmask}}$	5 %

Table 5.6: Top-down model parameters calibrated to experimental trench undercut and etch depth reported by Panduranga *et al.* [171].

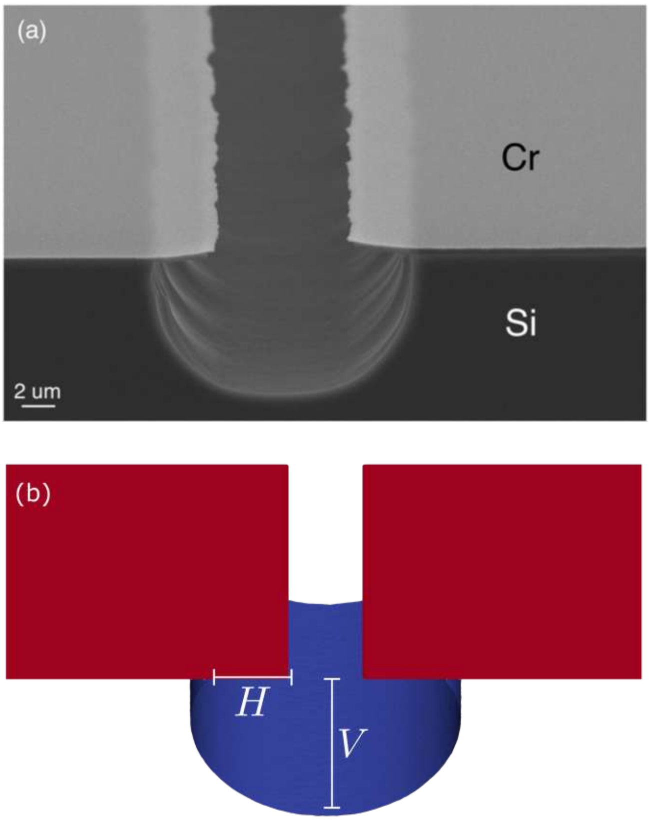

Figure 5.5: a) SEM image of etched trench with initial hardmask opening $d = 8\,\mu\text{m}$. Reprinted with permission from Panduranga *et al.*, *J. Vac. Sci. Technol. B* 37, (2019) p. 021302. [171], © American Vacuum Society. b) Simulation of the same trench showing two geometric quantities of interest: The undercut H and the etch depth V. Adapted from Aguinsky *et al.*, *Solid State Electron.* 191, (2022) p. 108262. [88], © The Authors, licensed under the CC BY 4.0 License, `https://creativecommons.org/licenses/by/4.0/`.

In summary, the good agreement shown in Figs. 5.4 to 5.6 is strong evidence of the suitability of the top-down approach. Only two parameters are required per material and etch step to achieve this agreement even for different geometries and etch times: The PWR and β_{eff}. The former can be initially estimated from the etch depths of large features and usually falls in known ranges [185, 186]. However, as discussed in Section 5.3, attention must be placed to correctly consider the reactor loading effect. It is in the sticking coefficient that the particularities of each reactor configuration express themselves, since substantially different values are reported in Tabs. 5.2, 5.5, and 5.6. Nonetheless, this quantity is fixed for *each* reactor condition. This is supported by recent experimental studies which connect β_{Si} and related quantities, like the reaction probability, to plasma properties. Most notably, β_{Si} appears to be strongly connected the fluorine radical density but has only minor variations with temperature [45, 181]. Therefore, the sticking coefficient can be taken as a phenomenological proxy of the reactor setup.

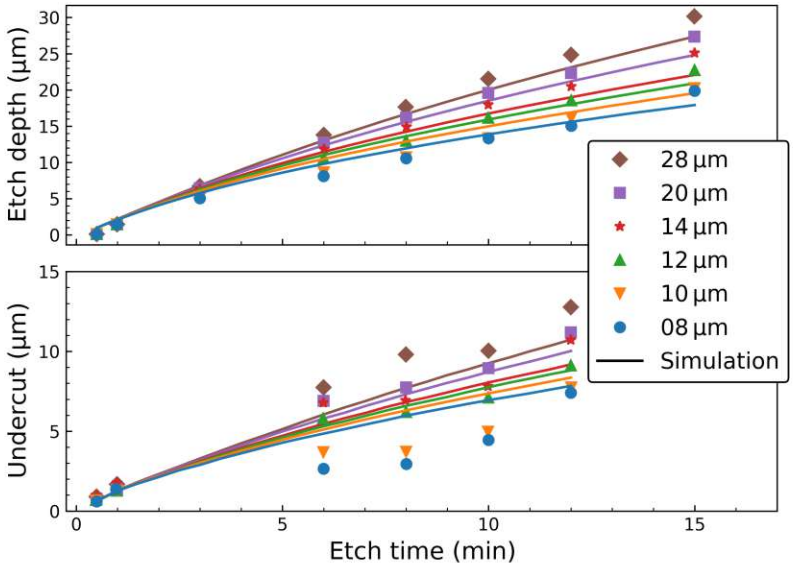

Figure 5.6: Time evolution of simulated trench undercut and etch depth compared to experimental data reported by Panduranga *et al.* [171]. Adapted from Aguinsky *et al., Solid State Electron.* 191, (2022) p. 108262. [88], © The Authors, licensed under the CC BY 4.0 License, `https://creativecommons.org/licenses/by/4.0/`.

5.5 Relationship between Degree of Isotropy and Sticking Coefficient

As discussed in Section 5.4, the phenomenological parameters are remarkably representative of the reactor conditions. From all parameters in the context of low-bias SF_6 etching of Si, the most crucial is the constant effective sticking coefficient of the fluorine reactant on silicon (β_{Si}). Therefore, it is important to investigate how this parameter relates to experimentally-accessible geometric quantities of interest of etched features. If such a relationship can be clearly established, an "inverse modeling" connection can be obtained: Given experimental measurements of features, the model parameters can be estimated. Thus, information about the surface chemistry can be inferred from the experimental topography.

To that end, it is necessary to define an empirically-accessible metric which can then be linked to β_{Si}. Based on the undercut H and the etch depth V shown in Fig. 5.5.b), the degree of isotropy I can be defined as [171]:

$$I = \frac{H}{V} \tag{5.2}$$

The definition in Eq. (5.2) is analogous to the step coverage defined for atomic layer deposition (ALD) in Section 4.4. Fundamentally, the concept of isotropy in etching is equivalent to conformality in deposition [129]. An ideally isotropic etching process leads to I=1, while a perfectly vertical process, like the one presented in Section 3.6.1, leads to I=0. In several cases, however, an intermediate value of I is required.

This is often the case in, e.g., laser cavity and other optical applications. As shown in Figs. 5.1 and 5.2, an ideally isotropic process leads to a perfectly flat region below the original opening, which is an undesirable feature for optical applications [187].

For the exploration of the relationship between β_{Si} and I, several topography simulations are performed. The experimental setup from Panduranga *et al.* [171] is considered for a trench with $d = 12\,\mu\mathrm{m}$. All parameters except for β_{Si} are thus taken from the calibrated values in Tab. 5.6. As it is considered a proxy for alternative reactor conditions, β_{Si} is varied between 1 % and 100 %. For each value of β_{Si}, the etch is performed for 1 h and the degree of isotropy is extracted every 30 s. Therefore, reactors with different loading conditions and *PWRs* can also be captured by adjusting the timescale. This analysis is plotted in Fig. 5.7, additionally including the contour map of I for a different trench with $d = 60\,\mu\mathrm{m}$.

From comparing the I contour lines from the trenches with 12 µm and 60 µm openings in Fig. 5.7, it can be noted that there is only a very limited impact of varying d. Similar remarks are made in the original publication [171]. Additionally, the etch time does not appear to impact the degree isotropy after a certain saturation period. Therefore, it can be concluded that I is fundamentally a function of β_{Si} and, subsequently, defined by the reactor condition.

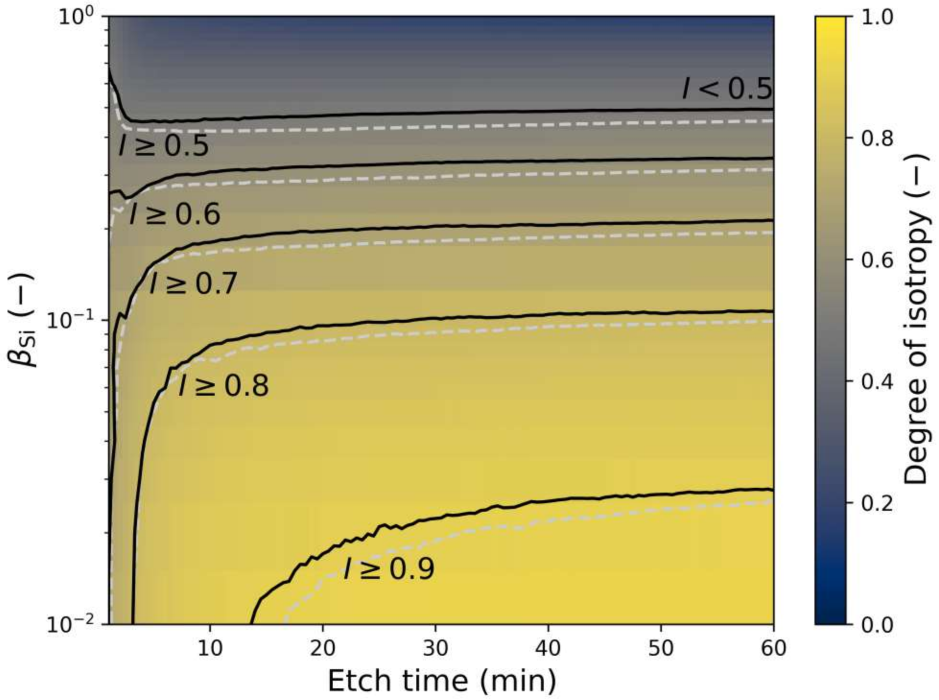

Figure 5.7: Heat map of the simulated degree of isotropy (I) as a function of the sticking coefficient β_{Si} and etch time for a trench with $d = 12\,\mu\mathrm{m}$. The simulation parameters are taken from Tab. 5.6. The gray dashed line shows the I contour lines for a trench with $d = 60\,\mu\mathrm{m}$. Adapted from Aguinsky *et al.*, *Solid State Electron.* 191, (2022) p. 108262. [88], © The Authors, licensed under the CC BY 4.0 License, `https://creativecommons.org/licenses/by/4.0/`.

An empirical relationship can now be constructed between I and β_{Si}. This is done by fixing the etch times to 5, 10, and 50 min in Fig. 5.7. This relationship, shown in Fig. 5.8, is the sought inverse connection between experimental topographies and the model parameters. Since the degree of isotropy is an empirically measurable property, its value can be used in Fig. 5.8 to provide an estimate of the sticking coefficient. This is not only useful as a starting point for calibrations of topography simulations, but also enables process developers to make inferences about the state of the reactor from topography measurements.

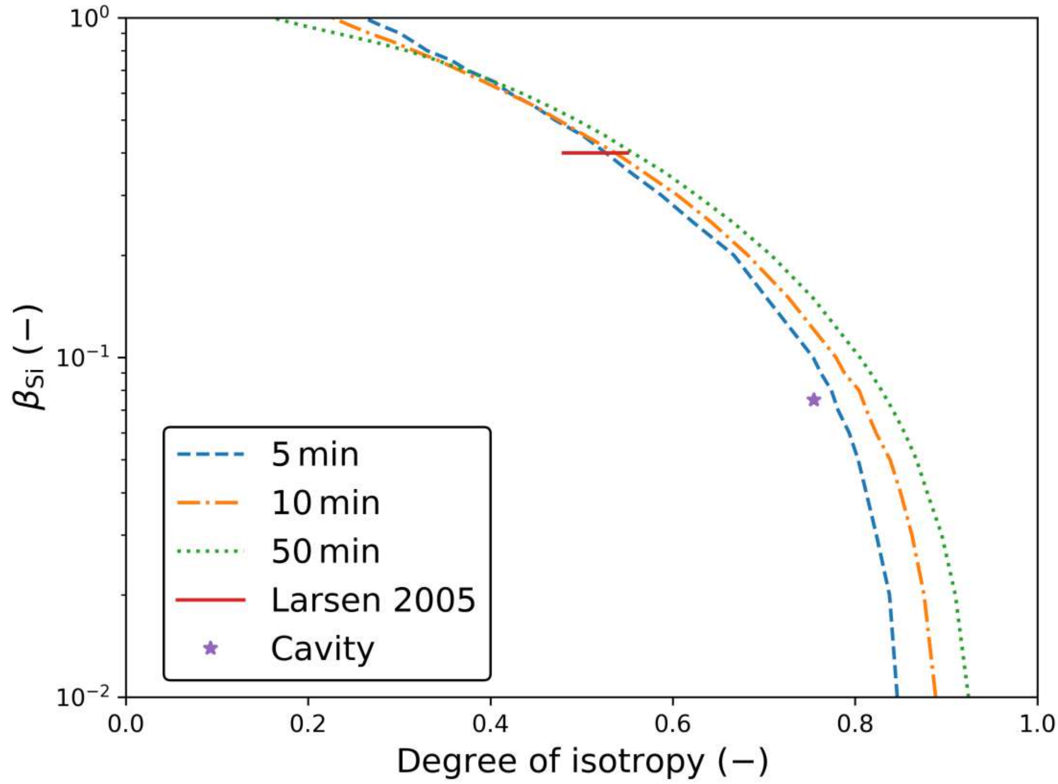

Figure 5.8: Empirical relationship between the degree of isotropy I and silicon sticking coefficient β_{Si} for multiple etch times. The line marked "Larsen 2005" shows the range of values of I extracted from the reported profiles [49] and the calibrated β_{Si} from Tab. 5.5. The point label "Cavity" denotes the value of I after the first etch step and calibrated β_{Si} for the cavity presented in Section 5.2. Adapted from Aguinsky *et al.*, *Solid State Electron.* 191, (2022) p. 108262. [88], © The Authors, licensed under the CC BY 4.0 License, `https://creativecommons.org/licenses/by/4.0/`.

The empirical relationship in Fig. 5.8 is further examined by applying it to situations with different reactor configurations and feature geometries, that is, the other experiments and calibrations presented in this chapter. The line marked "Larsen 2005" shows the range of I extracted from the reported SEM profiles [49] as well as the manually calibrated β_{Si} from Tab. 5.5. The wide range of I is partly due to the previously discussed photoresist bending phenomenon. In addition, the cavities presented in Section 5.2 have their values of β_{Si} and I after the first etch step presented with the label "Cavity". In both of these situations, good agreement is shown between the calibrated values and those expected from the empirical relationship. For the etched cavities, the somewhat larger deviation is in part explained by the fact that the geometries are different. Specifically, they are holes with cylindrical symmetry which are not entirely equivalent to long trenches, as discussed in Section 3.3.

Nevertheless, this examination shows that the empirical relationship shown in Fig. 5.8 is powerful and complementary to automatic calibration processes. It can also be applied to fine-tune etching processes by interpreting β_{Si} as a proxy variable to the reaction probability of fluorine radicals with silicon. Recent studies have shown that the reaction rates decrease with an increase of plasma flux of fluorine radicals $\Gamma_{\mathrm{source,F}}$ [45, 181]. For example, if the measured degree of isotropy is too low for a certain application, a process developer should consider adjusting the process in order to increase $\Gamma_{\mathrm{source,F}}$ and thus reduce β_{Si}. To further optimize this process, the development of an explicit mapping between $\Gamma_{\mathrm{source,F}}$ and I through experimentally-grounded topography simulation is an appealing area of future research.

Chapter 6

Optimization of Silicon Microcavity Resonators

The final technical chapter of this thesis focuses on an application of topography simulation to the optimization of a fabrication process. As previously discussed in Chapter 5, the top-down single-particle flux modeling approach with constant sticking coefficient β_{eff} is adequate for low-bias sulfur hexafluoride (SF_6) plasma etching of silicon (Si). Therefore, attention can now be placed on the optimization of an actual device component manufactured using this process: Silicon microcavity resonators. These components are under active investigation by experimental collaboration partners at the University of Vienna and TU Wien [168, 188], and they can be further optimized by achieving a higher degree of control of the microcavity shape.

Optical resonators are a fundamental component of modern light-based devices with diverse applications [189]. The resonator quality strongly depends on the exact shape of the involved microcavities [187]. Therefore, their optimization requires achieving fine control over the geometry which subsequently involves a large effort in understanding their manufacturing. Conventionally, microcavities are manufactured in Si wafers using isotropic wet etching [190, 191]. More recently, low-bias SF_6 plasma etching has been introduced as an alternative to this method due to its improved controllability, uniformity, and reproducibility [49]. Even though many advances have been made to reduce surface roughness [180] and improve mirror alignment [168], the challenge of precisely controlling the shape of the cavity still remains.

Topography simulation is an invaluable tool to tackle the issue of shape control. It is able to not only precisely reproduce the experimental geometries, but also enables a detailed investigation of alternative process recipes without having to perform multiple costly experiments. This chapter presents a simulation-driven optimization of the process parameters, namely the etch times, based on a robust calibration procedure. First, the fabrication and characterization of the experimental microcavity, performed by the collaboration partners, is briefly reviewed. Then, a robust novel calibration procedure is discussed, with particular focus on the critical feature detection algorithm. Finally, having obtained a calibrated simulation, the extraction and optimization of the microcavity parameters is presented.

Own contributions: The development of the custom feature detection algorithm, its integration with an automatic calibration procedure, and also the computational study of the optimization of optical and process parameters are novel contributions. These results have been originally published as a journal article [174].

6.1 Silicon Microcavity Resonators

Optical resonators are invaluable components with applications in diverse fields of science and technology. They enable a strong coupling between matter and light, thus finding use in, e.g., laser physics [192, 193], spectroscopy [194, 195], and in fundamental quantum science [196, 197]. There are several mirror configurations which enable optical resonators [168, 187], but in general they involve at least one cavity. For instance, a plano-concave (PC) resonator requires one cavity and one plane mirror, while a concave-concave (CC) configuration requires two cavities. In all cases, a very precise control of the shapes of the cavities is crucial, since geometric quantities, such as the radius of curvature (ROC), directly impact the quality metrics of the resonator [187].

Advanced micro- and nanomachining techniques of Si lend themselves to the development of very high quality optical resonators based on silicon microcavities. Since the desired structures have spherical or parabolic shapes, i.e., broadly isotropic shapes, the initial research efforts were driven by conventional isotropic wet etching of Si [190, 191]. However, as discussed in Chapter 5, low-bias plasma etching using SF_6 gas can have several advantages regarding controllability, reproducibility, and uniformity [49]. In addition, as shown in Section 5.2, an ideally isotropic process can lead to perfectly flat regions which are detrimental to optical device performance, since in this case the ROC is infinite.

A two-step low-bias inductively couple plasma (ICP) etching of Si has thus been proposed by Larsen *et al.* as a dry alternative to wet etching configurations for silicon microlens mold fabrication [49]. This fabrication process is illustrated in Fig. 6.1. After cylindrical openings are lithographically patterned on the photoresist, a first etch step is performed. The photoresist is then removed, and a second etch step is executed. This second maskless step is proposed to improve the quality of the final structure, a claim which is evaluated in Section 6.4. One significant trade-off of this approach is the increase in surface roughness [179] which is typical of dry etching processes. However, this roughness can be mitigated by a series of oxidation and oxide removal steps [180]. Additionally, SF_6 etching enables the use of deep reactive ion etching (DRIE) techniques to create alignment structures which are crucial to enable high quality CC resonators [168].

This two-step etching process is employed by the experimental collaboration partners from the University of Vienna and TU Wien, first described by Wachter *et al.* in [168]. A moderately doped, n-type Si(100) wafer is used as a substrate. Three layers of AZ6624 photoresist are added to achieve a masking layer thickness of 9 µm.

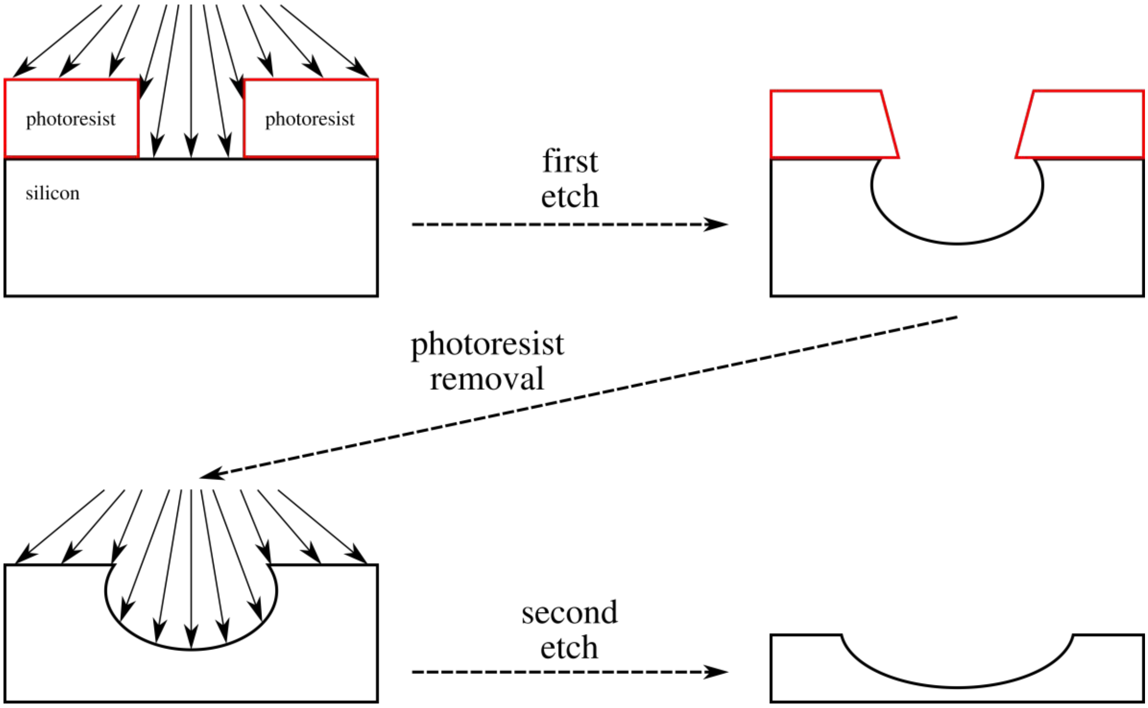

Figure 6.1: Illustration of the two etch steps of the fabrication process of Si microcavities. Adapted from Aguinsky *et al.*, *J. Micromech. Microeng.* 31, (2021) p. 125003. [174], © The Authors, licensed under the CC BY 4.0 License, `https://creativecommons.org/licenses/by/4.0/`.

The resist is then lithographically patterned with an array of 100 cylindrical holes with diameters d homogeneously increasing between 12.4 µm and 52 µm. Both etch steps are performed in the same ICP reactor using SF_6 gas at a flow rate of 100 sccm, a coil power of 2 kW, and a table power of 15 W. The first etch step is performed for 320 s, and the second is performed for 48 min. Between the etch steps, the photoresist is completely striped using acetone. A polishing step, consisting of wet oxidation of Si to a thickness of 2 µm followed by oxide removal using a solution of hydrogen fluoride (HF), is performed twice.

From the 100 fabricated microcavities, three representative initial diameters are selected for analysis: The smallest (12.4 µm), the largest (52 µm), and an intermediate value (34 µm). After the polishing procedure, their topographies are measured using a white light profilometer. Since there are steep angles near the edges, there is some lost information due to reflection. To partially recover this information, an additional tilted profilometer measurement is performed. All of these measurements are realized by the collaboration partners.

Then, these measurements were processed and tilt-corrected using the open-source tool Gwyddion [198]. Both profilometer measurements are combined into a single coordinate list for each microcavity after matching the cavity centers to the same (x, y) position. In order to reproduce these measurements and to explore the process parameter space, topography simulations using the level-set (LS) method are performed.

This physical simulation focuses on the most important aspects of the fabrication processes, namely the two etch steps. The simulation assumes as the starting point an ideal lithography process, illustrated in Fig. 6.2.a). The etch steps are both physically modeled with the top-down flux modeling approach, described in Section 2.3.3 and evaluated in Section 5.2, while the photoresist removal is assumed to be ideal and, thus, performed geometrically. The final state of the surface after both etch steps is shown in Fig. 6.2.b).

The topography simulation attempts to follow the physical process as closely as possible. The initial state of the geometry is a photoresist including an ideal cylindrical hole and a thickness of 9 µm placed on top of a 160 µm × 160 µm slab of Si. The etch times are taken directly from the experimental data. Since the mask removal step is assumed to be ideal, after the first etch step the photoresist is geometrically removed. Any noise present in the simulation is strictly numerical due to the finite number of Monte Carlo samples and does not represent the physical surface roughness. The slight additional etching resulting from oxidation and oxide removal in the polishing procedure is captured by artificially increasing the etch rate for the second etch step. The simulations are performed using the topography simulator ViennaTS [57]. At the end of a simulation run, the LS surface is converted to a triangle mesh using the VTK format [199] which is then used for calibration and parameter analyses presented in the following sections.

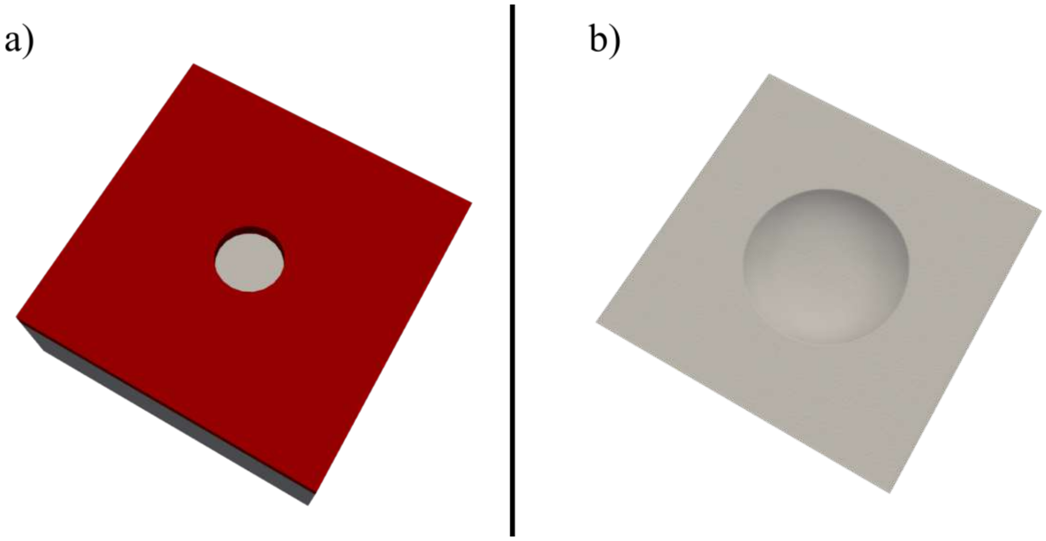

Figure 6.2: a) Initial state of the simulation domain including patterned photoresist. b) Final state of the simulation after two etch steps. Adapted from Aguinsky *et al.*, *J. Micromech. Microeng.* 31, (2021) p. 125003. [174], © The Authors, licensed under the CC BY 4.0 License, `https://creativecommons.org/licenses/by/4.0/`.

6.2 Automatic Calibration and Feature Detection Algorithm

As already evaluated in Section 5.2, the best-suited flux modeling approach is the top-down pseudo-particle tracking from Section 2.3.3 using constant and effective sticking coefficient (β_{eff}). The normalized flux convention from Eqs. (2.7) and (2.8) is applied, therefore, there are two key parameters per involved material: the plane-wafer etch rate (PWR) and β_{eff}. As seen in Fig. 6.1, the materials involved in the etching process are Si and the photoresist (res). Additionally, as discussed in Section 5.3, the reactor loading effect might play a role after the removal of the photoresist, thus the PWR_{Si} can take different values for each etch step. In summary, there are five model parameters: β_{Si}, β_{res}, PWR_{res}, the first etch step PWR_{Si}, and the second step PWR_{Si}.

Some of these parameters, most notably the second etch step PWR_{Si} and PWR_{res}, are in principle experimentally accessible. However, their values were not recorded, therefore, all five parameters must be calibrated to the experimental topographies. This number of free parameters is relatively high, as the only experimental data are the state of the cavities at the end of processing. Therefore, a robust calibration procedure is required to extract physically meaningful parameters values. In particular, the challenge of comparing disparate geometrical data — the simulated topography and the profilometer data — must be addressed. The algorithm which achieves this calibration is represented in Fig. 6.3.

The role of the topography simulator, which ingests the parameters and produces a simulated mirror microcavity, is shown in Fig. 6.3.a) through c). However, as discussed in Section 6.1, the simulated microcavity is outputted as a triangle mesh, while the experimentally characterized microcavity is described by a coordinate list. Furthermore, the coordinate systems used by both representations is not the same. Therefore, to meaningfully compare both surfaces and evaluate if the parameters are correct, feature detection is required. At the heart of the custom developed feature detection algorithm is the circular Hough transform [200], implemented in the OpenCV library [201]. This method is used to determine the center of the cavity and its maximum opening diameter O, therefore, delimiting the area of interest. It is very robust, being able to operate on incomplete experimental data, shown in Fig. 6.4.

Having extracted not only the value O of the microcavity opening but also the position of its center, the indeterminacy of the coordinate systems is resolved, since they can be matched at the microcavity minima. Therefore, the microcavity maximum depth h is also determined. To further simplify the structures in the presence of radial symmetry, all the data points are projected into their radial coordinate, thus reducing the data set from a three-dimensional (3D) to a two-dimensional (2D) problem. This is done instead of a simple cross-section to maximize the use of the experimental data, as the tilted profilometry measurement is not available for the entire microcavity. A functional description of the microcavity shape is then extracted via a sixth-order polynomial fit $\text{poly}(x)$ over this 2D data set. Figure 6.3.e) summarizes the outputs of the feature detection procedure: The maximum opening O, the maximum depth h, and the polynomial shape representation $\text{poly}(x)$.

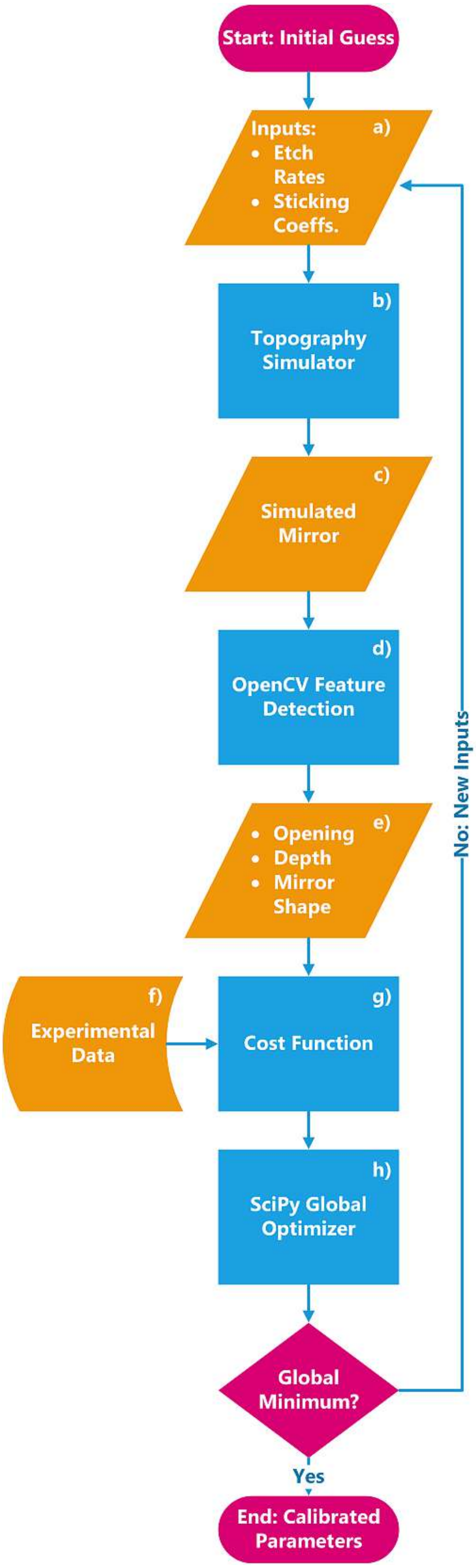

Figure 6.3: Flowchart representation of the automatic parameter calibration algorithm. Reprinted from Aguinsky *et al.*, *J. Micromech. Microeng.* 31, (2021) p. 125003. [174], © The Authors, licensed under the CC BY 4.0 License, `https://creativecommons.org/licenses/by/4.0/`.

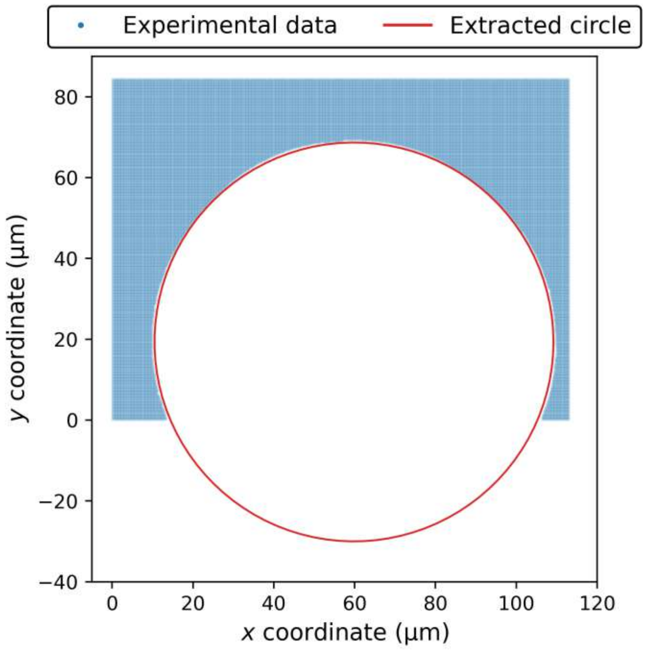

Figure 6.4: Microcavity opening extraction using the circular Hough transform on incomplete experimental data. The microcavity has been removed in a preprocessing step, therefore, the experimental data shows only the flat regions.

These outputs are by themselves not sufficient for the calibration algorithm. They must be combined into a *cost function* which is minimized during the calibration procedure, shown in Fig. 6.3.g). It is defined as the Euclidean norm of a vector of residuals which is itself constructed for each microcavity to be evaluated as

$$\begin{pmatrix} |h_{\text{exp}} - h_{\text{sim}}| \\ \frac{1}{N_x} \sum_x |\text{poly}_{\text{exp}}(x) - \text{poly}_{\text{sim}}(x)| \end{pmatrix}, \tag{6.1}$$

where N_x is the number of samples of x taken homogeneously from the region delimited by the microcavity opening O, and the subscripts exp and sim refer to experimental and simulation data, respectively. The opening O is not considered directly since it is already implicitly taken into account by the entry involving $\text{poly}(x)$. As this calibration procedure can be simultaneously performed on m multiple microcavities, the total vector of residuals has $2m$ entries.

The determination of the minimum of the cost function and, thus, the calibrated parameters, is performed with a global optimizer from the SciPy library [202], shown in Fig. 6.3.h). From the multiple available global optimizers, the generalized simulated annealing (GSA) algorithm is used [203]. Since the top-down pseudo-particle tracking is a Monte Carlo method, the simulated surfaces possess some noise which can propagate to the evaluated cost function. Therefore, local explorations of the parameter space should be avoided, as differences in Monte Carlo noise between similar simulations might lead to a fruitless search. The GSA algorithm, being stochastic in nature, performing comparatively large jumps in parameters, and not conducting local searches, is the most suited algorithm from those available within SciPy.

The calibration is performed over $m = 3$ experimental microcavities with initial photoresist opening diameters of 12.4 µm, 34 µm, and 52 µm. The simulation domain is 160 µm × 160 µm with a grid spacing $\Delta x = 0.5$ µm. Reflective boundary conditions are used. Approximately 6.1 million pseudo-particles are used per LS advection time step, that is, 120 pseudo-particles per source plane grid point. The calibration procedure is performed on a dual-socket compute node equipped with dual Intel Xeon Gold 6248 processors, for a total of 40 physical computing cores. Since each cavity can be simulated independently, each simulation is assigned 13 threads to homogeneously distribute the workload, since the topography simulation in Fig. 6.3.b) is the most resource-intensive operation. The remaining steps are single-threaded. Although the precise runtime varies greatly depending on the parameter bounds, a typical GSA run requires approximately 60 h to converge to an optimized set of parameters.

After successfully applying the GSA algorithm, a comparison of the simulated surfaces using the calibrated parameters to the experimental data is shown in Fig. 6.5, showing excellent agreement. The automatically calibrated parameters are shown in Tab. 6.1. The calibrated values of $PWR_{\mathrm{Si/res}}$ and $\beta_{\mathrm{Si/res}}$ are consistent with those reported in the literature [45, 171, 185, 186]. The reduction in PWR_{Si} of approximately 70 % in the second etch step is a consequence of the reactor loading effect, as discussed in Section 5.3, and is consistent with other reported experiments [46, 131, 204]. The ratio of the first step PWR_{Si} to PWR_{res}, that is, the observed photoresist selectivity of approximately 10 to 1, is in line with reported data from the literature [186, 205, 206]. This is remarkable evidence that the automatic calibration procedure is very effective, as it can obtain physically meaningful parameters even without direct measurements.

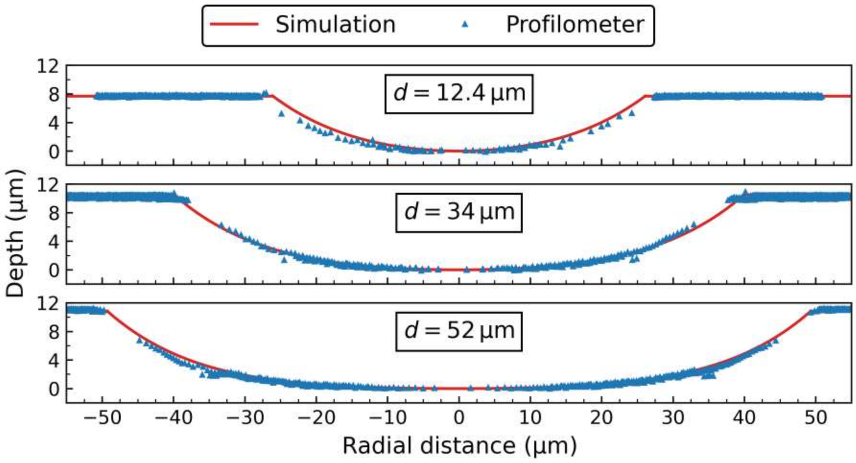

Figure 6.5: Comparison of calibrated simulation results to experimental profilometry data for microcavities with different initial photoresist openings d. The entire 3D geometry is considered by projecting into the radial coordinate. Adapted from Aguinsky *et al., J. Micromech. Microeng.* 31, (2021) p. 125003. [174], © The Authors, licensed under the CC BY 4.0 License, `https://creativecommons.org/licenses/by/4.0/`.

Parameter	Calibrated value
First etch step PWR_{Si}	$2.15\,\mu\mathrm{m\,min}^{-1}$
Second etch step PWR_{Si}	$0.66\,\mu\mathrm{m\,min}^{-1}$
PWR_{res}	$0.21\,\mu\mathrm{m\,min}^{-1}$
β_{Si}	$7.5\,\%$
β_{res}	$6.1\,\%$
Cost function	$0.367\,\mu\mathrm{m}$

Table 6.1: Model parameters obtained using automatic calibration

6.3 Optical Parameter Extraction

The feature detection procedure described in Section 6.2 is sufficient for determining a thorough description of a single cavity. However, to understand the impact of the quality of the microcavity on the assembled resonator, the entire device must be considered. Through Gaussian beam analysis of an assembled resonator [187], optical parameters can be extracted in a rough approximation of a device simulation, as they are representative of possible device performance. For simplicity, a PC resonator is considered, which is shown in Fig. 6.6 together with the extraction procedure of such parameters.

The starting point of the optical parameter extraction procedure is the feature detection algorithm, first presented in Section 6.2. Having obtained the maximum cavity opening O and having projected the data onto the radial coordinate, a representative ROC is extracted by fitting a parabola $y = ax^2 + c$ to the central $50\,\%$ of the maximum opening. This restriction is necessary to have an accurate parabolic fit, since the shape might deviate from an ideal parabola if the entire cavity is considered. Thus, the estimate of the ROC is given by:

$$ROC = \frac{1}{2|a|} \tag{6.2}$$

With the ROC having been determined, the next step is the extraction of the Gaussian beam waist size w_M. In a PC resonator, the expression for w_M at the concave mirror is [187]

$$w_M = \sqrt{\frac{\lambda}{\pi}\sqrt{\frac{L \times (ROC)}{1 - \frac{L}{ROC}}}}\,, \tag{6.3}$$

where L is the resonator length and λ is the light wavelength applied to the resonator. From further infrared laser analysis of assembled resonators [168], the relevant wavelength is $1.55\,\mu\mathrm{m}$ and L has a fixed ratio to the ROC, i.e., $L/(ROC) = 0.75$.

The waist w_M has the Gaussian interpretation of being one standard deviation σ of the beam intensity relative to its center of symmetry. Therefore, a region of interest where the majority of the beam can be found can be defined as $6w_M$, which is equivalent to 3σ. This represents an active resonator area large enough such that the maximum achievable finesse (a measure of resonator losses) is larger than 10^7 [189, 207].

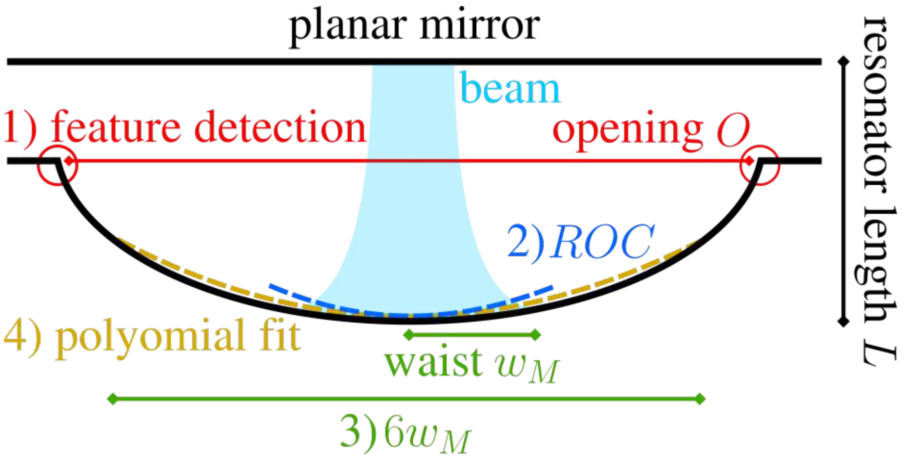

Figure 6.6: Illustration of procedure to extract optical parameters from simulated microcavities in a PC resonator configuration. 1) The feature detection algorithm from Section 6.2 is employed do determine the cavity opening O. 2) The radius of curvature (ROC) is extracted. 3) The Gaussian beam waist w_M and 4) the polynomial description of the cavity are determined. Adapted from Aguinsky *et al.*, *J. Micromech. Microeng.* 31, (2021) p. 125003. [174], © The Authors, licensed under the CC BY 4.0 License, `https://creativecommons.org/licenses/by/4.0/`.

Now, a functional polynomial description of the resonator can again be extracted. However, in contrast to the polynomial description of Section 6.2 where the entire microcavity is considered, the sixth-order even polynomial fit is restricted to the region inside the smallest of either O or $6w_M$.

With these parameters available, attention must now be placed on interpreting them in order to optimize the quality of the resonators. As previously indicated, to achieve a finesse above the state of the art [168], the resonator must be able to capture the majority of the beam. Thus, the first design criterion is having an opening large enough to capture three standard deviations of the beam intensity, i.e., $O > 6w_M$.

The second criterion comes from the insight that the best resonator performance is obtained from a parabolic cavity shape. Since the shapes have been functionally described via sixth-order polynomial of the form $a_2x^2 + a_4x^4 + a_6x^6$, the same fits can be used to quantify how closely the shape resembles a parabola. That is, the polynomial fit is taken as a measure of the deviation of the profile from an ideal parabola. This is done through the following measure of parabolicity P:

$$P = \frac{|a_2|}{\sqrt{a_2^2 + a_4^2 + a_6^2}} \tag{6.4}$$

Therefore, a measure of *parabolicity error* can be defined as:

$$\epsilon_P = 1 - P \tag{6.5}$$

Although ϵ_P is identically 0 for an ideally parabolic structure, it is more useful to analyze it in terms of a maximum error threshold. A maximum parabolicity error of 10^{-6} suffices for resonators with finesse larger than 10^6 [207].

Finally, a resonator must be as compact as possible, such that the beams become concentrated and the likelihood of spurious interactions is reduced. This is achieved through a cavity which is not only highly parabolic but which is also characterized by a sharp parabola. Alternatively, this can be interpreted through Eq. (6.2) as minimizing the *ROC*. Therefore, the three optimization design criteria are, in summary:

$$\begin{cases} O > 6w_M, \\ \epsilon_P < 10^{-6}, \text{ and} \\ \min(ROC). \end{cases} \tag{6.6}$$

6.4 Optimization of Process Parameters

As discussed in Section 5.4, the model parameters tend to be stable with respect to the reactor configuration. Therefore, the calibrated simulation can be used to investigate different processing parameters in the same reactor configuration. That is, variations of the etch times can be computationally investigated without requiring further fabrication runs. In this section, the effect on the geometrical and optical parameters of changing the first etch time, i.e., the etch time with photoresist present (t_resist), as well as of varying the cumulative etch time (t_etch), is investigated.

Firstly, it is fundamental to determine if the process inputs, i.e., the etch time, and the process outputs, i.e., the geometric quantities of interest, scale with a representative feature dimension. In this case, the representative scaling dimension is the initial photoresist opening d. This is crucial for further process optimization, since it addresses the issue of generalizability of the design guidelines to different feature scales. That is, if the resulting shape follows a consistent scaling behavior, the optimized etch times can be applied to different photoresist configurations by considering the d scaling. Otherwise, other geometric scales such as, e.g., the photoresist thickness, might also play a role and should be considered. The determination of the scaling behavior is performed through a scale analysis, shown in Fig. 6.7. In it, both the main processing input, the t_resist, and the key output, the *ROC*, are divided by the respective d for each of the three simulated cavities.

Figure 6.7 shows that the scaled evolutions of the *ROC* for the three studied cavities follow very similar curves which is evidence that d truly is the key physical scale. This enables further analyses to focus on a single cavity, since the results from the others can in principle be recovered via scaling. The same scaling behavior is plotted in Fig. 6.8 on logarithmic axes. In this plot, the microcavities with $d = 34\,\mu\text{m}$ and $d = 52\,\mu\text{m}$ have a closer agreement than that with $d = 12.4\,\mu\text{m}$. Although this is an indication that other geometrical sizes, such as the photoresist thickness, could be affecting the smallest cavity, this should not be overemphasized. The logarithmic scale can exaggerate the effect of other phenomena, such as the impact of the Monte Carlo noise or the intrinsic accuracy of the feature detection algorithm. Therefore, the conclusion that the process follows a single scaling behavior remains valid.

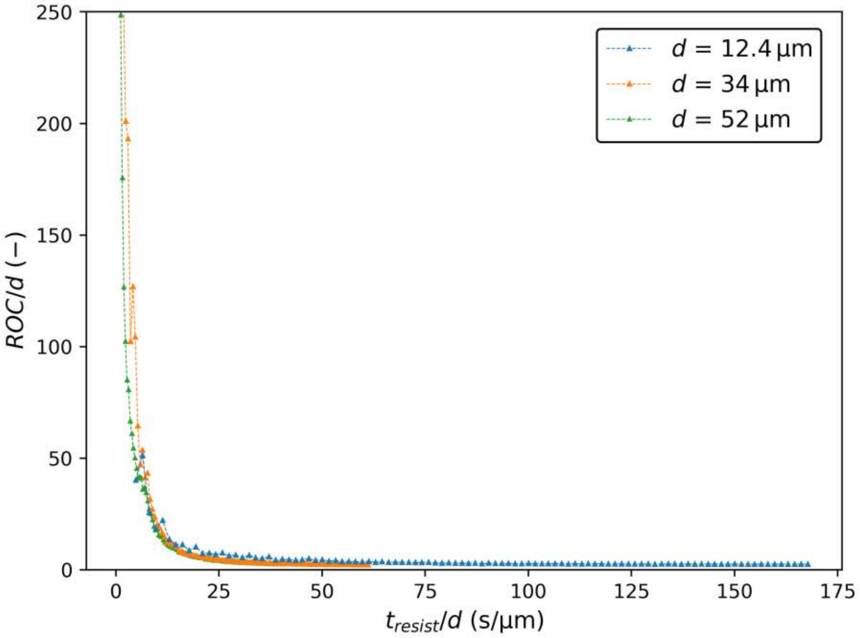

Figure 6.7: Scaling behavior of the *ROC* for simulated cavities during the first etch step. Both the input (t_{resist}) and the output (*ROC*) are scaled according to the initial photoresist opening diameter d. Adapted from Aguinsky *et al.*, *J. Micromech. Microeng.* 31, (2021) p. 125003. [174], © The Authors, licensed under the CC BY 4.0 License, `https://creativecommons.org/licenses/by/4.0/`.

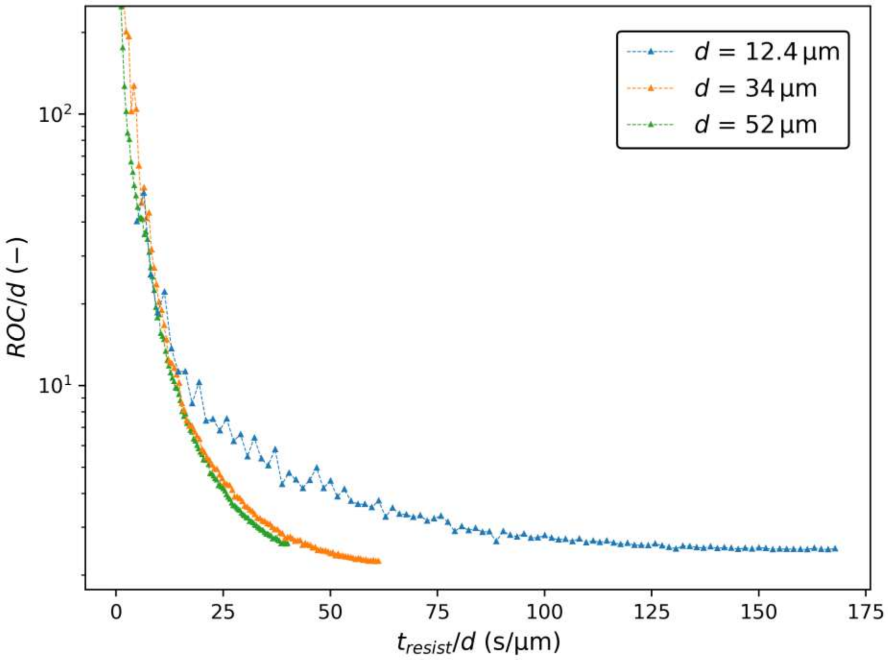

Figure 6.8: Scaling behavior of the *ROC* from Fig. 6.7 on logarithmic axes.

With the demonstrated scaling behavior of the characteristics of the microcavity, the time evolution of the geometric parameters h, O, and ROC can be investigated for a single microcavity with initial photoresist opening $d = 12.4\,\mu\text{m}$ for different simulated values of t_{resist}. This is depicted in Fig. 6.9 which also includes the same extracted parameters from the experimental cavity etched with $t_{\text{resist}} = 320\,\text{s}$ and $t_{\text{etch}} = 3200\,\text{s}$, under the label "Experiment". Good agreement is shown between the values extracted from simulated and experimental topographies which is a sign of the power of topography simulation in aiding the design process: If a similar analysis would be performed strictly experimentally, each point in the plot would require a separate costly experiment. The noise in the extracted geometric parameters is a consequence of the top-down approach being a Monte Carlo method.

In Fig. 6.9.a), it can be remarked that the first etch step is directly responsible for determining the h of the cavity, as it remains stable during the second step. The opening O, however, shown in Fig. 6.9.b), is defined by both etch steps. Nonetheless, it can be noted that the rate of change of O is determined by the length of t_{resist}. Finally, the ROC in Fig. 6.9.c) shows a competitive behavior between both etch steps. That is, the ROC has its lowest value defined by the first etch step, reaching a minimum at $t_{\text{resist}} = 1000\,\text{s}$, while the second etch step slowly increases it. According to the criteria in Eq. (6.6), the ROC should be kept to a minimum, thus, the second etch step should not be longer than necessary to reach the other optimization targets.

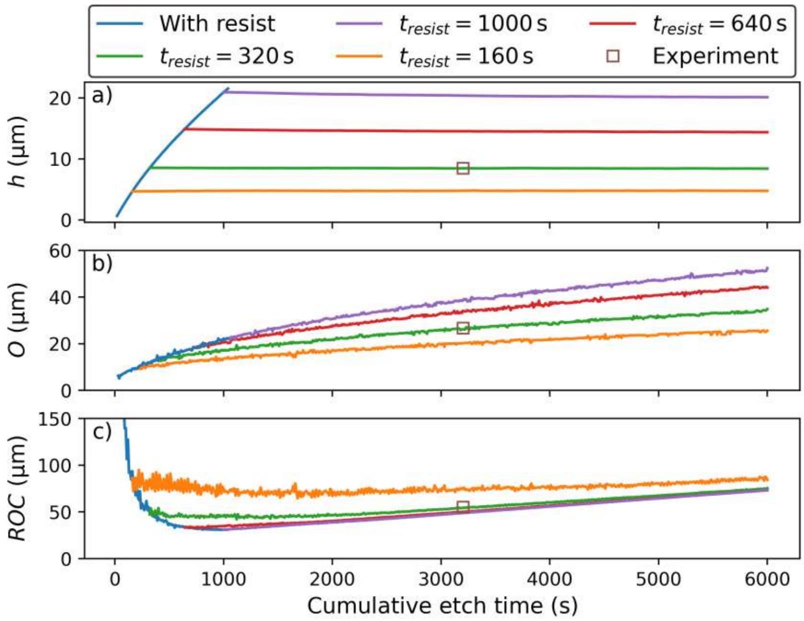

Figure 6.9: Time evolution of geometric parameters during simulated etching of a microcavity with 12.4 µm initial photoresist opening. a) Maximum depth (h). b) Maximum opening (O). c) Radius of curvature (ROC). The blue line shows the evolution during the first etch step. The same parameters are extracted from the manufactured microcavity and shown with label "Experiment". Adapted from Aguinsky *et al.*, *J. Micromech. Microeng.* 31, (2021) p. 125003. [174], © The Authors, licensed under the CC BY 4.0 License, `https://creativecommons.org/licenses/by/4.0/`.

The remaining optimization design criteria from Eq. (6.6), namely those involving w_M and ϵ_P, can now be appreciated. The etch time evolution of these optical parameters is shown in Fig. 6.10 for the same simulated microcavity with $d = 12.4\,\mu\text{m}$. In Fig. 6.10.a), it can be seen that the t_{etch} necessary to reach the design criterion $O > 6w_M$ is greatly reduced with increased t_{resist}. In fact, it is already fulfilled during the first etch step at a time of approximately $t_{\text{resist}} = 600\,\text{s}$. In combination with the observed reduction in ROC in Fig. 6.9.c), it appears that t_{resist} should be increased by a factor of approximately 2 to improve microcavity quality. Attention must be placed, however, on further processing issues which might arise such as loss of photoresist structural integrity [171] or photoresist hardening [185, 208].

So far, the discussion has focused on the effect of the first etch step. It is in observing Fig. 6.10.b) that the necessity of the second etch step becomes abundantly clear. Except for the extreme values of t_{resist}, the quality of the cavity after the first step is very poor when analyzed through the lens of the parabolicity error from Eq. (6.5). As already motivated when this process was originally introduced [49], the second etch step is essentially isotropic, since there are no visibility effects from the masking layer. This is crucial to converge the feature shape into a parabola. However, this realization exposes a trade-off when considered in conjunction with Fig. 6.9: The second etch step is necessary to improve ϵ_P, however, it negatively impacts the ROC.

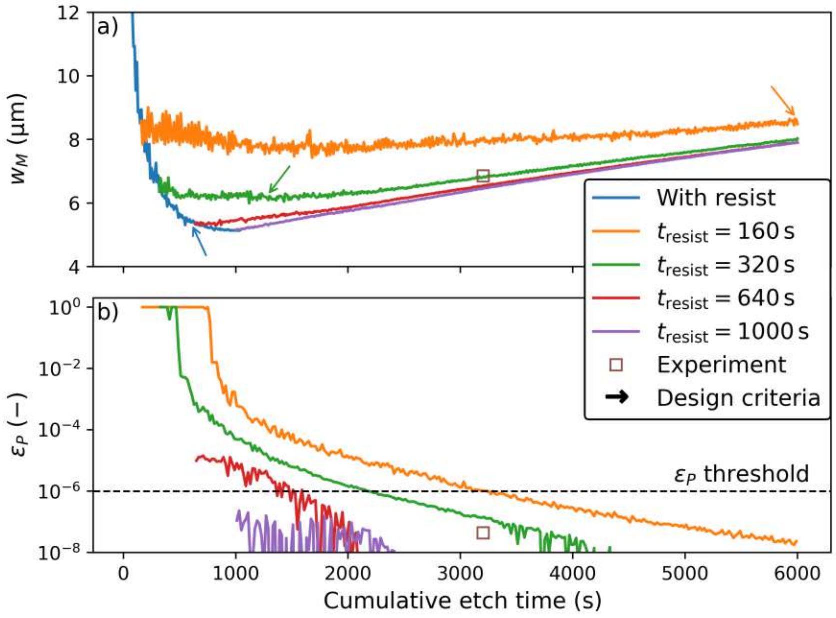

Figure 6.10: Etch time evolution of a) beam waist (w_M) and b) parabolicity error (ϵ_P) for a simulated microcavity with $d = 12.4\,\mu\text{m}$. The arrows in a) indicate the etch times when the criterion $O > 6w_M$ is achieved. Adapted from Aguinsky *et al.*, *J. Micromech. Microeng.* 31, (2021) p. 125003. [174], © The Authors, licensed under the CC BY 4.0 License, `https://creativecommons.org/licenses/by/4.0/`.

In conclusion, having achieved an accurate calibration to an experimentally manufactured cavity, the process could be efficiently explored via simulation. To improve the resonator quality, the first etch time should be increased as much as possible, ideally by a factor of 2, while keeping in mind possibly arising issues such as photoresist instability. Although the second etch time is necessary in the context of reducing ϵ_P, it should not be arbitrarily increased. As soon as ϵ_P crosses below a specified threshold, the etching should be stopped such as to not negatively impact the ROC or increase costs. The analysis from Fig. 6.10 indicates that the second etch step can be reduced by up to 50 %, leading to a cumulative t_{etch} reduction of 35 % when also considering the increase in t_{resist}. Finally, the scale analysis from Fig. 6.7 shows that there is room to further minimize the ROC by reducing the photoresist diameter d. However, this exploration should be performed carefully, since Fig. 6.8 indicates that a change of scaling regime could take place at excessively low values of d.

Chapter 7

Conclusion and Outlook

This thesis has thoroughly addressed the issue of phenomenological models for reactive single-particle transport in topography simulation. At a first glance, these models might appear to be straightforward, thus not warranting an in-depth investigation. However, as discussed in detail throughout this work, the correct application of single-particle modeling requires very careful consideration and deep knowledge of the involved processing technique to obtain both a reproduction of experimental surfaces and useful chemical insights.

The fundamental constituents of modern topography simulation were introduced: The LS method, and reactive transport models, as well as their interface through the surface advection velocity field. The fundamental phenomenological model at the core of reactive single-particle transport, first-order reversible Langmuir kinetics, was reviewed and discussed with respect to the underlying chemical and physical assumptions. However, a full description of the Langmuir kinetics is incomplete without a discussion of the calculation method for the local reactant fluxes. Therefore, an overview of the four main approaches to calculate the local fluxes was given, namely: Constant flux, bottom-up visibility calculation, top-down pseudo-particle tracking, and 1D models.

From the category of 1D models, Knudsen diffusive transport was chosen to merit a more in-depth examination due to its comparatively simple implementation, ability to provide direct physical insights, and, importantly, abundance of historical and contemporary misconceptions. To address this issue, Knudsen diffusivity was reformulated in a new and more modern fashion using an analogy to radiative heat transfer. First, the well-established expression of Knudsen diffusivity in a long cylinder is recovered. Then, the issue at the heart of the misconceptions was addressed: How to handle geometries with lateral cross-sections different from a cylinder. Particularly, the divergence of the mathematical formulation of Knudsen diffusivity for an infinitely wide trench is discussed. In conclusion, it is shown that 3D geometries are not completely equivalent to their 2D cross-sections. Although commonly used mappings, such as the hydraulic diameter approximation, attempt to simplify the involved geometries into an EAR, the underlying 3D complexity often resists such coarse simplifications.

With a firmer understanding of Knudsen diffusive transport processes, this 1D model was then applied to thermal ALP. Since these processing techniques exploit the self-limiting nature of the surface reactions, the first-order irreversible Langmuir kinetics had to be integrated with the diffusive transport model, showing the profound relationship between reactant transport and surface reactions. Additionally, the novel integration of this reactive transport model with the LS method through the introduction of an artificial time unit was shown.

After manual calibration of parameters to reported experimental data of ALD of Al_2O_3, the temperature dependence of the phenomenological parameters is determined. From this analysis, the importance of the reversibility of the H_2O reaction, particularly at low temperatures, is demonstrated. Additionally, an activation energy comparable with recent direct experimental studies is extracted. By reproducing multiple reactors in the TMA-limited regime, remarkable parameter stability is achieved. This is evidence that the phenomenological parameters are strongly linked to the reactor parameters, most importantly the substrate temperature. Thus, the parameters can be interpreted as a proxy of the reactor setup. Finally, a qualitative analysis of both ALD and ALE of HfO_2 is performed. Due to its efficient integration into a commercial simulator, a path for future investigations of device performance is highlighted.

Attention is then placed on the process of low-bias SF_6 plasma etching of Si. Even though this process is employed due to its near-isotropic etch characteristics, the final surfaces are known to be different from those obtained from ideal isotropic etching. To accurately reproduce these surfaces using topography simulation, the available flux calculation approaches were evaluated. The top-down pseudo-particle tracking approach using a constant effective sticking coefficient was shown to be sufficient to reproduce the experimental surfaces. Moreover, by reproducing multiple geometries reported in the literature using the same surface model and flux calculation approach, the phenomenological model parameters again appear to serve as a proxy of the reactor configuration.

Through a series of computational experiments, a novel empirical relationship was then constructed between an experimentally-accessible quantity of interest and the model parameters. Thus, information about the phenomenological model and, consequently, the surface chemistry and the state of the reactor, can be directly extracted from experimental topography measurements. This information can be used not only for accelerating calibration procedures but also to optimize the reactor setup by interpreting the parameters as, for example, surrogate variables of the fluorine radical density.

Finally, the capabilities of topography simulation are showcased by exploring the optimization of the fabrication process of silicon microcavity resonators. In order to move away from manual parameter calibration, a more robust automatic calibration procedure was introduced, including a custom feature detection algorithm. With that procedure, the entire phenomenological parameter set was calibrated using only the final state of the surface. Having achieved a calibrated simulation, the etch times and photoresist opening diameter of the involved two-step etching process were computationally investigated to optimize parameters indicative of device performance.

An increase in the first step etch time, ideally by doubling it, appears to positively impact the resonator quality. Simultaneously, the second etch time can be significantly reduced, leading to a reduction in overall etch time and, consequently, a reduction in cost and complexity.

In summary, it can be concluded that the final topography of a processed device possesses substantial information about the involved surface-chemical phenomena. Therefore, both direct modeling of experimental topographies and inverse modeling to gather information about the surface chemistry are possible. This strongly supports the applicability of first-order reversible Langmuir kinetics to a wide range of semiconductor processing applications. Through the judicious use of approximations, by paying careful attention to the calibration procedure, and by choosing the correct flux calculation approach, reactor-scale or first-principle simulations can either be complemented, or even completely bypassed in a few cases, using phenomenological modeling of reactive single-particle transport in topography simulation.

For future research, a natural extension of this work is the combination of the most physically rich flux calculation approach, the top-down pseudo-particle tracking, with first-order reversible Langmuir kinetics without the constant effective sticking coefficient approximation. For self-limiting reactions, a similar pulse time integration approach to that employed for thermal ALP can be employed to handle variable sticking coefficients. Nevertheless, for processes in the steady-state, a different self-consistent methodology for the calculation of the sticking coefficients will be necessary. This will require substantial computational resources, but the possible gains in accuracy and insight are very attractive. Additionally, as already hinted in the examination of aspect ratio dependent RIE, an increased number of phenomenological particle species will be necessary for certain processes.

In addition, the realization that the final surfaces carry the fingerprint of the surface chemical processes imposes additional pressure on the calibration method. The here-presented automated calibration procedure shows the tremendous promise of this approach, however, it had to be manually tailored to the application. To move beyond these custom solutions, recent advances in computer vision and artificial intelligence could be leveraged to create a truly general automatic calibration procedure and earnestly close the loop between experiment and simulation.

Bibliography

[1] Y. Yasuda-Masuoka *et al.*, “High performance 4nm FinFET platform (4LPE) with novel advanced transistor level DTCO for dual-CPP/HP-HD standard cells,” in *Proceedings of the International Electron Devices Meeting (IEDM)*, 2021, pp. 13.3.1–13.3.4. doi: 10.1109/IEDM19574.2021.9720656.

[2] Y.-D. Chih *et al.*, “Design challenges and solutions of emerging nonvolatile memory for embedded applications,” in *Proceedings of the International Electron Devices Meeting (IEDM)*, 2021, pp. 2.4.1–2.4.4. doi: 10.1109/IEDM19574.2021.9720557.

[3] T. Tan, X. Jiang, C. Wang, B. Yao, and H. Zhang, “2D material optoelectronics for information functional device applications: Status and challenges,” *Advanced Science*, vol. 7, p. 2000058, 2020. doi: 10.1002/ADVS.202000058.

[4] M. Kues *et al.*, “Quantum optical microcombs,” *Nature Photonics*, vol. 13, pp. 170–179, 2019. doi: 10.1038/s41566-019-0363-0.

[5] J. N. Haus *et al.*, “Robust pressure sensor in SOI technology with butterfly wiring for airfoil integration,” *Sensors*, vol. 21, p. 6140, 2021. doi: 10.3390/S21186140.

[6] D. Shepardson and J. L. Lee. (2022) Intel’s $20 bln Ohio factory could become world’s largest chip plant. [Accessed: 2022, Nov 6th]. [Online]. Available: https://www.reuters.com/technology/intel-plans-new-chip-manufacturing-site-ohio-report-2022-01-21/

[7] G. S. May and C. J. Spanos, *Fundamentals of Semiconductor Manufacturing and Process Control*. John Wiley & Sons, 2006. ISBN 9780471784067

[8] S. Selberherr, *Analysis and Simulation of Semiconductor Devices*. Springer Vienna, 1984. doi: 10.1007/978-3-7091-8752-4. . ISBN 978-3-7091-8754-8

[9] C. K. Maiti, *Introducing Technology Computer-Aided Design (TCAD)*. Jenny Stanford Publishing, 3 2017. doi: 10.1201/9781315364506. . ISBN 9781315364506

[10] J. Piprek, *Handbook of Optoelectronic Device Modeling and Simulation: Fundamentals, Materials, Nanostructures, LEDs, and Amplifiers, Vol. 1*. CRC Press, 2017. ISBN 9780367875602

[11] M. Luisier, A. Schenk, W. Fichtner, and G. Klimeck, “Atomistic simulation of nanowires in the $sp^3d^5s^*$ tight-binding formalism: From boundary conditions to strain calculations,” *Physical Review B*, vol. 74, p. 205323, 2006. doi: 10.1103/PHYSREVB.74.205323.

[12] J. Weinbub and D. K. Ferry, “Recent advances in Wigner function approaches,” *Applied Physics Reviews*, vol. 5, p. 041104, 2018. doi: 10.1063/1.5046663.

[13] S. Fiorentini, J. Ender, S. Selberherr, R. L. de Orio, W. Goes, and V. Sverdlov, “Coupled spin and charge drift-diffusion approach applied to magnetic tunnel junctions,” *Solid-State Electronics*, vol. 186, p. 108103, 2021. doi: 10.1016/J.SSE.2021.108103.

[14] S. J. Pearton, F. Ren, E. Patrick, M. E. Law, and A. Y. Polyakov, “Review—Ionizing radiation damage effects on GaN devices,” *ECS Journal of Solid State Science and Technology*, vol. 5, pp. Q35–Q60, 2016. doi: 10.1149/2.0251602JSS/XML.

[15] R. Hussin *et al.*, “Reliability aware simulation flow: From TCAD calibration to circuit level analysis,” in *Proceedings of the International Conference on Simulation of Semiconductor Processes and Devices (SISPAD)*. IEEE, 9 2015, pp. 152–155. doi: 10.1109/SISPAD.2015.7292281.

[16] H. Ceric, R. L. D. Orio, J. Cervenka, and S. Selberherr, “A comprehensive TCAD approach for assessing electromigration reliability of modern interconnects,” *IEEE Transactions on Device and Materials Reliability*, vol. 9, pp. 9–19, 2009. doi: 10.1109/TDMR.2008.2000893.

[17] S. Narayanan *et al.*, “Extraction of parasitic and channel resistance components in FinFETs using TCAD tools,” *Solid-State Electronics*, vol. 123, pp. 44–50, 2016. doi: 10.1016/J.SSE.2016.05.018.

[18] M. E. Law, “20 years of SISPAD: Adolescence of TCAD and further perspective,” in *Proceedings of the International Conference on Simulation of Semiconductor Processes and Devices (SISPAD)*. IEEE, 2016, pp. 1–6. doi: 10.1109/SISPAD.2016.7605135.

[19] M. A. Stettler *et al.*, “Industrial TCAD: Modeling atoms to chips,” *IEEE Transactions on Electron Devices*, vol. 68, pp. 5350–5357, 2021. doi: 10.1109/TED.2021.3076976.

[20] S. W. Jones, “Cost simulations to enable PPAC aware technology development,” in *Proceedings of the International Conference on Simulation of Semiconductor Processes and Devices (SISPAD)*. IEEE, 9 2021, pp. 215–218. doi: 10.1109/SISPAD54002.2021.9592598. . ISBN 978-1-6654-0685-7

[21] C.-F. Chien, H.-A. Kuo, and Y.-S. Lin, “Smart semiconductor manufacturing for pricing, demand planning, capacity portfolio and cost for sustainable supply chain management,” *International Journal of Logistics Research and Applications*, pp. 1–24, 5 2022. doi: 10.1080/13675567.2022.2076818.

[22] E. Chason *et al.*, “Ion beams in silicon processing and characterization,” *Journal of Applied Physics*, vol. 81, p. 6513, 1998. doi: 10.1063/1.365193.

[23] M. E. Law, H. Park, and P. Novell, “Theory of dopant diffusion assuming nondilute concentrations of dopant-defect pairs,” *Applied Physics Letters*, vol. 59, p. 3488, 1998. doi: 10.1063/1.105662.

[24] M. E. Law and S. M. Cea, “Continuum based modeling of silicon integrated circuit processing: An object oriented approach,” *Computational Materials Science*, vol. 12, pp. 289–308, 1998. doi: 10.1016/S0927-0256(98)00020-2.

[25] E. Ungersboeck, S. Dhar, G. Karlowatz, V. Sverdlov, H. Kosina, and S. Selberherr, “The effect of general strain on the band structure and electron mobility of silicon,” *IEEE Transactions on Electron Devices*, vol. 54, pp. 2183–2190, 9 2007. doi: 10.1109/TED.2007.902880.

[26] H. Kwon *et al.*, “TCAD augmented generative adversarial network for hot-spot detection and mask-layout optimization in a large area HARC etching process,” *Physics of Plasmas*, vol. 29, p. 073504, 7 2022. doi: 10.1063/5.0093076.

[27] K. K. Bhuwalka *et al.*, “Optimization and benchmarking FinFETs and GAA nanosheet architectures at 3-nm technology node: Impact of unique boosters,” *IEEE Transactions on Electron Devices*, vol. 69, pp. 4088–4094, 2022. doi: 10.1109/TED.2022.3178665.

[28] V. Ruiz-Díez *et al.*, “Modelling and characterization of the roof tile-shaped modes of AlN-based cantilever resonators in liquid media,” *Journal of Micromechanics and Microengineering*, vol. 26, p. 084008, 2016. doi: 10.1088/0960-1317/26/8/084008.

[29] T. Weingartner, N. Pokhrel, M. Sulangi, L. Bjorndal, E. Patrick, and M. E. Law, “Modeling process and device behavior of Josephson junctions in superconductor electronics with TCAD,” *IEEE Transactions on Electron Devices*, vol. 68, pp. 5448–5454, 2021. doi: 10.1109/TED.2021.3085540.

[30] A. Yanguas-Gil, *Growth and Transport in Nanostructured Materials: Reactive Transport in PVD, CVD, and ALD.* Springer, 2016. doi: 10.1007/978-3-319-24672-7.

[31] M. A. Lieberman and A. J. Lichtenberg, *Principles of Plasma Discharges and Materials Processing.* John Wiley & Sons, 2005. ISBN 0471720011

[32] S. M. Rossnagel, “Thin film deposition with physical vapor deposition and related technologies,” *Journal of Vacuum Science & Technology A*, vol. 21, p. S74, 2003. doi: 10.1116/1.1600450.

[33] N. Cheimarios, G. Kokkoris, and A. G. Boudouvis, “Multiscale modeling in chemical vapor deposition processes: Coupling reactor scale with feature scale computations,” *Chemical Engineering Science*, vol. 65, pp. 5018–5028, 2010. doi: 10.1016/J.CES.2010.06.004.

[34] S. Hou, M. Shakir, P.-E. Hellstrom, C.-M. Zetterling, and M. Ostling, “Process control and optimization of 4H-SiC semiconductor devices and circuits,” in *Proceedings of the Electron Devices Technology and Manufacturing Conference (EDTM).* IEEE, 3 2019, pp. 252–254. doi: 10.1109/EDTM.2019.8731140.

[35] V. Suvorov, A. Hössinger, Z. Djurić, and N. Ljepojevic, “A novel approach to three-dimensional semiconductor process simulation: Application to thermal oxidation,” *Journal of Computational Electronics*, vol. 5, pp. 291–295, 2006. doi: 10.1007/S10825-006-0003-Z.

[36] H. H. Gatzen, V. Saile, and J. Leuthold, *Lithography.* Springer Berlin Heidelberg, 2015, pp. 313–395.

[37] A. Erdmann, *Optical and EUV Lithography: A Modeling Perspective.* SPIE, 2021. doi: 10.1117/3.2576902. . ISBN 9781510639027

[38] M. J. Kushner, “Hybrid modelling of low temperature plasmas for fundamental investigations and equipment design,” *Journal of Physics D: Applied Physics*, vol. 42, p. 194013, 2009. doi: 10.1088/0022-3727/42/19/194013.

[39] M. Karner *et al.*, "Vertically stacked nanowire MOSFETs for sub-10nm nodes: Advanced topography, device, variability, and reliability simulations," in *Proceedings of the International Electron Devices Meeting (IEDM)*. IEEE, 2017, pp. 30.7.1–30.7.4. doi: 10.1109/IEDM.2016.7838516.

[40] S. Alasatri, M. Schneider, J. Mirwald, B. Hofko, and U. Schmid, "Accuracy and precision of resonant piezoelectric MEMS viscosity sensors in highly viscous bituminous materials," *Sensors and Actuators A: Physical*, vol. 347, p. 113903, 2022. doi: 10.1016/J.SNA.2022.113903.

[41] X. Klemenschits, S. Selberherr, and L. Filipovic, "Modeling of gate stack patterning for advanced technology nodes: A review," *Micromachines*, vol. 9, p. 631, 2018. doi: 10.3390/mi9120631.

[42] J. A. Sethian and D. Adalsteinsson, "An overview of level set methods for etching, deposition, and lithography development," *IEEE Transactions on Semiconductor Manufacturing*, vol. 10, pp. 167–184, 1997. doi: 10.1109/66.554505.

[43] A. La Magna and G. Garozzo, "Factors affecting profile evolution in plasma etching of SiO_2: Modeling and experimental verification," *Journal of The Electrochemical Society*, vol. 150, pp. F178 – F185, 2003. doi: 10.1149/1.1602084.

[44] S. Huang *et al.*, "Plasma etching of high aspect ratio features in SiO_2 using $Ar/C_4F_8/O_2$ mixtures: A computational investigation," *Journal of Vacuum Science & Technology A*, vol. 37, p. 031304, 2019. doi: 10.1116/1.5090606.

[45] V. M. Donnelly, "Reactions of fluorine atoms with silicon, revisited, again," *Journal of Vacuum Science & Technology A*, vol. 35, p. 05C202, 2017. doi: 10.1116/1.4983922.

[46] C. J. Mogab, "The loading effect in plasma etching," *Journal of The Electrochemical Society*, vol. 124, pp. 1262–1268, 1977. doi: 10.1149/1.2133542/XML.

[47] H. G. Gauch Jr, *Parsimony and Efficiency*. Cambridge University Press, 2002, p. 269–326.

[48] X. Klemenschits, S. Selberherr, and L. Filipovic, "Geometric advection and its application in the emulation of high aspect ratio structures," *Computer Methods in Applied Mechanics and Engineering*, vol. 386, pp. 114 196–1 – 114 196–22, 2021. doi: 10.1016/j.cma.2021.114196.

[49] K. P. Larsen, J. T. Ravnkilde, and O. Hansen, "Investigations of the isotropic etch of an ICP source for silicon microlens mold fabrication," *Journal of Micromechanics and Microengineering*, vol. 15, pp. 873–882, 2005. doi: 10.1088/0960-1317/15/4/028.

[50] H. Komiyama, Y. Shimogaki, and Y. Egashira, "Chemical reaction engineering in the design of CVD reactors," *Chemical Engineering Science*, vol. 54, pp. 1941–1957, 7 1999. doi: 10.1016/S0009-2509(98)00443-6.

[51] N. Pokhrel, T. A. Weingartner, M. A. Sulangi, E. E. Patrick, and M. E. Law, "Modeling the effect of fabrication process on grain boundary formation in Nb/Al-Alo_x/Nb Josephson junction circuit," *IEEE Transactions on Applied Superconductivity*, vol. 31, 8 2021. doi: 10.1109/TASC.2021.3066533.

[52] C. M. Huard, Y. Zhang, S. Sriraman, A. Paterson, and M. J. Kushner, “Role of neutral transport in aspect ratio dependent plasma etching of three-dimensional features,” *Journal of Vacuum Science & Technology A*, vol. 35, no. 5, pp. 05C301–1 – 05C301–18, 2017. doi: 10.1116/1.4973953.

[53] X. Klemenschits, “Emulation and Simulation of Microelectronic Fabrication Processes,” Doctoral dissertation, TU Wien, 2022, [Accessed: 2022, July]. [Online]. Available: https://www.iue.tuwien.ac.at/phd/klemenschits/index.html

[54] Synopsys. Sentaurus Topography. [Online]. Available: https://www.synopsys.com/silicon/tcad/process-simulation/sentaurus-topography.html

[55] Silvaco. Victory Process 2D and 3D Layout-Driven Simulator. [Online]. Available: https://silvaco.com/tcad/victory-process-3d/

[56] S. Morarka, N. G. Rudawski, M. E. Law, K. S. Jones, and R. G. Elliman, “Modeling two-dimensional solid-phase epitaxial regrowth using level set methods,” *Journal of Applied Physics*, vol. 105, p. 053701, 2009. doi: 10.1063/1.3082086.

[57] ViennaTS. [Online]. Available: https://github.com/viennats/viennats-dev

[58] S. Osher and J. A. Sethian, “Fronts propagating with curvature-dependent speed: Algorithms based on Hamilton-Jacobi formulations,” *Journal of Computational Physics*, vol. 79, no. 1, pp. 12–49, 1988. doi: 10.1016/0021-9991(88)90002-2.

[59] J. Sethian, *Level Set Methods and Fast Marching Methods: Evolving Interfaces in Computational Geometry, Fluid Mechanics, Computer Vision, and Materials Science.* Cambridge University Press, 1999.

[60] D. Adalsteinsson and J. A. Sethian, “A level set approach to a unified model for etching, deposition, and lithography I: Algorithms and two-dimensional simulations,” *Journal of Computational Physics*, vol. 120, pp. 128–144, 1995. doi: 10.1006/JCPH.1995.1153.

[61] D. Adalsteinsson and J. A. Sethian, “A level set approach to a unified model for etching, deposition, and lithography II: Three-dimensional simulations,” *Journal of Computational Physics*, vol. 122, pp. 348–366, 12 1995. doi: 10.1006/JCPH.1995.1221.

[62] S. Osher and R. P. Fedkiw, “Level set methods: An overview and some recent results,” *Journal of Computational Physics*, vol. 169, pp. 463–502, 2001. doi: 10.1006/jcph.2000.6636.

[63] B. Engquist and S. Osher, “One-sided difference approximations for nonlinear conservation laws,” *Mathematics of Computation*, vol. 36, pp. 321–351, 1981. doi: 10.1090/s0025-5718-1981-0606500-x.

[64] J. A. Sethian, “A fast marching level set method for monotonically advancing fronts,” *Proceedings of the National Academy of Sciences*, vol. 93, no. 4, pp. 1591–1595, 1996. doi: 10.1073/pnas.93.4.1591.

[65] D. Adalsteinsson and J. A. Sethian, “A fast level set method for propagating interfaces,” *Journal of Computational Physics*, vol. 118, no. 2, pp. 269–277, 1995. doi: 10.1006/jcph.1995.1098.

[66] J. Weinbub and A. Hössinger, “Comparison of the parallel fast marching method, the fast iterative method, and the parallel semi-ordered fast iterative method,” *Procedia Computer Science*, vol. 80, pp. 2271–2275, 2016. doi: 10.1016/J.PROCS.2016.05.408.

[67] M. Quell, G. Diamantopoulos, A. Hössinger, and J. Weinbub, “Shared-memory block-based fast marching method for hierarchical meshes,” *Journal of Computational and Applied Mathematics*, vol. 392, p. 113488, 8 2021. doi: 10.1016/J.CAM.2021.113488.

[68] I. Langmuir, “The adsorption of gases on plane surfaces of glass, mica and platinum,” *Journal of the American Chemical Society*, vol. 40, pp. 1361–1403, 1918. doi: 10.1021/JA02242A004.

[69] A. W. Adamson and A. P. Gast, *Physical Chemistry of Surfaces*, 6th ed. Wiley-Interscience, 1997. ISBN 978-0471148739

[70] Y. S. Ho and G. McKay, “Pseudo-second order model for sorption processes,” *Process Biochemistry*, vol. 34, pp. 451–465, 1999. doi: 10.1016/S0032-9592(98)00112-5.

[71] J. C. Bullen, S. Saleesongsom, K. Gallagher, and D. J. Weiss, “A revised pseudo-second-order kinetic model for adsorption, sensitive to changes in adsorbate and adsorbent concentrations,” *Langmuir*, vol. 37, pp. 3189–3201, 2021. doi: 10.1021/ACS.LANGMUIR.1C00142.

[72] M. Knudsen, “Eine Revision der Gleichgewichtsbedingung der Gase. Thermische Molekularströmung,” *Annalen der Physik*, vol. 336, pp. 205–229, 1909. doi: 10.1002/ANDP.19093360110.

[73] M. Knudsen, “Das Cosinusgesetz in der kinetischen Gastheorie,” *Annalen der Physik*, vol. 353, pp. 1113–1121, 1916. doi: 10.1002/ANDP.19163532409.

[74] I. Langmuir, “The evaporation, condensation and reflection of molecules and the mechanism of adsorption,” *Physical Review*, vol. 8, p. 149, 1916. doi: 10.1103/PhysRev.8.149.

[75] R. J. Hoekstra, M. J. Kushner, V. Sukharev, and P. Schoenborn, “Microtrenching resulting from specular reflection during chlorine etching of silicon,” *Journal of Vacuum Science & Technology B*, vol. 16, p. 2102, 1998. doi: 10.1116/1.590135.

[76] D. C. Gray, “Phenomenological modeling of ion-enhanced surface kinetics in fluorine-based plasma etching,” *Journal of Vacuum Science & Technology B*, vol. 11, no. 4, pp. 1243 – 1257, 1993. doi: 10.1116/1.586925.

[77] M. Tuda, K. Nishikawa, and K. Ono, “Numerical study of the etch anisotropy in low-pressure, high-density plasma etching,” *Journal of Applied Physics*, vol. 81, no. 2, pp. 960–967, 1997. doi: 10.1063/1.364189.

[78] E. Gogolides, P. Vauvert, G. Kokkoris, G. Turban, and A. G. Boudouvis, “Etching of SiO_2 and Si in fluorocarbon plasmas: A detailed surface model accounting for etching and deposition,” *Journal of Applied Physics*, vol. 88, p. 5570, 2000. doi: 10.1063/1.1311808.

[79] R. Courant, K. Friedrichs, and H. Lewy, “Über die partiellen Differenzengleichungen der mathematischen Physik,” *Mathematische Annalen*, vol. 100, no. 1, pp. 32–74, 1928. doi: 10.1007/BF01448839.

[80] S. G. Kandlikar, S. Garimella, D. Li, S. Colin, and M. R. King, *Heat Transfer and Fluid Flow in Minichannels and Microchannels*. Elsevier, 2006. doi: 10.1016/B978-008044527-4/50004-9.

[81] C. Qu, Y. Sakiyama, P. Agarwal, and M. J. Kushner, "Plasma-enhanced atomic layer deposition of SiO_2 film using capacitively coupled Ar/O_2 plasmas: A computational investigation," *Journal of Vacuum Science & Technology A*, vol. 39, p. 052403, 2021. doi: 10.1116/6.0001121.

[82] O. Ertl and S. Selberherr, "A fast void detection algorithm for three-dimensional deposition simulation," in *Proceedings of the International Conference on Simulation of Semiconductor Processes and Devices (SISPAD)*, 2009, pp. 174–177. doi: 10.1109/SISPAD.2009.5290221.

[83] O. Ertl and S. Selberherr, "A fast level set framework for large three-dimensional topography simulations," *Computer Physics Communications*, vol. 180, pp. 1242–1250, 2009. doi: 10.1016/J.CPC.2009.02.002.

[84] M. Köhler, "Isotropic Etching," in *Encyclopedia of Microfluidics and Nanofluidics*. Springer, 2008, pp. 877–884. doi: 10.1007/978-0-387-48998-8_751.

[85] K. E. Bean, "Anisotropic etching of silicon," *IEEE Transactions on Electron Devices*, vol. 25, pp. 1185–1193, 1978. doi: 10.1109/T-ED.1978.19250.

[86] I. Zubel, "Anisotropic etching of Si," *Journal of Micromechanics and Microengineering*, vol. 29, p. 093002, 2019. doi: 10.1088/1361-6439/AB2B8D.

[87] A. Toifl, F. Rodrigues, L. F. Aguinsky, A. Hössinger, and J. Weinbub, "Continuum level-set model for anisotropic wet etching of patterned sapphire substrates," *Semiconductor Science and Technology*, vol. 36, p. 045016, 2021. doi: 10.1088/1361-6641/ABE49B.

[88] L. F. Aguinsky *et al.*, "Phenomenological modeling of low-bias sulfur hexafluoride plasma etching of silicon," *Solid-State Electronics*, vol. 191, pp. 108 262–1–108 262–8, 2022. doi: 10.1016/j.sse.2022.108262.

[89] O. Ertl and S. Selberherr, "Three-dimensional level set based bosch process simulations using ray tracing for flux calculation," *Microelectronic Engineering*, vol. 87, pp. 20–29, 2010. doi: 10.1016/J.MEE.2009.05.011.

[90] D. Adalsteinsson and J. A. Sethian, "A level set approach to a unified model for etching, deposition, and lithography III: Redeposition, reemission, surface diffusion and complex simulations," *Journal of Computational Physics*, vol. 138, pp. 193–223, 1997. doi: 10.1006/JCPH.1997.5817.

[91] P. Manstetten, J. Weinbub, A. Hössinger, and S. Selberherr, "Using temporary explicit meshes for direct flux calculation on implicit surfaces," *Procedia Computer Science*, vol. 108, pp. 245–254, 1 2017. doi: 10.1016/J.PROCS.2017.05.067.

[92] P. Manstetten, A. Hössinger, J. Weinbub, and S. Selberherr, "Accelerated direct flux calculations using an adaptively refined icosahedron," in *Proceedings of the International Conference on Simulation of Semiconductor Processes and Devices (SISPAD)*. IEEE, 2017, pp. 73–76. doi: 10.23919/SISPAD.2017.8085267.

[93] L. Gnam, P. Manstetten, A. Hössinger, S. Selberherr, and J. Weinbub, "Accelerating flux calculations using sparse sampling," *Micromachines*, vol. 9, p. 550, 2018. doi: 10.3390/MI9110550.

[94] T. S. Cale, G. B. Raupp, and T. H. Gandy, "Free molecular transport and deposition in long rectangular trenches," *Journal of Applied Physics*, vol. 68, pp. 3645–3652, 1990. doi: 10.1063/1.346328.

[95] C. Heitzinger, A. Sheikholeslami, F. Badrieh, H. Puchner, and S. Selberherr, "Feature-scale process simulation and accurate capacitance extraction for the backend of a 100-nm aluminium/TEOS process," *IEEE Transactions on Electron Devices*, vol. 51, pp. 1129–1134, 2004. doi: 10.1109/TED.2004.829868.

[96] G. Kokkoris, A. Tserepi, A. G. Boudouvis, and E. Gogolides, "Simulation of SiO_2 and Si feature etching for microelectronics and microelectromechanical systems fabrication: A combined simulator coupling modules of surface etching, local flux calculation, and profile evolution," *Journal of Vacuum Science & Technology A*, vol. 22, p. 1896, 2004. doi: 10.1116/1.1738660.

[97] M. Hauguth, T. Danz, B. E. Volland, V. Ishshuk, D. Dreßler, and I. W. Rangelow, "New method for the precise flux calculation of neutrals for arbitrary surfaces in profile etch simulations," *Microelectronic Engineering*, vol. 85, pp. 982–984, 2008. doi: 10.1016/J.MEE.2008.01.019.

[98] M. F. Modest, *Radiative Heat Transfer*. Elsevier, 2013. doi: 10.1016/C2010-0-65874-3.

[99] T. Reiter, X. Klemenschits, and L. Filipovic, "Impact of plasma induced damage on the fabrication of 3D NAND flash memory," *Solid-State Electronics*, vol. 192, p. 108261, 2022. doi: 10.1016/J.SSE.2022.108261.

[100] M. Hauguth *et al.*, "Integrated plasma processing simulation framework, linking tool scale plasma models with 2D feature scale etch simulator," *Microelectronic Engineering*, vol. 86, pp. 976–978, 2009. doi: 10.1016/J.MEE.2009.02.012.

[101] L. Filipovic, "Modeling and simulation of atomic layer deposition," in *Proceedings of the International Conference on Simulation of Semiconductor Processes and Devices (SISPAD)*, 2019, pp. 323–326. doi: 10.1109/SISPAD.2019.8870462.

[102] G. Memos, E. Lidorikis, E. Gogolides, and G. Kokkoris, "A hybrid modeling framework for the investigation of surface roughening of polymers during oxygen plasma etching," *Journal of Physics D: Applied Physics*, vol. 54, p. 175205, 2021. doi: 10.1088/1361-6463/ABDB0B.

[103] M. C. Schwille, J. Barth, T. Schössler, F. Schön, J. W. Bartha, and M. Oettel, "Simulation approach of atomic layer deposition in large 3D structures," *Modelling and Simulation in Materials Science and Engineering*, vol. 25, p. 035008, 2017. doi: 10.1088/1361-651X/AA5F9D.

[104] J. Koike, M. Hosseini, H. T. Hai, D. Ando, and Y. Sutou, "Material innovation for MOL, BEOL, and 3D integration," in *Proceedings of the International Electron Devices Meeting (IEDM)*, 2018, pp. 32.3.1–32.3.4. doi: 10.1109/IEDM.2017.8268485.

[105] A. Goda, "Recent progress on 3D NAND Flash technologies," *Electronics*, vol. 10, p. 3156, 2021. doi: 10.3390/ELECTRONICS10243156.

[106] G. Kokkoris, A. G. Boudouvis, and E. Gogolides, "Integrated framework for the flux calculation of neutral species inside trenches and holes during plasma etching," *Journal of Vacuum Science & Technology A*, vol. 24, p. 2008, 2006. doi: 10.1116/1.2345643.

[107] J. R. Howell, M. P. Mengüç, and R. Siegel, *Thermal Radiation Heat Transfer.* CRC Press, 2020. doi: 10.1201/9780429327308.

[108] P. Manstetten, L. Filipovic, A. Hössinger, J. Weinbub, and S. Selberherr, “Framework to model neutral particle flux in convex high aspect ratio structures using one-dimensional radiosity,” *Solid-State Electronics*, vol. 128, pp. 141–147, 2017. doi: 10.1016/j.sse.2016.10.029.

[109] M. Ylilammi, O. M. Ylivaara, and R. L. Puurunen, “Modeling growth kinetics of thin films made by atomic layer deposition in lateral high-aspect-ratio structures,” *Journal of Applied Physics*, vol. 123, 2018. doi: 10.1063/1.5028178.

[110] V. Cremers, R. L. Puurunen, and J. Dendooven, “Conformality in atomic layer deposition: Current status overview of analysis and modelling,” *Applied Physics Reviews*, vol. 6, p. 021302, 6 2019. doi: 10.1063/1.5060967.

[111] A. Yanguas-Gil, J. A. Libera, and J. W. Elam, “Reactor scale simulations of ALD and ALE: Ideal and non-ideal self-limited processes in a cylindrical and a 300 mm wafer cross-flow reactor,” *Journal of Vacuum Science & Technology A*, vol. 39, p. 062404, 2021. doi: 10.1116/6.0001212.

[112] W. Steckelmacher, “Knudsen flow 75 years on: The current state of the art for flow of rarefied gases in tubes and systems,” *Reports on Progress in Physics*, vol. 49, p. 1083, 1986. doi: 10.1088/0034-4885/49/10/001.

[113] M. v. Smoluchowski, “Zur kinetischen Theorie der Transpiration und Diffusion verdünnter Gase,” *Annalen der Physik*, vol. 338, pp. 1559–1570, 1 1910. doi: 10.1002/ANDP.19103381623.

[114] P. Clausing, “Über die Strömung sehr verdünnter Gase durch Röhren von beliebiger Länge,” *Annalen der Physik*, vol. 404, pp. 961–989, 1 1932. doi: 10.1002/ANDP.19324040804.

[115] P. Clausing, “The flow of highly rarefied gases through tubes of arbitrary length,” *Journal of Vacuum Science and Technology*, vol. 8, pp. 636–646, 1971. doi: 10.1116/1.1316379.

[116] W. G. Pollard and R. D. Present, “On gaseous self-diffusion in long capillary tubes,” *Physical Review*, vol. 73, pp. 762–774, 4 1948. doi: 10.1103/PhysRev.73.762.

[117] R. D. Present, *Kinetic Theory of Gases.* McGraw-Hill, 1958.

[118] L. F. Aguinsky, P. Manstetten, A. Hössinger, S. Selberherr, and J. Weinbub, “A mathematical extension to Knudsen diffusion including direct flux and accurate geometric description,” in *Book of Abstracts of the International Workshop on Computational Nanotechnology (IWCN)*, 2019, pp. 109–110.

[119] L. F. Aguinsky, P. Manstetten, A. Hössinger, S. Selberherr, and J. Weinbub, “An extended Knudsen diffusion model for aspect ratio dependent atomic layer etching,” in *Book of Abstracts of the International Conference on Atomic Layer Deposition (ALD) Featuring the International Workshop on Atomic Layer Etching (ALE)*, 2019, p. 109.

[120] S. Chapman and T. G. Cowling, *The Mathematical Theory of Non-Uniform Gases*, 3rd ed. Cambridge University Press, 1990.

[121] H. C. Hottel and J. Keller, “Effect of reradiation on heat transmission in furnaces and through openings,” *Transactions of the ASME*, vol. 55, pp. 39–49, 1933.

[122] C. Buraczewski and J. Stasiek, “Application of generalized pythagoras theorem to calculation of configuration factors between surfaces of channels of revolution,” *International Journal of Heat and Fluid Flow*, vol. 4, no. 3, pp. 157–160, 1983. doi: 10.1016/0142-727X(83)90061-9.

[123] G. B. Raupp and T. S. Cale, “Step coverage prediction in low-pressure chemical vapor deposition,” *Chemistry of Materials*, vol. 1, no. 2, pp. 207–214, 1989.

[124] A. Yanguas-Gil and J. W. Elam, “Self-limited reaction-diffusion in nanostructured substrates: Surface coverage dynamics and analytic approximations to ALD saturation times,” *Chemical Vapor Deposition*, vol. 18, pp. 46–52, 2012. doi: 10.1002/CVDE.201106938.

[125] V. Cremers, F. Geenen, C. Detavernier, and J. Dendooven, “Monte Carlo simulations of atomic layer deposition on 3D large surface area structures: Required precursor exposure for pillar- versus hole-type structures,” *Journal of Vacuum Science & Technology A*, vol. 35, p. 01B115, 2016. doi: 10.1116/1.4968201.

[126] W. R. Inc., “Mathematica, Version 12.0,” Champaign, IL, 2022. [Online]. Available: https://www.wolfram.com/mathematica

[127] C. Bosanquet, “The optimum pressure for a diffusion separation plant,” British TA, Tech. Rep. BR-507, 1944.

[128] A. Feingold, “A new look at radiation configuration factors between disks,” *Journal of Heat Transfer*, vol. 100, no. 4, pp. 742–744, 1978. doi: 10.1115/1.3450893.

[129] T. Lill, *Atomic Layer Processing.* John Wiley & Sons, 2021. doi: 10.1002/9783527824199.

[130] J. W. Coburn and H. F. Winters, “Ion- and electron-assisted gas-surface chemistry—An important effect in plasma etching,” *Journal of Applied Physics*, vol. 50, p. 3189, 1979. doi: 10.1063/1.326355.

[131] V. M. Donnelly and A. Kornblit, “Plasma etching: Yesterday, today, and tomorrow,” *Journal of Vacuum Science & Technology A*, vol. 31, p. 050825, 2013. doi: 10.1116/1.4819316.

[132] F. Rodrigues, L. F. Aguinsky, A. Toifl, A. Scharinger, A. Hössinger, and J. Weinbub, “Surface reaction and topography modeling of fluorocarbon plasma etching,” in *International Conference on Simulation of Semiconductor Processes and Devices (SISPAD)*, 2021, pp. 229–232. doi: 10.1109/SISPAD54002.2021.9592583.

[133] C. G. Lee, K. J. Kanarik, and R. A. Gottscho, “The grand challenges of plasma etching: a manufacturing perspective,” *Journal of Physics D: Applied Physics*, vol. 47, p. 273001, 2014. doi: 10.1088/0022-3727/47/27/273001.

[134] K. Ishikawa *et al.*, “Progress in nanoscale dry processes for fabrication of high-aspect-ratio features: How can we control critical dimension uniformity at the bottom?” *Japanese Journal of Applied Physics*, vol. 57, p. 06JA01, 2018. doi: 10.7567/JJAP.57.06JA01/XML.

[135] H. Nagasawa, M. Abe, K. Yagi, T. Kawahara, and N. Hatta, “Fabrication of high performance 3C-SiC vertical MOSFETs by reducing planar defects,” *Physica Status Solidi (B)*, vol. 245, no. 7, pp. 1272–1280, 2008. doi: 10.1002/pssb.200844053.

[136] T. Kimoto and J. A. Cooper, *Fundamentals of Silicon Carbide Technology.* John Wiley & Sons, 2014. doi: 10.1002/9781118313534.

[137] F. Iacopi *et al.*, “Orientation-dependent stress relaxation in hetero-epitaxial 3C-SiC films,” *Applied Physics Letters*, vol. 102, no. 1, p. 011908, 2013. doi: 10.1063/1.4774087.

[138] T. Kreiliger *et al.*, “3C-SiC epitaxy on deeply patterned Si(111) substrates,” *Materials Science Forum*, vol. 858, pp. 151–154, 5 2016. doi: 10.4028/www.scientific.net/MSF.858.151.

[139] M. Masullo *et al.*, “Growth and coalescence of 3C-SiC on Si(111) micro-pillars by a phase-field approach,” *Materials*, vol. 12, p. 3223, 10 2019. doi: 10.3390/ma12193223.

[140] S. Morarka, N. G. Rudawski, and M. E. Law, “Level set modeling of the orientation dependence of solid phase epitaxial regrowth,” *Journal of Vacuum Science & Technology B*, vol. 26, p. 357, 2008. doi: 10.1116/1.2823063.

[141] A. Toifl *et al.*, “The level-set method for multi-material wet etching and non-planar selective epitaxy,” *IEEE Access*, vol. 8, pp. 115 406–115 422, 2020. doi: 10.1109/ACCESS.2020.3004136.

[142] S. M. George, “Atomic layer deposition: An overview,” *Chemical Reviews*, vol. 110, pp. 111–131, 2010. doi: 10.1021/cr900056b.

[143] A. Fischer, A. Routzahn, S. M. George, and T. Lill, “Thermal atomic layer etching: A review,” *Journal of Vacuum Science & Technology A*, vol. 39, p. 030801, 2021. doi: 10.1116/6.0000894.

[144] L. F. Aguinsky, F. Rodrigues, X. Klemenschits, L. Filipovic, A. Hössinger, and J. Weinbub, “Modeling non-ideal conformality during atomic layer deposition in high aspect ratio structures,” in *Book of Abstracts of the International Conference on Simulation of Semiconductor Processes and Devices (SISPAD)*, 2022, pp. 40–41.

[145] L. F. Aguinsky *et al.*, “Modeling non-ideal conformality during atomic layer deposition in high aspect ratio structures,” 2022. [Online]. Available: https://arxiv.org/abs/2210.00749

[146] R. L. Puurunen, “Surface chemistry of atomic layer deposition: A case study for the trimethylaluminum/water process,” *Journal of Applied Physics*, vol. 97, p. 121301, 2005. doi: 10.1063/1.1940727.

[147] H. C. M. Knoops, E. Langereis, M. C. M. van de Sanden, and W. M. M. Kessels, “Conformality of plasma-assisted ALD: Physical processes and modeling,” *Journal of The Electrochemical Society*, vol. 157, p. G241, 2010. doi: 10.1149/1.3491381/XML.

[148] S. Jakschik, U. Schroeder, T. Hecht, G. Dollinger, A. Bergmaier, and J. W. Bartha, “Physical properties of ALD-Al_2O_3 in a DRAM-capacitor equivalent structure comparing interfaces and oxygen precursors,” *Materials Science and Engineering: B*, vol. 107, pp. 251–254, 2004. doi: 10.1016/J.MSEB.2003.09.044.

[149] A. Fischer, A. Routzahn, R. J. Gasvoda, J. Sims, and T. Lill, “Control of etch profiles in high aspect ratio holes via precise reactant dosing in thermal atomic layer etching,” *Journal of Vacuum Science & Technology A*, vol. 40, p. 022603, 2022. doi: 10.1116/6.0001691.

[150] F. Zaera, “The surface chemistry of atomic layer depositions of solid thin films,” *Journal of Physical Chemistry Letters*, vol. 3, pp. 1301–1309, 2012. doi: 10.1021/jz300125f.

[151] Y. Lee and S. M. George, “Atomic layer etching of Al_2O_3 using sequential, self-limiting thermal reactions with $Sn(acac)_2$ and hydrogen fluoride,” *ACS Nano*, vol. 9, pp. 2061–2070, 2015. doi: 10.1021/NN507277F.

[152] M. Bonvalot *et al.*, “Area selective deposition using alternate deposition and etch super-cycle strategies,” *Dalton Transactions*, vol. 51, pp. 442–450, 2022. doi: 10.1039/D1DT03456A.

[153] T. Weckman, M. Shirazi, S. D. Elliott, and K. Laasonen, “Kinetic Monte Carlo study of the atomic layer deposition of zinc oxide,” *Journal of Physical Chemistry C*, vol. 122, pp. 27 044–27 058, 2018. doi: 10.1021/acs.jpcc.8b06909.

[154] R. Mullins, S. K. Natarajan, S. D. Elliott, and M. Nolan, “Self-limiting temperature window for thermal atomic layer etching of HfO_2 and ZrO_2 based on the atomic-scale mechanism,” *Chemistry of Materials*, vol. 32, pp. 3414–3426, 2020. doi: 0.1021/acs.chemmater.9b05021.

[155] M. C. Schwille, T. Schössler, F. Schön, M. Oettel, and J. W. Bartha, “Temperature dependence of the sticking coefficients of bis-diethyl aminosilane and trimethylaluminum in atomic layer deposition,” *Journal of Vacuum Science & Technology A*, vol. 35, p. 01B119, 2016. doi: 10.1116/1.4971197.

[156] E. Anderson *et al.*, *LAPACK Users’ Guide*, 3rd ed. Philadelphia, PA: Society for Industrial and Applied Mathematics, 1999. ISBN 0-89871-447-8

[157] OpenBLAS. [Online]. Available: http://www.openblas.net/

[158] X. Klemenschits, O. Ertl, P. Manstetten, J. Weinbub, and L. Filipovic. ViennaLS - A High Performance Sparse Level Set Library. [Online]. Available: https://github.com/ViennaTools/ViennaLS

[159] B. A. Sperling, B. Kalanyan, and J. E. Maslar, “Atomic layer deposition of Al_2O_3 using trimethylaluminum and H_2O: The kinetics of the H_2O half-cycle,” *Journal of Physical Chemistry C*, vol. 124, pp. 3410–3420, 2020. doi: 10.1021/ACS.JPCC.9B11291.

[160] F. Gao, S. Arpiainen, and R. L. Puurunen, “Microscopic silicon-based lateral high-aspect-ratio structures for thin film conformality analysis,” *Journal of Vacuum Science & Technology A*, vol. 33, p. 010601, 2015. doi: 10.1116/1.4903941.

[161] K. Arts *et al.*, “Sticking probabilities of H_2O and $Al(CH3)_3$ during atomic layer deposition of Al_2O_3 extracted from their impact on film conformality,” *Journal of Vacuum Science & Technology A*, vol. 37, p. 030908, 2019. doi: 10.1116/1.5093620.

[162] J. Yim *et al.*, “Saturation profile based conformality analysis for atomic layer deposition: Aluminum oxide in lateral high-aspect-ratio channels,” *Physical Chemistry Chemical Physics*, vol. 22, pp. 23 107–23 120, 2020. doi: 10.1039/D0CP03358H.

[163] S. Seo, T. Nam, H. B. R. Lee, H. Kim, and B. Shong, “Molecular oxidation of surface –CH_3 during atomic layer deposition of Al_2O_3 with H_2O, H_2O_2, and O_3: A theoretical study,” *Applied Surface Science*, vol. 457, pp. 376–380, 2018. doi: 10.1016/J.APSUSC.2018.06.160.

[164] V. Miikkulainen, M. Leskelä, M. Ritala, and R. L. Puurunen, “Crystallinity of inorganic films grown by atomic layer deposition: Overview and general trends,” *Journal of Applied Physics*, vol. 113, p. 021301, 2013. doi: 10.1063/1.4757907.

[165] J. Yim, E. Verkama, J. A. Velasco, K. Arts, and R. L. Puurunen, “Conformality of atomic layer deposition in microchannels: Impact of process parameters on the simulated thickness profile,” *Physical Chemistry Chemical Physics*, vol. 24, pp. 8645–8660, 2022. doi: 10.1039/D1CP04758B.

[166] Y. Chen, “ReRAM: History, status, and future,” *IEEE Transactions on Electron Devices*, vol. 67, pp. 1420–1433, 4 2020. doi: 10.1109/TED.2019.2961505.

[167] R. G. Gordon, D. Hausmann, E. Kim, and J. Shepard, “A kinetic model for step coverage by atomic layer deposition in narrow holes or trenches,” *Chemical Vapor Deposition*, vol. 9, pp. 73–78, 2003. doi: 10.1002/CVDE.200390005.

[168] G. Wachter *et al.*, “Silicon microcavity arrays with open access and a finesse of half a million,” *Light: Science & Applications*, vol. 8, p. 37, 2019. doi: 10.1038/s41377-019-0145-y.

[169] R. van Erp, R. Soleimanzadeh, L. Nela, G. Kampitsis, and E. Matioli, “Co-designing electronics with microfluidics for more sustainable cooling,” *Nature*, vol. 585, pp. 211–216, 2020. doi: 10.1038/s41586-020-2666-1.

[170] M. Rondé, A. J. Walton, and J. G. Terry, “Test structure for measuring the selectivity in XeF_2 and HF vapour etch processes,” *IEEE Transactions on Semiconductor Manufacturing*, vol. 34, pp. 241–247, 2021. doi: 10.1109/TSM.2021.3063633.

[171] P. Panduranga, A. Abdou, Z. Ren, R. H. Pedersen, and M. P. Nezhad, “Isotropic silicon etch characteristics in a purely inductively coupled SF_6 plasma,” *Journal of Vacuum Science & Technology B*, vol. 37, p. 061206, 2019. doi: 10.1116/1.5116021.

[172] D. C. Hays *et al.*, “Comparison of F_2-based gases for high-rate dry etching of si,” *Journal of The Electrochemical Society*, vol. 146, pp. 3812–3816, 1999. doi: 10.1149/1.1392556/XML.

[173] L. F. Aguinsky *et al.*, “Feature-scale modeling of low-bias SF_6 plasma etching of Si,” in *Joint International EUROSOI Workshop and International Conference on Ultimate Integration on Silicon (EUROSOI-ULIS)*, B. Cretu, Ed. IEEE, 2021, pp. 1–4. doi: 10.1109/EuroSOI-ULIS53016.2021.9560685.

[174] L. F. Aguinsky *et al.*, “Modeling and analysis of sulfur hexafluoride plasma etching for silicon microcavity resonators,” *Journal of Micromechanics and Microengineering*, vol. 31, no. 12, pp. 125 003–1–125 003–9, 2021. doi: 10.1088/1361-6439/ac2bad.

[175] C. L. Chernick *et al.*, “Fluorine compounds of Xenon and Radon,” *Science*, vol. 138, pp. 136–138, 10 1962. doi: 10.1126/SCIENCE.138.3537.136.

[176] L. Arana, N. de Mas, R. Schmidt, A. Franz, M. Schmidt, and K. Jensen, “Isotropic etching of silicon in fluorine gas for MEMS micromachining,” *Journal of Micromechanics and Microengineering*, vol. 17, pp. 384–392, 2 2007. doi: 10.1088/0960-1317/17/2/026.

[177] M. J. Madou, *Manufacturing Techniques for Microfabrication and Nanotechnology*. CRC Press, 2011, vol. 2. ISBN 9781420055191

[178] P. Arora, T. Nguyen, A. Chawla, S.-K. Nam, and V. M. Donnelly, “Role of sulfur in catalyzing fluorine atom fast etching of silicon with smooth surface morphology,” *Journal of Vacuum Science & Technology A*, vol. 37, p. 061303, 11 2019. doi: 10.1116/1.5125266.

[179] K. P. Larsen, D. H. Petersen, and O. Hansen, “Study of the roughness in a photoresist masked, isotropic, SF_6-based ICP silicon etch,” *Journal of The Electrochemical Society*, vol. 153, p. G1051, 2006. doi: 10.1149/1.2357723/XML.

[180] G. W. Biedermann *et al.*, “Ultrasmooth microfabricated mirrors for quantum information,” *Applied Physics Letters*, vol. 97, p. 181110, 2010. doi: 10.1063/1.3511743.

[181] M. Rudenko, V. Kuzmenko, A. Miakonkikh, and V. Lukichev, “On temperature and flux dependence of isotropic silicon etching in inductively coupled SF_6 plasma,” *Vacuum*, vol. 204, p. 111326, 2022. doi: 10.1016/J.VACUUM.2022.111326.

[182] R. J. Belen, S. Gomez, M. Kiehlbauch, D. Cooperberg, and E. S. Aydil, “Feature-scale model of Si etching in SF_6 plasma and comparison with experiments,” *Journal of Vacuum Science & Technology A*, vol. 23, pp. 99–113, 2005. doi: 10.1116/1.1830495.

[183] E. J. C. Tinacba, T. Ito, K. Karahashi, M. Isobe, and S. Hamaguchi, “Molecular dynamics simulation for reactive ion etching of Si and SiO_2 by SF_5^+ ions,” *Journal of Vacuum Science & Technology B*, vol. 39, no. 4, p. 043203, 2021. doi: 10.1116/6.0001230.

[184] M. A. Gosalvez, Y. Zhou, Y. Zhang, G. Zhang, Y. Li, and Y. Xing, “Simulation of microloading and ARDE in DRIE,” in *Proceedings of the International Conference on Solid-State Sensors, Actuators and Microsystems (TRANSDUCERS)*, 2015, pp. 1255–1258. doi: 10.1109/TRANSDUCERS.2015.7181158.

[185] K. R. Williams and R. S. Muller, “Etch rates for micromachining processing,” *Journal of Microelectromechanical Systems*, vol. 5, pp. 256–269, 1996. doi: 10.1109/84.546406.

[186] K. R. Williams, K. Gupta, and M. Wasilik, “Etch rates for micromachining processing - Part II,” *Journal of Microelectromechanical Systems*, vol. 12, pp. 761–778, 2003. doi: 10.1109/JMEMS.2003.820936.

[187] D. A. Steck, “Classical and Modern Optics,” Available online: http://steck.us/teaching (revision 1.8.3, 25 July 2021).

[188] J. Fait *et al.*, “High finesse microcavities in the optical telecom O-band,” *Applied Physics Letters*, vol. 119, p. 221112, 2021. doi: 10.1063/5.0066620.

[189] K. J. Vahala, “Optical microcavities,” *Nature*, vol. 424, pp. 839–846, 2003. doi: 10.1038/nature01939.

[190] Z. Moktadir *et al.*, “Etching techniques for realizing optical micro-cavity atom traps on silicon,” *Journal of Micromechanics and Microengineering*, vol. 14, pp. 82–85, 2004. doi: 10.1088/0960-1317/14/9/014.

[191] M. Trupke *et al.*, “Microfabricated high-finesse optical cavity with open access and small volume,” *Applied Physics Letters*, vol. 87, pp. 1–3, 2005. doi: 10.1063/1.2132066.

[192] T. Kessler *et al.*, “A sub-40-mHz-linewidth laser based on a silicon single-crystal optical cavity,” *Nature Photonics*, vol. 6, pp. 687–692, 2012. doi: 10.1038/nphoton.2012.217.

[193] W. Loh, S. Yegnanarayanan, F. O’Donnell, and P. W. Juodawlkis, “Ultra-narrow linewidth Brillouin laser with nanokelvin temperature self-referencing,” *Optica*, vol. 6, p. 152, 2 2019. doi: 10.1364/optica.6.000152.

[194] B. Bernhardt *et al.*, “Cavity-enhanced dual-comb spectroscopy,” *Nature Photonics*, vol. 4, pp. 55–57, 2010. doi: 10.1038/nphoton.2009.217.

[195] N. Picqué and T. W. Hänsch, “Frequency comb spectroscopy,” *Nature Photonics*, vol. 13, pp. 146–157, 2019. doi: 10.1038/s41566-018-0347-5.

[196] P. Samutpraphoot, P. L. Ocola, H. Bernien, C. Senko, V. Vuletić, and M. D. Lukin, “Strong coupling of two individually controlled atoms via a nanophotonic cavity,” *Physical Review Letters*, vol. 124, p. 063602, 2020. doi: 10.1103/PhysRevLett.124.063602.

[197] S. Haroche, M. Brune, and J. M. Raimond, “From cavity to circuit quantum electrodynamics,” *Nature Physics*, vol. 16, pp. 243–246, 2020. doi: 10.1038/s41567-020-0812-1.

[198] D. Nečas and P. Klapetek, “Gwyddion: An open-source software for SPM data analysis,” *Central European Journal of Physics*, vol. 10, pp. 181–188, 2 2012. doi: 10.2478/s11534-011-0096-2. . [Online]. Available: http://gwyddion.net/

[199] W. Schroeder, K. Martin, and B. Lorensen, *The Visualization Toolkit*, 4th ed. Kitware, 2006. ISBN 9781930934191

[200] H. Yuen, J. Princen, J. Illingworth, and J. Kittler, “Comparative study of Hough transform methods for circle finding,” *Image and Vision Computing*, vol. 8, pp. 71–77, 1990. doi: 10.1016/0262-8856(90)90059-E.

[201] OpenCV. [Online]. Available: https://opencv.org/

[202] P. Virtanen *et al.*, “SciPy 1.0: Fundamental algorithms for scientific computing in Python,” *Nature Methods*, vol. 17, pp. 261–272, 2020. doi: 10.1038/s41592-019-0686-2.

[203] C. Tsallis and D. A. Stariolo, “Generalized simulated annealing,” *Physica A: Statistical Mechanics and its Applications*, vol. 233, pp. 395–406, 1996. doi: 10.1016/S0378-4371(96)00271-3.

[204] D. L. Flamm, D. N. K. Wang, and D. Maydan, “Multiple-etchant loading effect and silicon etching in ClF_3 and related mixtures,” *Journal of The Electrochemical Society*, vol. 129, pp. 2755–2760, 1982. doi: 10.1149/1.2123673/XML.

[205] E. Cabruja and M. Schreiner, “Deep trenches in silicon using photoresist as a mask,” *Sensors and Actuators A: Physical*, vol. 37-38, pp. 766–771, 1993. doi: 10.1016/0924-4247(93)80129-5.

[206] C. Waits, B. Morgan, M. Kastantin, and R. Ghodssi, “Microfabrication of 3D silicon MEMS structures using gray-scale lithography and deep reactive ion etching,” *Sensors and Actuators A: Physical*, vol. 119, pp. 245–253, 2005. doi: 10.1016/j.sna.2004.03.024.

[207] D. Kleckner, W. T. Irvine, S. S. Oemrawsingh, and D. Bouwmeester, “Diffraction-limited high-finesse optical cavities,” *Physical Review A*, vol. 81, p. 043814, 2010. doi: 10.1103/PhysRevA.81.043814.

[208] S. Wolf and R. Tauber, *Silicon Processing for the VLSI Era*, 2nd ed. Lattice Press, 2000, vol. 1. ISBN 978-0961672164

List of Own Publications

Journal Articles

[1] **L. F. Aguinsky**, F. Rodrigues, T. Reiter, X. Klemenschits, L. Filipovic, A. Hössinger, J. Weinbub, "Modeling non-ideal conformality during atomic layer deposition in high aspect ratio structures", submitted to *Solid-State Electronics*, under review, 2022. arXiv: 2210.00749

[2] **L. F. Aguinsky**, F. Rodrigues, G. Wachter, M. Trupke, U. Schmid, A. Hössinger, J. Weinbub, "Phenomenological modeling of sulfur hexafluoride plasma etching of silicon", *Solid-State Electronics*, vol. 191, (**invited**), 108262-1–108262-8, 2022, doi: 10.1016/j.sse.2022.108262.

[3] **L. F. Aguinsky**, G. Wachter, P. Manstetten, F. Rodrigues, M. Trupke, U. Schmid, A. Hössinger, J. Weinbub, "Modeling and analysis of sulfur hexafluoride plasma etching for silicon microcavity resonators", *Journal of Micromechanics and Microengineering*, vol. 31, 125003-1–125003-9, 2021, doi: 10.1088/1361-6439/ac2bad.

[4] A. Toifl, F. Rodrigues, **L. F. Aguinsky**, A. Hössinger, J. Weinbub, "Continuum level-set model for anisotropic wet etching of patterned sapphire substrates", *Semiconductor Science and Technology*, vol. 36, 045016-1 – 045016-12, 2021, doi: 10.1088/1361-6641/abe49b.

Book Contributions

[5] **L. F. Aguinsky**, G. Wachter, F. Rodrigues, A. Scharinger, A. Toifl, M. Trupke, U. Schmid, A. Hössinger, J. Weinbub, "Feature-scale modeling of low-bias SF_6 plasma etching of Si", in *Joint International EUROSOI Workshop and International Conference on Ultimate Integration on Silicon (EUROSOI-ULIS)*. IEEE, pp. 1–4, 2021, doi: 10.1109/EuroSOI-ULIS53016.2021.9560685.

[6] F. Rodrigues, **L. F. Aguinsky**, A. Toifl, A. Scharinger, A. Hössinger, J. Weinbub, "Surface reaction and topography modeling of fluorocarbon plasma etching", in *International Conference on Simulation of Semiconductor Processes and Devices (SISPAD)*. IEEE, pp. 229–232, 2021, doi: 10.1109/SISPAD54002.2021.9592583.

Conference Contributions

[7] **L. F. Aguinsky**, "Advanced flux models in Victory Process: Low-bias SF_6 etching and thermal atomic layer processing", in *Silvaco Users Global Event (SURGE)*, (**invited**), 2022.

[8] **L. F. Aguinsky**, G. Wachter, A. Scharinger, F. Rodrigues, A. Toifl, M. Trupke, U. Schmid, A. Hössinger, J. Weinbub, "Feature-scale modeling of isotropic SF_6 plasma etching of Si", in *Book of Abstracts of the Joint International EUROSOI Workshop and International Conference on Ultimate Integration on Silicon (EUROSOI-ULIS)*, pp. 54–55, 2021.

[9] F. Rodrigues, **L. F. Aguinsky**, A. Toifl, A. Hössinger, J. Weinbub, "Feature scale modeling of fluorocarbon plasma etching for via structures including faceting phenomena", in *Book of Abstracts of the International Workshop on Computational Nanotechnology (IWCN)*, pp. 101–102, 2021.

[10] **L. F. Aguinsky**, P. Manstetten, A. Hössinger, S. Selberherr, J. Weinbub, "An extended Knudsen diffusion model for aspect ratio dependent atomic layer etching", in *Book of Abstracts of the International Conference on Atomic Layer Deposition (ALD) Featuring the International Workshop on Atomic Layer Etching (ALE)*, p. 109, 2019.

[11] **L. F. Aguinsky**, P. Manstetten, A. Hössinger, S. Selberherr, J. Weinbub, "Three-dimensional TCAD for atomic layer processing", in *Book of Abstracts of the Workshop on High Performance TCAD (WHPTCAD)*, p. 5, 2019.

[12] P. Manstetten, **L. F. Aguinsky**, S. Selberherr, J. Weinbub, "High-performance ray tracing for nonimaging applications", in *Book of Abstracts of the Workshop on High Performance TCAD (WHPTCAD)*, p. 20, 2019.

[13] P. Manstetten, G. Diamantopoulos, L. Gnam, **L. F. Aguinsky**, M. Quell, A. Toifl, A. Scharinger, A. Hössinger, M. Ballicchia, M. Nedjalkov, J. Weinbub, "High performance TCAD: From simulating fabrication processes to Wigner quantum transport", in *Book of Abstracts of the Workshop on High Performance TCAD (WHPTCAD)*, p. 13, 2019.

[14] **L. F. Aguinsky**, P. Manstetten, A. Hössinger, S. Selberherr, J. Weinbub, "A mathematical extension to Knudsen diffusion including direct flux and accurate geometric description", in *Book of Abstracts of the International Workshop on Computational Nanotechnology (IWCN)*, pp. 109-110, 2019.

[15] G. Diamantopoulos, P. Manstetten, L. Gnam, V. Simonka, **L. F. Aguinsky**, M. Quell, A. Toifl, A. Hössinger, J. Weinbub, "Recent advances in high performance process TCAD", in *Book of Abstracts of the SIAM Conference on Computational Science and Engineering (CSE)*, p. 335.

Curriculum Vitae

Education

03/2018 – present

Doctoral candidate in Electrical Engineering
Institute for Microelectronics, TU Wien
Vienna, Austria

10/2014 – 01/2018

Master's degree in Simulation Sciences
Thesis titled "Modeling Radiative Heat Transfer in Solar Thermochemical Particle Receivers"
RWTH Aachen University and Deutsches Zentrum für Luft- und Raumfahrt (DLR)
Aachen and Cologne, Germany

01/2012–06/2012

Exchange student
University of Montreal
Montreal, Canada

03/2009 – 08/2013

Bachelor's degree in Physics
Thesis titled "Capillary Electrophoresis in Ultra-High Electric Fields"
Federal University of Rio Grande do Sul (UFRGS)
Porto Alegre, RS, Brazil

Research Projects

2022

FWF Erwin Schrödinger Postdoctoral Fellowship
"Exploring Novel Materials for Next-Generation Optically Stimulated Memristors"
Integrated Systems Laboratory, ETH Zurich
Zurich, Switzerland

Awards and Scholarships

2021

Solid-State Electronics Best Poster Award
EUROSOI-ULIS 2021 Conference

2012

Science without Borders CNPq Scholarship
University of Montreal, Canada.

Teaching

2021

Bachelor Thesis Supervisor
Thesis titled "Rasterization for Flux Calculations in Topography Simulations"
TU Wien

2019–2022

Co-lecturer
Numerical Simulation and Scientific Computing I
TU Wien

2011

Teaching Assistant
Computational Methods of Physics B
UFRGS